CONSTITUTIVE MODELING AND NUMERICAL IMPLEMENTATION OF BRITTLE AND DUCTILE MATERIAL BEHAVIOR WITH THE AID OF INELASTIC XFEM AND DAMAGE-PLASTICITY MODELS

A Dissertation

Presented to

the Faculty of the Department of Civil and Environmental Engineering

University of Houston

In Partial Fulfillment

of the Requirements for the Degree

Doctor of Philosophy

in Civil Engineering

by

Shahriyar Beizaee

December 2013

CONSTITUTIVE MODELING AND NUMERICAL IMPLEMENTATION OF BRITTLE AND DUCTILE MATERIAL BEHAVIOR WITH THE AID OF INELASTIC XFEM AND DAMAGE-PLASTICITY MODELS

Shahriyar Beizaee

Approved:

Chair of the Committee
Kaspar J. Willam, Professor,
Civil and Environmental Engineering

Committee Members:

Abdeldjelil Belarbi, Professor,
Civil and Environmental Engineering

Mina Dawood, Assistant Professor,
Civil and Environmental Engineering

Kalyana Nakshatrala, Assistant Professor,
Civil and Environmental Engineering

Kenneth White, Professor,
Mechanical Engineering

Ilinca Stanciulescu, Assistant Professor,
Civil and Environmental Engineering,
Rice University

Suresh K. Khator, Associate Dean,
Cullen College of Engineering

Kaspar J. Willam, Professor and Chair,
Civil and Environmental Engineering

Acknowledgements

My greatest gratitude is given to Dr. Kaspar Willam, who as my advisor, directed all stages of my research program. His wisdom, knowledge, ideas, and commitment to the highest standards inspired and motivated me. This work could not have been accomplished without his guidance and encouragement. I would like to gratefully acknowledge Dr. Kenneth White, Dr. Abdeldjelil Belarbi, Dr. Mina Dawood, Dr. Ilinca Stanciulescu and Dr. Kalyana Nakshatrala, as members of my dissertation committee, for their generous time and valuable recommendations.

Many thanks to my friends, colleagues, and Dr. Giovanna Xotta for her great help with the experiments and numerical modelings. Jeannot Ahossin Guezo for his help during my experiments, Reza Mousavi and Amir Mohammadipour, for their assistance with the concrete specimens, and special thanks to Jeffery Miller for making the metallic flat bars.

The National Science Foundation sponsored part of the research study described herein. Their sponsorship is greatly appreciated.

Finally, I am most appreciative of my parents, family, and specially my loving wife, Lillian, who has always supported me, encouraged me, and believed in me, without which this dissertation would not be possible.

CONSTITUTIVE MODELING AND NUMERICAL IMPLEMENTATION OF BRITTLE AND DUCTILE MATERIAL BEHAVIOR WITH THE AID OF INELASTIC XFEM AND DAMAGE-PLASTICITY MODELS

An Abstract

of a

Dissertation

Presented to

the Faculty of the Department of Civil and Environmental Engineering

University of Houston

In Partial Fulfillment

of the Requirements for the Degree

Doctor of Philosophy

in Civil Engineering

by

Shahriyar Beizaee

December 2013

Abstract

Constitutive equations establish the relationship between kinetic with kinematic quantities to characterize the specific properties of the material. Mechanical constitutive relations are formulated to describe nonlinear and inelastic response behavior as well as brittle or ductile failure of metallic and cementitious materials in form of plastic and damage material formulations.

This dissertation addresses three topics: The first topic is focused on the peak response behavior of brittle and ductile materials by coupling plasticity with extended finite element method in order to model and follow discrete crack initiation and fracture propagation. This is accomplished by exploiting appropriate crack initiation criteria and performing analytical and numerical localization analysis to determine the critical orientation of the emerging failure surface. A series of experiments are performed on perforated metallic flat bars and the observations are used to validate the computational failure predictions.

The second topic is the finite element approximation of the field data obtained by photogrammetric non-contact digital image correlation analysis. This study includes experimental observations on various perforated metallic flat bars to evaluate displacements and strains by using digital image correlation analysis. The displacement images are used in order to determine the best approximation of finite element nodal displacement values based on least square approximation of the optical measurement data. Moreover, infinitesimal and finite strains are calculated and contrasted with the results processed by the commercial Aramis imaging software.

The last topic is focused on the localization of triaxial concrete behavior by a damage-plasticity model. In this constitutive formulation a three-invariant yield function is introduced to model plastic deformations and a damage function is used to determine the nonlinear and inelastic behavior of concrete. Coupling of the inelastic

damage and plasticity processes is introduced by a damage variable that enters the plastic yield function in terms of the effective stress. Localization properties of the combined damage-plasticity model are studied and the differences of the damage vs. plasticity constituents are explored and compared. A series of experimental tests are performed on concrete cylinders in cyclic compression and digital images are recorded to provide complementary field data of surface deformations and cracks.

Table of Contents

List of Figures

List of Tables

Chapter 1. Introduction

OBJECTIVE

The purpose of this study is to develop adequate constitutive relations for ductile as well as brittle behavior of metallic and cementitious materials by using plasticity and damage-plasticity constitutive models. The concept of inelastic extended finite element method is introduced to model discrete crack propagation for brittle and ductile materials. Furthermore, the error associated with the post processing of the experimental field data obtained by digital image correlation system is evaluated and analyzed with the aid of least square analysis of the finite element approximation of spatial displacements from the photogrammetric non-contact camera measurement data.

For calibrating and investigating the inelastic XFEM model, mild steel, high strength steel, aluminum and cast iron flat bar specimens are tested under uniaxial tension. These flat bars are made based on ASTM standards and both perforated and non-perforated specimens are used in order to observe the effect of perforation on the ultimate load capacity and ultimate strength. These flat bars are tested in tension with a constant displacement rate using a Tinius Olsen testing frame and the strain distribution on the surface of these bars are collected and analyzed with the Aramis software. In order to model the behavior of these materials, a linear elastic material behavior is assumed up to the yield limit and appropriate yield functions are used to describe the post-yield behavior in the plastic range up to peak and post-peak separation. For the case of brittle cast iron, the post-yield behavior which is a brittle mode of failure that is modeled by incorporating extended finite element method into the finite element formulation in order to be able to discretely follow the crack propagation. In the case of ductile behavior of mild steel, high strength steel and aluminum, the post-yield behavior consists of two regions, the first region is modeled with the aid of hardening/softening plasticity formulation and the second region which is the transition from stable material behavior to unstable fracture of that is modeled by using appropriate failure criteria and localization analysis. The concept of inelastic extended finite element method (IXFEM), is introduced by coupling localization analysis and extended finite element method which discretely follows the crack propagation in ductile material regime.

For the second part, the results obtained by digital image correlation system are assessed and compared to the results obtained by the least square approximation of the spatial displacements. In order to achieve this, the specimens were painted in white paint and black speckles are sprayed on the surface. Afterwards, a photogrammetric non-contact digital image correlation system was placed in front of the sample and the cameras were calibrated based on the instruction of the GOM optical measurements manual. The two cameras of this device take pictures with constant rate during the test and measure the movement of target points on the surface of the specimen. After these raw data are collected, the Aramis software product specifies several square boxes known as facets on the surface of the specimen where each of these facets contain n by n pixels of the target points and they are placed m pixels away from one another. The spatial position of the center point of these facets are calculated by averaging the positions of the corners of these facets and this data is treated as the raw data obtained from the experiment. Afterwards the Aramis software triangulates the motion of the target points and includes a procedure to calculates the infinitesimal and finite strain fields on the surface of the specimen. In order to assess the results provided by this software, the raw spatial positions and displacements of the facets are extracted and imported into a least square approximation code. This code is written in Matlab. It uses a finite element approximation of the displacement field in order to cover all the target points. A least square approximation of these data is performed and the best nodal displacement values are determined. Based on the nodal data infinitesimal and finite strain distributions are determined over the surface image window of the of the specimen. These least square results are explored and compared with the corresponding results of the Aramis software.

For the third part of the project, the behavior of concrete as a cementitious material is studied. The localization properties of the damage-plasticity model used to simulate the behavior of the concrete is investigated. Drucker-Prager plasticity and scalar damage are combined to model the behavior of concrete. It is assumed that plasticity and damage have different loading functions that are connected via effective stress measures of the damaged material skeleton that enter the plastic yield function. This model is numerically implemented in Fortran and is connected to Abaqus finite element software [ABAQUS (2012)] in form of a user subroutine (UMAT) for further investigations. This model is calibrated based on the uniaxial and cyclic experiments that are performed on concrete cylinders under displacement control which is performed by a Tinus Olsen testing frame. In short, the main objective of this study is to perform localization analysis of this model for damage, for plasticity and for the combined damage-plasticity when subjected to different loading scenarios considering associated and non-associated flow rules and to assess the localization properties of discontinuous strains and compare them with crack initiations of experimental observations.

In the following chapters, theoretical backgrounds of kinematic, kinetics and linear elasticity are discussed. General elastoplastic material behavior is introduced and different yield functions are presented in this dissertation. Furthermore, damage and plasticity models are combined and the background information on failure indicators is discussed. Localization analysis and extended finite element method (XFEM) are presented and the methodology is explained on how to combine these techniques. The numerical implementation of the plasticity, damage-plasticity and localization analysis are discussed and experimental observations on mild steel, high strength steel, cast iron and aluminum flat bars are presented. Theoretical information on the least square approximation of the raw data based on the finite element discretization is provided. Finally the simulations of these models are presented, concluding remarks are made and future opportunities are discussed.

BACKGROUND AND LITERATURE REVIEW

Constitutive behavior of materials which is the relationship between the stress and strain, has been the subject of numerous studies. It perhaps started by Robert Hooke (Hooke's theorem 1678) which described the force and displacement in form of linear relationship. This relation was further expanded and expressed by Augustin-Louis Cauchy [1789-1857] in form of a nonlinear relationship between the stress and strain tensors as

$$\sigma_{ij} = g_{ij}(\epsilon_{kl}). \tag{1.1}$$

If the elastic response is assumed to be independent of the load history, which implies that the strain energy per unit volume is only dependent on the strain and not on the load history, there exists a scalar potential, $W = W(\epsilon_{ij})$, from which the stress may be defined as

$$\sigma_{ij} = \frac{\partial W}{\partial \epsilon_{kl}}. \tag{1.2}$$

It is worthwhile to mention that if the constitutive relation changes according to coordinate rotation, the behavior would be anisotropic hyper-elastic.

In general, establishment of nonlinear constitutive models for materials is not trivial and although experimentation provides valuable information, the constitutive relation is achieved only for a particular path of loading, e.g., uniaxial compression, and the question of explicit constitutive models for arbitrary load paths remains unanswered (Ottosen and Ristinmaa, 2005). To address this issue and to determine the most explicit constitutive relation, the *representation theorems* are used. These theorems are for scalar as well as tensorial functions and have to satisfy the coordinate invariance property and material symmetries and are utilized to determine constitutive relations for thermo-elastic, visco-elastic, orthotropic linear elastic, plastic and many other material behaviors. Representation theorems are used in this work to determine the free energy function. It should be noted that there are so called *hypo-elastic* constitutive relations that relate the time derivative of stress tensor and time derivative of strain tensor, which is beyond the scope of this work.

Plasticity is used in order to account for the irreversible behavior of materials, specially ductile metals that experience large flow and plastification. To trigger plasticity during loading there has to be a yield envelope. One of the early yield conditions for metals is the Tresca hexagonal criterion (Tresca, 1864) which Tresca proposed during his work on plastic behavior of metals and is used for shear failure. The von Mises yield criterion(von Mises, 1913) is an extension of Tresca criterion in terms of J_2 invariant of deviatoric stress tensor. Besides these two yielding criteria that are independent of hydrostatic stresses, there are several yield envelopes to account for the first invariant of stress tensor and to account for voids or frictional properties, such as the criteria by Coulomb (1776), Drucker and Prager (1952), Gurson (1977; 1975). There are also yield surfaces that are based on three parameters and all the invariants of stresses are used in them, e.g., the yield criterion introduced by Willam and Warnke (1975). The von Mises yield criteria is used in this work to initiate plasticity for mild steel, high strength steel and aluminum, and Drucker-Prager and Willam-Warnke are used to model concrete behavior.

Choosing the appropriate yield function, it is possible to formulate plasticity. There are several types of post-yield formulations, such as isotropic hardening/softening, kinematic hardening and it is also possible to incorporate viscous effects in the plasticity formulation and model creep and relaxation behavior. However, in this dissertation it is assumed that the material behavior is rate independent.

An isotropic hardening/softening model based on associate flow rule is used in order to model the behavior of ductile metals where the elastoplastic constitutive formulation are used to evaluate the stress-strain relation in terms of the continuum elastoplastic tangent operator.

In order to study bifurcation, weak discontinuities, loss of uniqueness, loss of ellipticity and loss of symmetry in materials that may lead to strong discontinuities and failure, several papers have been studied. Localization, which is the jump of velocity gradient across the discontinuity surface occurs due to stationary acceleration waves which is discussed by Hill (1962). Computational simulation of discontinuous failure processes has been discussed by Willam and Iordache (1996) by means of establishing localization conditions and geometrical analysis for von Mises and Drucker-Prager yield functions and acquiring associate and non-associate flow rules. The localization analysis for generalized Drucker–Prager model is developed by Liebe and Willam (2001) and the localization characteristic of triaxial concrete model is been discussed by Kang and Willam (1999). Rice and Rudnicki (1979) discovered some features of the theory of localization of deformation and in another work, Rudnicki and Rice (1975) studied the conditions for the localization of deformation in pressure sensitive dilatant materials. Steinmann and Willam (1994) studied the effect of mesh alignment with localization direction in finite element analysis of elastoplastic discontinuities and Willam and Iordache (2001) revisited the hierarchy of different failure diagnostics when the material properties lose symmetry in the case of finite deformations and micropolar continua. The three dimensional localization analysis for several yield functions are described in Chaves (2003). It should be noted that Cosserat and Cosserat (1909) introduced the Cosserat or micropolar continuum where micro rotations as well as couple stresses are introduced into the Boltzmann or classic continuum that introduces unsymmetrical stress and strain tensors. This continuum also introduces a length scale that plays an important role in regularizing localized regions in finite element analysis as discussed by Willam et al. (1995), Iordache (1996) and Etse et al. (2003). The J_2 elastoplastic micropolar formulation is being discussed and an algorithm is provided for finite element analysis by de Borst (1993), Grammenoudis and Tsakmakis (2008) studied the micropolar plasticity for the special case of isotropic hardening.

In order to model concrete behavior, a damage-plasticity model is used, where the damage and plasticity functions are two separate functions as discussed by Grassl and Jirásek (2006). Also there has been lots of studies performed on coupled damage plasticity models such as the work of Lubliner et al. (1989) and Salari et al. (2004). The micro and macro damage models introduced by Mazars (1986) and continuum damage theory of Mazars and Pijaudier-Cabot (1989) are studied. Hansen and Schreyer (1992; 1994) introduced thermodynamically consistent theories as well as frameworks for theories of damage coupled with elastoplasticity. Carol (1996), Carol and Willam (1997) have done localization study and analysis of damage models.

It is also possible to incorporate XFEM capability in the finite element analysis in order to simulate strong discontinuities. Moës et al. (1999) introduced a finite element method for crack growth that did not need remeshing in order to propagate and later Giner et al. (1999) implemented the XFEM capability into Abaqus software.

It should be noted that in order to write the finite element framework, the books by Ottosen and Ristinmaa (2005) and Zienkiewicz et al. (2005) are used and the manuals of Matlab (2011), ABAQUS (2012) and GOM optical measurements company are used.

Chapter 2. Theory

In the first section of this chapter basic concepts of kinematics and kinetics are discussed and the constitutive relations of linear elastic isotropic material behavior is explained. With this background, the elastoplastic material behavior is introduced, different yield functions based on stress invariants are presented and flow rules, consistency condition and elastoplastic tensor are explained. For each yield function, the normal to the yield surface is derived. Afterwards the damage-plasticity formulations is introduced and two models of Drucker-Prager and Willam-Warnke are presented.

BASIC EQUATIONS

In this section, the theoretical background of kinetics and kinematics is explained. The infinitesimal and finite strain formulations are introduced and the constitutive relation between the elastic stress and strain tensors for linear elastic material behavior is explained.

2.1.1 Kinematics

At any instant of time t, a continuum occupies a region R of the space. It is assumed that the whole body is continuous and deformation is defined as the change of the continuum from one to another configuration. The position vectors of a point P of the continuum are defined by upper case $\boldsymbol{X}$ for the undeformed and by the lower case $\boldsymbol{x}$ for the deformed configurations. The corresponding coordinates are called *material* and *spatial* coordinates correspondingly,

$$\boldsymbol{X} = X_1\hat{\boldsymbol{I}}_1 + X_2\hat{\boldsymbol{I}}_2 + X_3\hat{\boldsymbol{I}}_3 \quad \text{and} \tag{2.1a}$$

$$\boldsymbol{x} = x_1\hat{\boldsymbol{e}}_1 + x_2\hat{\boldsymbol{e}}_2 + x_3\hat{\boldsymbol{e}}_3\,. \tag{2.1b}$$

The displacement vector joining point P from its original configuration to the deformed configuration can be defined either in the material or the spatial coordinates, expressed as

$$\boldsymbol{U} = U_K \hat{\boldsymbol{I}}_K \quad \text{and} \tag{2.2a}$$

$$\boldsymbol{u} = u_k \hat{\boldsymbol{e}}_k. \tag{2.2b}$$

When the continuum undergoes a deformation, this deformation is expressed either in terms of the initial or current coordinates, if it is defined with respect to the initial coordinates then it is known as the Lagrangian formulation, and for the latter case it is called the Eulerian formulations,

$$\boldsymbol{x} = \boldsymbol{x}(\boldsymbol{X}, t) \quad \text{and} \tag{2.3a}$$

$$\boldsymbol{X} = \boldsymbol{X}(\boldsymbol{x}, t)\,. \tag{2.3b}$$

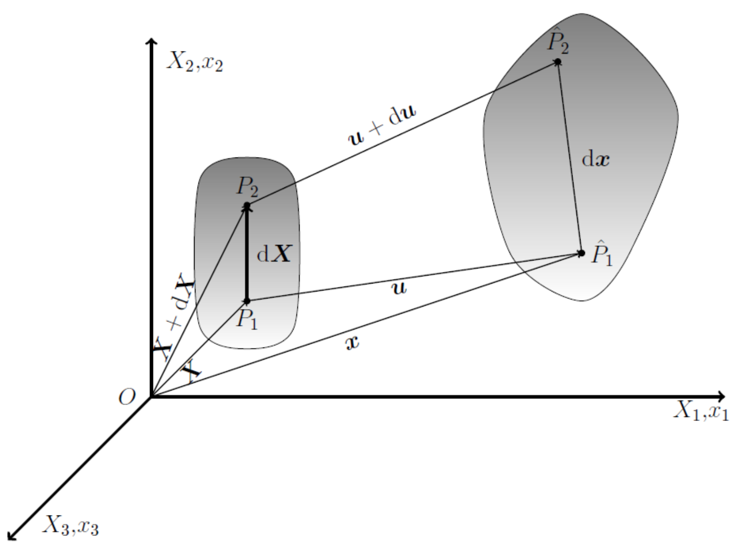

Figure 2.1: Initial and final configurations of a continuum.

Lets assume that there are two particles at points P_1 and P_2 in the continuum that after deformation go to $\hat{P}_1$ and $\hat{P}_2$. Position of the particle at point P_1 is defined by the vector $\boldsymbol{X}$ and the position of the particle at point P_2 is defined by $\boldsymbol{X} + \mathrm{d}\boldsymbol{X}$, and the distance between these particles is $\mathrm{d}\boldsymbol{X}$. After the deformation the new positions of the particles are defined by $\boldsymbol{x}$ and $\boldsymbol{x}+\mathrm{d}\boldsymbol{x}$. The deformation between points P_1 and $\hat{P}_1$ is described by $\boldsymbol{u}$ and the deformation between points P_2 and $\hat{P}_2$ is described by $\boldsymbol{u}+\mathrm{d}\boldsymbol{u}$. The magnitude of the length between P_1 and P_2 is defined as

$$(\mathrm{d}X)^2 = \mathrm{d}\boldsymbol{X} \cdot \mathrm{d}\boldsymbol{X} = \mathrm{d}X_i \mathrm{d}X_i, \tag{2.4}$$

where from equation (2.3b), $\mathrm{d}X_i$ can be defined as

$$\mathrm{d}X_i = \frac{\partial X_i}{\partial x_j}\mathrm{d}x_j \tag{2.5}$$

and equation (2.4) becomes

$$(\mathrm{d}X)^2 = \frac{\partial X_k}{\partial x_i}\frac{\partial X_k}{\partial x_j}\mathrm{d}x_i \mathrm{d}x_j = C_{ij}\mathrm{d}x_i \mathrm{d}x_j, \tag{2.6}$$

where C_{ij} is known as Cauchy's deformation tensor. Similarly $\mathrm{d}x_i$ can be defined in terms of $\mathrm{d}X_j$ in the form

$$\mathrm{d}x_i = \frac{\partial x_i}{\partial X_j}\mathrm{d}X_j \quad \text{or} \quad \mathrm{d}\boldsymbol{x} = \boldsymbol{F} \cdot \mathrm{d}\boldsymbol{X}, \tag{2.7}$$

where $\boldsymbol{F}$ is the material deformation gradient. The magnitude of the distance between points $\hat{P}_1$ and $\hat{P}_2$ may be written

$$(\mathrm{d}x)^2 = \frac{\partial x_k}{\partial X_i}\frac{\partial x_k}{\partial X_j}\mathrm{d}X_i \mathrm{d}X_j = G_{ij}\mathrm{d}X_i \mathrm{d}X_j, \tag{2.8}$$

where G_{ij} is the Green's deformation tensor. The difference between the magnitudes of the distance between the neighboring points at the current and the initial configuration provides a measure of the deformation and may be expressed in the form

$$(\mathrm{d}x)^2 - (\mathrm{d}X)^2 = \left(\frac{\partial x_k}{\partial X_i}\frac{\partial x_k}{\partial X_j} - \delta_{ij}\right)\mathrm{d}X_i\mathrm{d}X_j = 2E^G_{ij}\mathrm{d}X_i\mathrm{d}X_j, \tag{2.9}$$

where the second order tensor

$$E^G_{ij} = \frac{1}{2}\left(\frac{\partial x_k}{\partial X_i}\frac{\partial x_k}{\partial X_j} - \delta_{ij}\right) \quad \text{or} \quad \boldsymbol{E}^G = \frac{1}{2}\left(\boldsymbol{F}\cdot\boldsymbol{F} - \mathbf{1}\right), \tag{2.10}$$

is called the Green's (Lagrangian) finite strain tensor. The deformation may alternatively be expressed in the form

$$(\mathrm{d}x)^2 - (\mathrm{d}X)^2 = \left(\delta_{ij} - \frac{\partial X_k}{\partial x_i}\frac{\partial X_k}{\partial x_j}\right)\mathrm{d}x_i\mathrm{d}x_j = 2E^A_{ij}\mathrm{d}x_i\mathrm{d}x_j, \tag{2.11}$$

where the second order tensor

$$E^A_{ij} = \frac{1}{2}\left(\delta_{ij} - \frac{\partial X_k}{\partial x_i}\frac{\partial X_k}{\partial x_j}\right) \quad \text{or} \quad \boldsymbol{E}^A = \frac{1}{2}\left(\mathbf{1} - \boldsymbol{H}\cdot\boldsymbol{H}\right), \tag{2.12}$$

is called the Almansi's (Eulerian) finite strain tensor. In order to have the Green's and Almansi's finite strain tensors in terms of deformations, the following expression may be used and substituted in equations (2.10) and (2.12),

$$\boldsymbol{x} = \boldsymbol{X} + \boldsymbol{u} \quad \longrightarrow \quad \frac{\partial \boldsymbol{x}}{\partial \boldsymbol{X}} = \mathbf{1} + \frac{\partial \boldsymbol{u}}{\partial \boldsymbol{X}}. \tag{2.13}$$

The corresponding Lagrangian and Eulerian finite strain tensors take the form

$$E^G_{ij} = \frac{1}{2}\left(\frac{\partial u_i}{\partial X_j} + \frac{\partial u_j}{\partial X_i} + \frac{\partial u_k}{\partial X_i}\frac{\partial u_k}{\partial X_j}\right) \quad \text{and} \tag{2.14a}$$

$$E^A_{ij} = \frac{1}{2}\left(\frac{\partial u_i}{\partial x_j} + \frac{\partial u_j}{\partial x_i} - \frac{\partial u_k}{\partial x_i}\frac{\partial u_k}{\partial x_j}\right). \tag{2.14b}$$

The small deformation theory assumes that the deformation gradients are small compared to unity, therefore it is reasonable to assume that the multiplication of the deformation gradients is negligible in compare to the deformation gradient. With this assumption the Lagrangian and Eulerian strain tensors take the form

$$E_{ij}^G \simeq \frac{1}{2}\left(\frac{\partial u_i}{\partial X_j} + \frac{\partial u_j}{\partial X_i}\right) \quad \text{and} \tag{2.15a}$$

$$E_{ij}^A \simeq \frac{1}{2}\left(\frac{\partial u_i}{\partial x_j} + \frac{\partial u_j}{\partial x_i}\right), \tag{2.15b}$$

where it should be noted that if both displacement and displacement gradients are small, there is very small difference in the material and spatial coordinates and therefore the Lagrangian and Eulerian strain tensors are almost equal and is expressed as

$$E_{ij}^G = E_{ij}^A = \epsilon_{ij}. \tag{2.16}$$

In order to obtain more information on this subject please refer to continuum mechanics books such as Mase (1970).

2.1.2 Statics

An arbitrary volume in the space that is subjected to surface traction and body force is depicted in figure (2.2). When the resultant forces and moments on the volume are zero, the body is in equilibrium, expressed as

$$\int_S \boldsymbol{t}\mathrm{d}S + \int_V \rho\boldsymbol{b}\mathrm{d}V = 0 \quad \text{and} \tag{2.17a}$$

$$\int_S \boldsymbol{x} \times \boldsymbol{t}\mathrm{d}S + \int_V \boldsymbol{x} \times \rho\boldsymbol{b}\mathrm{d}V = 0. \tag{2.17b}$$

In equation (2.17a), $\boldsymbol{t}$ is the traction acting on the surface dS with the normal $\boldsymbol{n}$ and $\rho\boldsymbol{b}$ is the body force acting on the volume dV. Using the divergence theorem

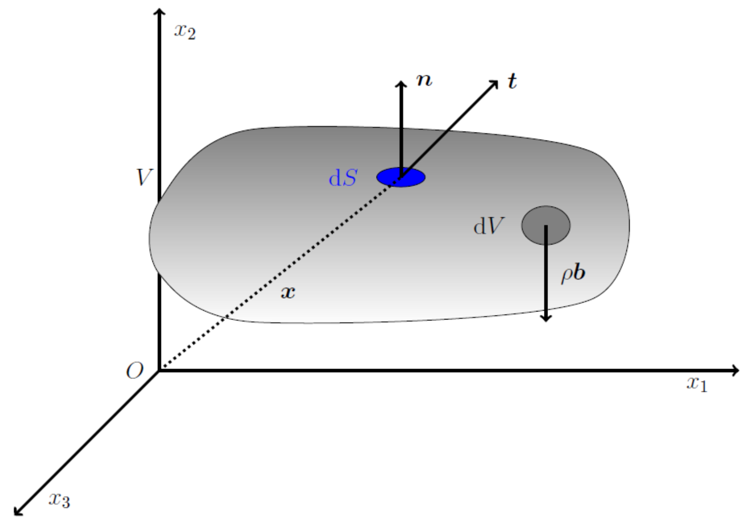

Figure 2.2: Traction and body force on an arbitrary volume.

equation (2.17a) may be written as

$$\int_V (\nabla \cdot \boldsymbol{\sigma} + \rho \boldsymbol{b}) \mathrm{d}V = 0 \quad \text{or} \quad \int (\sigma_{ji,j} + \rho b_i) \mathrm{d}V = 0 \tag{2.18}$$

and since V is arbitrary it takes the form

$$\nabla \cdot \boldsymbol{\sigma} + \rho \boldsymbol{b} = 0 \quad \text{or} \quad \sigma_{ji,j} + \rho b_i = 0, \tag{2.19}$$

which is called the equilibrium equation. Note that the traction vector is defined as

$$\boldsymbol{t} = \boldsymbol{\sigma} \cdot \boldsymbol{n}. \tag{2.20}$$

Equilibrium of moments about the origin which is shown in equation (2.17b) shows that the stress tensor is symmetric, therefore

$$\sigma_{ij} = \sigma_{ji}. \tag{2.21}$$

2.1.3 Linear Elastic Material Behavior

A linear elastic constitutive relation is described by generalized Hooke's theorem and states that the triaxial state of stress is proportional to the triaxial state of strain by a linear relation as follow

$$\boldsymbol{\sigma} = \mathbb{E} : \boldsymbol{\epsilon}, \tag{2.22}$$

where the stress and strain tensors can be expressed by standard (Voigt) format

$$\boldsymbol{\sigma} = \begin{pmatrix} \sigma_{11} \\ \sigma_{22} \\ \sigma_{33} \\ \sigma_{12} \\ \sigma_{23} \\ \sigma_{31} \end{pmatrix} \qquad \boldsymbol{\epsilon} = \begin{pmatrix} \epsilon_{11} \\ \epsilon_{22} \\ \epsilon_{33} \\ \gamma_{12} \\ \gamma_{23} \\ \gamma_{31} \end{pmatrix}, \tag{2.23}$$

where the omission of σ_{21}, σ_{32} and σ_{31} is due to symmetry of the stress tensor. In the case of an isotropic material behavior, the forth order elasticity tensor is expressed as

$$\mathbb{E} = \Lambda \mathbf{1} \otimes \mathbf{1} + 2\mu \mathbb{I}, \tag{2.24}$$

where Λ and μ are Lame constants, $\mathbf{1}$ is the second order identity tensor and $\mathbb{I}$ is the forth order identity tensor which is expressed as

$$\mathrm{I}_{ijkl} = \frac{1}{2}(\delta_{ik}\delta_{jl} + \delta_{il}\delta_{jk}). \tag{2.25}$$

The Lame constants may be expressed in terms of elastic modulus and Poisson's ratio

$$\Lambda = \frac{E\nu}{(1+\nu)(1-2\nu)} \quad \text{and} \quad \mu = \frac{E}{2(1+\nu)}, \tag{2.26}$$

and they may also be expressed in terms of bulk and shear modulus

$$\Lambda = K - \frac{2G}{3} \quad \text{and} \quad \mu = G. \tag{2.27}$$

For elastic isotropic behavior the forth order elastic tensor becomes

$$\mathbb{E} = \frac{E}{(1+\nu)(1-2\nu)} \begin{pmatrix} 1-\nu & \nu & \nu & 0 & 0 & 0 \\ \nu & 1-\nu & \nu & 0 & 0 & 0 \\ \nu & \nu & 1-\nu & 0 & 0 & 0 \\ 0 & 0 & 0 & \frac{1}{2}(1-2\nu) & 0 & 0 \\ 0 & 0 & 0 & 0 & \frac{1}{2}(1-2\nu) & 0 \\ 0 & 0 & 0 & 0 & 0 & \frac{1}{2}(1-2\nu) \end{pmatrix}, \tag{2.28}$$

where the decoupling between the deviatoric and volumetric response is observed. The previously mentioned relations are for a general three dimensional case where the material behavior is linear elastic and isotropic, for the two dimensional case, there are two different constitutive relations namely plane strain and plane stress.

Plane Strain

In the plane strain model it is assumed that the out of plane strains are zero, that is

$$\epsilon_{33} = 0, \quad \epsilon_{13} = 0, \quad \text{and} \quad \epsilon_{23} = 0 \tag{2.29}$$

and the out of plane shear stresses are zero

$$\sigma_{13} = 0, \quad \text{and} \quad \sigma_{23} = 0, \tag{2.30}$$

therefore the stress, strain and elastic tensors become

$$\boldsymbol{\sigma} = \begin{pmatrix} \sigma_{11} \\ \sigma_{22} \\ \sigma_{12} \end{pmatrix}, \quad \boldsymbol{\epsilon} = \begin{pmatrix} \epsilon_{11} \\ \epsilon_{22} \\ \gamma_{12} \end{pmatrix}, \quad \mathbb{E} = \frac{E}{(1+\nu)(1-2\nu)} \begin{pmatrix} 1-\nu & \nu & 0 \\ \nu & 1-\nu & 0 \\ 0 & 0 & \frac{1}{2}(1-2\nu) \end{pmatrix}, \tag{2.31}$$

where it should be noted that the out of plane stress σ_{33} is not zero and is expressed as

$$\sigma_{33} = \frac{E\nu}{(1+\nu)(1-2\nu)}(\epsilon_{11} + \epsilon_{22}). \tag{2.32}$$

Plane Stress

In the case of plane stress, the nonzero stresses are σ_{11}, σ_{22} and σ_{12} and the elastic tensor may be expressed as

$$\mathbb{E} = \frac{E}{1-\nu^2} \begin{pmatrix} 1 & \nu & 0 \\ \nu & 1 & 0 \\ 0 & 0 & \frac{1}{2}(1-\nu) \end{pmatrix} \tag{2.33}$$

and the out of plane shear strains ϵ_{23} and ϵ_{13} are zero while ϵ_{33} is not zero and is expressed as

$$\epsilon_{33} = -\frac{\nu}{E}(\sigma_{11} + \sigma_{22}). \tag{2.34}$$

In order to further investigate the material behavior it is worthwhile to briefly introduce the invariants of a second order tensor which will be extensively referred to in consequent chapters. A second order tensor $\boldsymbol{A}$ has three invariants that are constants and do not change by transformation of that tensor, these invariants are the first, second and third invariant of the tensor and are expressed as

$$
\begin{aligned}
I_1 &= \mathbf{1} : \boldsymbol{A} = A_{ii} \\
I_2 &= \frac{1}{2}\mathbf{1} : \boldsymbol{A}^2 = \frac{1}{2}\delta_{ij}A_{ik}A_{kj} \\
I_3 &= \frac{1}{3}\mathbf{1} : \boldsymbol{A}^3 = \frac{1}{3}\delta_{ij}A_{ik}A_{kl}A_{lj},
\end{aligned}
\tag{2.35}
$$

where the second order tensor $\boldsymbol{A}$ could be replaced by stress or strain tensor. In this work I_i represents the invariants of the stress tensor and $\hat{I}_i$ is used for invariants of strain tensor. The stress and strain tensors can be expressed in terms of deviatoric and volumetric parts in order to have a decoupling of volumetric and deviatoric response if desirable and are expressed as

$$\boldsymbol{s} = \boldsymbol{\sigma} - \frac{1}{3}(\mathbf{1} : \boldsymbol{\sigma})\mathbf{1} = \boldsymbol{\sigma} - \sigma_m\mathbf{1} = \boldsymbol{\sigma} - \frac{1}{3}I_1\mathbf{1} \quad \text{and} \tag{2.36a}$$

$$\boldsymbol{e} = \boldsymbol{\epsilon} - \frac{1}{3}(\mathbf{1} : \boldsymbol{\epsilon})\mathbf{1} = \boldsymbol{\epsilon} - \frac{1}{3}\epsilon_{vol}\mathbf{1} = \boldsymbol{\epsilon} - \frac{1}{3}\hat{I}_1\mathbf{1}, \tag{2.36b}$$

where, $\boldsymbol{s}$ is the deviatoric stress tensor and $\boldsymbol{e}$ is the deviatoric strain tensor. The invariants of the deviatoric stress and strain tensors are expressed by J_i and $\hat{J}_i$.

ELASTOPLASTIC MATERIAL BEHAVIOR

In the previous section, the linear elastic time independent isotropic material response was explained. As this material reaches its proportional or yield limit, it undergoes permanent deformation, i.e. in the case of unloading the stress-strain curve will not return to its original place, this behavior can be explained by plasticity theory. The onset of yielding for a material is defined by a function $F(\sigma_{ij})$. The material yields when $F(\sigma_{ij})$ is greater than zero and is in elastic region when $F(\sigma_{ij})$ is less than zero and is on the yield surface when $F(\sigma_{ij})$ is equal to zero. This function must hold for all the coordinate systems and therefore it is concluded that the yield

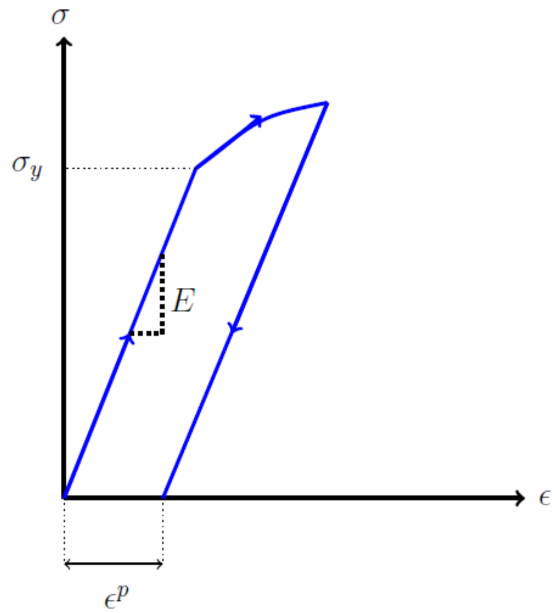

Figure 2.3: Loading and unloading of an elastoplastic material.

function is a function of stress invariants which is expressed as

$$F = F(I_1, I_2, I_3). \tag{2.37}$$

It is more convenient to write the yield function in the form

$$F = F(I_1, J_2, J_3) \quad \text{or} \quad F = F(I_1, J_2, \cos 3\theta), \tag{2.38}$$

where

$$\cos 3\theta = \frac{3\sqrt{3}}{2} \frac{J_3}{J_2^{3/2}}. \tag{2.39}$$

Before the reason for the term $\cos(3\theta)$ is discussed, different coordinate systems in which the yield surface is plotted are introduced. The so called Haigh-Westergaard coordinate system is the same as Cartesian coordinate system with axes σ_1, σ_2 and σ_3 where the spatial positions of a point are expressed in terms of ξ, ρ and θ. If a

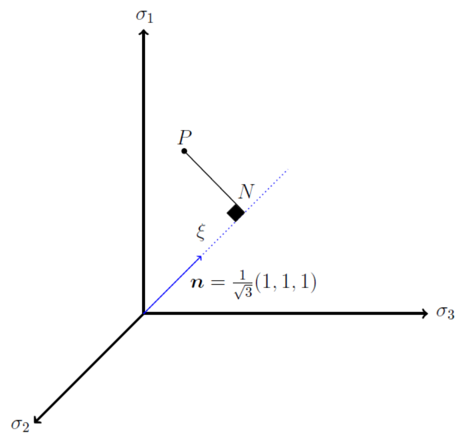

Figure 2.4: Haigh-Westergaard coordinate system.

stress point is located at space diagonal, all principal stresses are equal and therefore the space diagonal is called the hydrostatic axis and its unit vector is

$$\boldsymbol{n} = \frac{1}{\sqrt{3}}(1,1,1). \tag{2.40}$$

The plane perpendicular to the hydrostatic axis is called the deviatoric plane. Any stress point P, can also be expressed in terms of the coordinates ξ, ρ and θ, where ρ and θ are polar coordinates in the deviatoric plane and expressed as

$$\xi = \frac{I_1}{\sqrt{3}} \quad \text{and} \tag{2.41a}$$

$$\rho = \sqrt{2J_2}. \tag{2.41b}$$

It is also possible to depict the yield surface in a coordinate system with hydrostatic (ξ) and deviatoric (ρ) axes, the yield surface in this plane is achieved by intersecting the yield surface with a plane containing the hydrostatic axis, this plane is called the Rendulic plane and is depicted in figure (2.6). In plasticity, the total strain is additively decomposed into elastic and plastic strains as

$$\boldsymbol{\epsilon} = \boldsymbol{\epsilon}^e + \boldsymbol{\epsilon}^p, \tag{2.42}$$

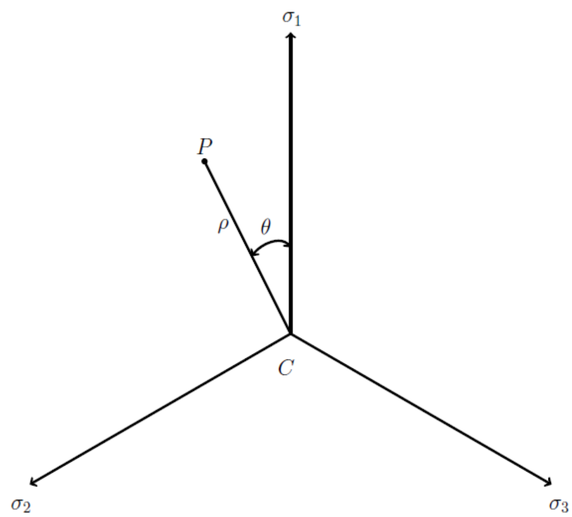

Figure 2.5: Deviatoric plane.

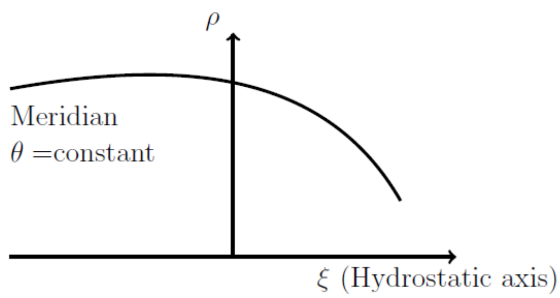

Figure 2.6: Rendulic plane, intersection of yield surface with the plane containing hydrostatic axis.

therefore the constitutive relation between stress and strain may be expressed as

$$\boldsymbol{\sigma} = \mathbb{E}^e : (\boldsymbol{\epsilon} - \boldsymbol{\epsilon}^p). \tag{2.43}$$

Assuming that $\mathbb{E}^e$ is constant, the rate of stresses are expressed as

$$\dot{\boldsymbol{\sigma}} = \mathbb{E}^e : (\dot{\boldsymbol{\epsilon}} - \dot{\boldsymbol{\epsilon}}^p), \tag{2.44}$$

where the material time derivative of the stress tensor is defined as

$$\dot{\boldsymbol{\sigma}} = \frac{\partial \boldsymbol{\sigma}}{\partial t}. \tag{2.45}$$

In order to account for hardening, softening or perfect plasticity, parameter K is introduced into the yield function

$$F(\boldsymbol{\sigma}, \underline{K}) = 0, \tag{2.46}$$

where $\underline{K}$ contains hardening/softening parameters and it may be scalar or vectorial based on the number of hardening/softening parameters, expressed as

$$\underline{K} = \underline{K}(\underline{\kappa}). \tag{2.47}$$

The hardening parameter is a function of internal variables $\underline{\kappa}$ and it is assumed in this work that the number of hardening parameters are the same as internal variables. In order to express the rate of plastic strain it is assumed that there exist a potential function G that has the same form as the yield function,

$$G = G(\boldsymbol{\sigma}, \boldsymbol{K}) \tag{2.48}$$

and the plastic flow is defined as

$$\dot{\boldsymbol{\epsilon}}^p = \dot{\lambda}\frac{\partial G}{\partial \boldsymbol{\sigma}}; \qquad \dot{\lambda} \geq 0. \tag{2.49}$$

The flow rule states that the direction of the plastic strain is expressed by the partial derivative term $(\frac{\partial G}{\partial \boldsymbol{\sigma}})$ and the plastic multiplier $\dot{\lambda}$ determines the magnitude of $\dot{\boldsymbol{\epsilon}}^p$. If the plastic potential function is equal to the yield function ($G = F$), it is said that the plasticity is associated and if they are different ($G \neq F$) the plasticity is non-associated. Now that the yield function and flow rules are defined, the Prager's consistency condition is introduced in equation (2.50), it states that during the development of plastic strain the yield criterion should be fulfilled, that is

$$\dot{F} = \frac{\partial F}{\partial \boldsymbol{\sigma}} : \dot{\boldsymbol{\sigma}} + \frac{\partial F}{\partial \underline{K}} \odot \dot{\underline{K}} = 0, \tag{2.50}$$

where the multiplication sign $\odot$ is used here because it is not yet known whether $\underline{K}$ is scalar or matrix and it assures the full contraction of the second term in equation (2.50). In this work it is assumed that the hardening and internal parameters are scalars. The evolution of the internal variable is defined as

$$\dot{\kappa} = -\dot{\lambda}\frac{\partial G}{\partial K}, \tag{2.51}$$

where G is substituted with F in case of associated plasticity. It is very important that the choice of yield and potential functions fulfill the second law of thermodynamics, i.e., the dissipation inequality or ClausiusâĂŞDuhem inequality

$$\boldsymbol{\sigma} : \dot{\boldsymbol{\epsilon}}^p - K\dot{\kappa} \geq 0. \tag{2.52}$$

In the above equations the first term has the dimension of the energy rate per unit volume and therefore the second term has the same dimension. It is said the $\boldsymbol{\sigma}$ is conjugated to $\dot{\boldsymbol{\epsilon}}^p$ because their product is an energy rate, therefore K and $\dot{\kappa}$ are conjugated as well. Equation (2.50) can be expressed in terms of the generalized plastic modulus H as

$$\dot{F} = \frac{\partial F}{\partial \boldsymbol{\sigma}} : \dot{\boldsymbol{\sigma}} - H\dot{\lambda} = 0, \tag{2.53}$$

where H may be expressed as

$$H = -\frac{\partial F}{\partial K}\frac{\partial K}{\partial \kappa}. \tag{2.54}$$

In order to simplify the equation of elastoplastic tangent operator the following

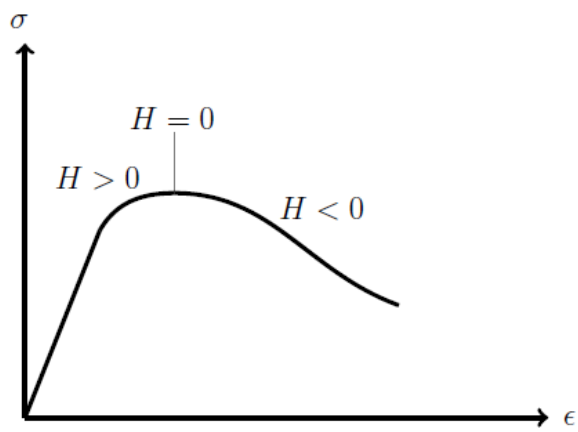

Figure 2.7: Hardening plasticity, perfect plasticity and softening plasticity.

notations are used

$$\boldsymbol{n} = \frac{\partial F}{\partial \boldsymbol{\sigma}} \quad \text{and} \tag{2.55a}$$

$$\boldsymbol{m} = \frac{\partial G}{\partial \boldsymbol{\sigma}}, \tag{2.55b}$$

where $\boldsymbol{n}$ and $\boldsymbol{m}$ are the normals to the yield and potential functions. Based on the above formulations, the plastic multiplier and elastoplastic stiffness tensor become

$$\dot{\lambda} = \frac{1}{H^p} \boldsymbol{n} : \mathbb{E} : \dot{\boldsymbol{\epsilon}} \quad \text{and} \tag{2.56}$$

$$\mathbb{E}^{ep} = \mathbb{E}^e - \frac{1}{H^p} \mathbb{E} : \boldsymbol{m} \otimes \boldsymbol{n} : \mathbb{E}, \tag{2.57}$$

where H^p is defined as

$$H^p = H + \boldsymbol{n} : \mathbb{E} : \boldsymbol{m}, \tag{2.58}$$

therefore the rate of elastoplastic constitutive relation takes the form of

$$\dot{\boldsymbol{\sigma}} = \mathbb{E}^{ep} : \dot{\boldsymbol{\epsilon}}. \tag{2.59}$$

The loading condition for elastoplastic material behavior is

$$\dot{\lambda} \geq 0\,, \quad F(\boldsymbol{\sigma}, K) \leq 0\,, \quad \dot{\lambda} F(\boldsymbol{\sigma}, K) = 0. \tag{2.60}$$

The rheological model to describe plasticity with hardening is depicted in figure (2.8), where H denotes the hardening parameter and r is for mixed hardening plasticity.

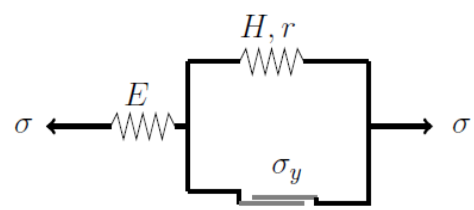

Figure 2.8: Rheological model for plasticity with hardening.

Based on this rheological model the general format of the free energy function for plasticity takes the form

$$\Psi = \Psi[\boldsymbol{\epsilon}, \boldsymbol{\epsilon}^p, \kappa, a], \tag{2.61}$$

where a is the internal parameter for kinematic hardening and it affects the yield function in the form of plastic parameter α as follow

$$F = F(\boldsymbol{\sigma}_{red}, K). \tag{2.62}$$

The free energy function for linear mixed isotropic-kinematic hardening takes the form

$$\Psi = \frac{1}{2}\boldsymbol{\epsilon}^e : \mathbb{E}^e : \boldsymbol{\epsilon}^e + \frac{1}{2}Hr\kappa^2 + \frac{1}{2}H(1-r)a^2, \tag{2.63}$$

where r determines how much of the hardening is due to isotropic hardening and how much is for kinematic hardening. In this dissertation only the isotropic hardening is used and therefore a and r are removed from the equations of this section.

In order to introduce appropriate yield functions for ductile and brittle materials, it is worthwhile to mention that it is assumed that the hydrostatic stress has little influence for ductile materials while it has strong influence for brittle materials. For initial yielding of metals, the yield surface depends on the deviatoric stresses and the material behaves similar in tension and compression. An appropriate way to describe this behavior is by von Mises criterion.

2.2.1 von Mises Criterion

This criterion is only dependent on the second invariant of deviatoric stress tensor and is completely independent of hydrostatic stresses and the third invariant.

$$F = F(J_2) = \sqrt{3J_2} - \sigma_{y0} = 0. \tag{2.64}$$

For the case of von Mises plasticity with linear isotropic hardening the yield function

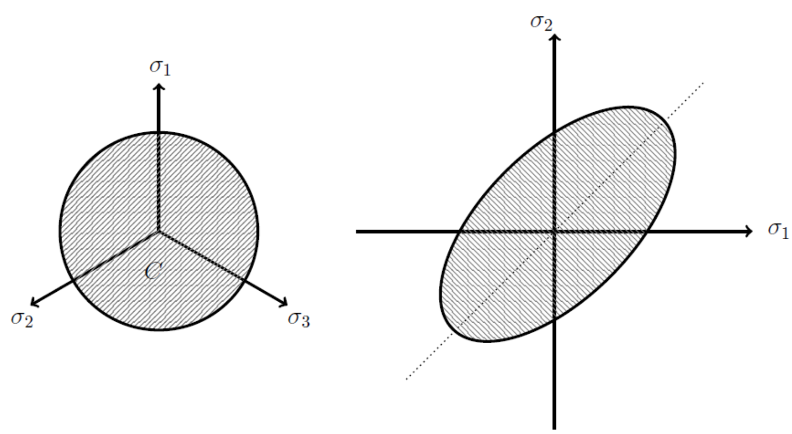

Figure 2.9: von Mises criterion in the deviatoric and $\sigma_1 - \sigma_2$ plane.

becomes

$$F = F(J_2) = \sqrt{3J_2} - \sigma_y(K) = 0 \Longrightarrow F(J_2) = \sqrt{3J_2} - (\sigma_{y0} + K) = 0, \tag{2.65}$$

where for linear hardening

$$K = -\int H\dot{\kappa}, \tag{2.66}$$

and the normal to the yield function takes the form

$$\boldsymbol{n} = \frac{\partial F}{\partial \boldsymbol{\sigma}} = \frac{\sqrt{3}}{2}\frac{\boldsymbol{s}}{\sqrt{J_2}}. \tag{2.67}$$

2.2.2 Drucker-Prager Criterion

Drucker and Prager (1952) criteria is used to describe the yielding of materials like concrete, soil and rocks. In this yield function the hydrostatic stress I_1 is of high importance and it is described as

$$F = F(I_1, J_2) = \sqrt{3J_2} + \alpha I_1 - \beta = 0, \tag{2.68}$$

where α and β are material parameters related to cohesion and friction, α is dimensionless and β has the units of stress and they are determined based on yield stresses of the material in tension and compression,

$$\alpha = \frac{f_c - f_t}{f_c + f_t}, \quad \beta = \frac{2 f_c f_t}{f_c + f_t}. \tag{2.69}$$

From figure (2.10) it is observed that the Drucker-Prager yield surface is conical and the diameter of the circle in the deviatoric plane decreases as the hydrostatic stress increases. The normal to the yield function ($\boldsymbol{n}$) is defined as

$$\boldsymbol{n} = \frac{\partial F}{\partial \boldsymbol{\sigma}} = \frac{\partial F}{\partial I_1}\frac{\partial I_1}{\partial \boldsymbol{\sigma}} + \frac{\partial F}{\partial J_2}\frac{\partial J_2}{\partial \boldsymbol{\sigma}} = \alpha \mathbf{1} + \frac{\sqrt{3}}{2}\frac{\boldsymbol{s}}{\sqrt{J_2}}. \tag{2.70}$$

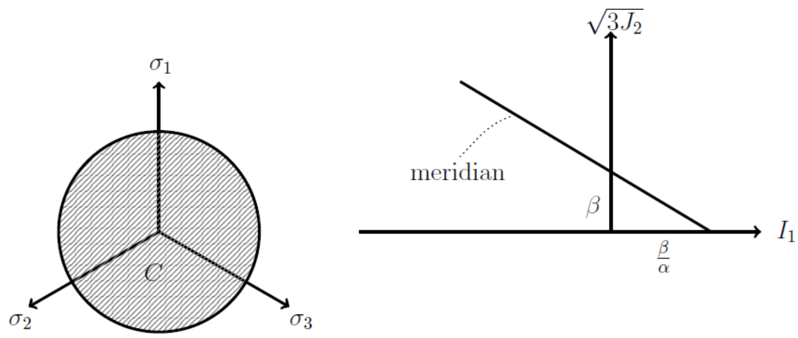

Figure 2.10: Drucker-Prager criterion in the deviatoric and Rendulic plane.

2.2.3 Tresca Criterion

Tresca Tresca (1864) assumes that yielding in ductile material occurs when the maximum shear stress achieves a certain limit, this is described by

$$|\ \tau\ |= \frac{\sigma_{y0}}{2} \quad \Longrightarrow F = \sigma_1 - \sigma_3 - \sigma_{y0} = 0, \tag{2.71}$$

where based on Mohr's circle τ is described as

$$\tau = \frac{\sigma_1 - \sigma_3}{2}, \quad \sigma_1 > \sigma_2 > \sigma_3, \tag{2.72}$$

where σ_i is the principal stress. This criteria forms a hexagonal surface which has the same shape along the hydrostatic axis.

The normal to the yield function becomes

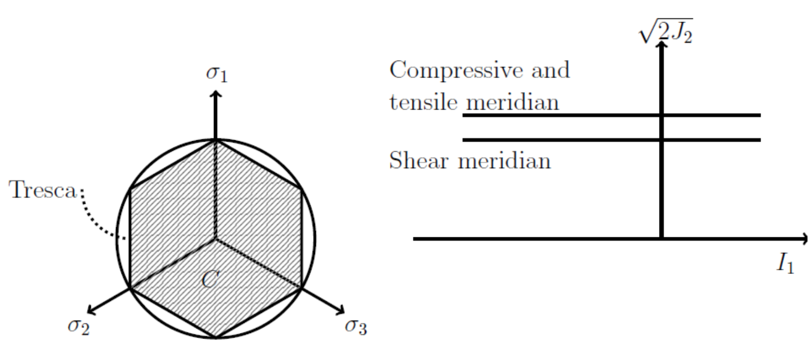

Figure 2.11: Tresca criterion in the deviatoric and Rendulic plane.

$$\boldsymbol{n} = \frac{\partial F}{\partial \boldsymbol{\sigma}} = [\frac{\sqrt{2}}{2} \quad 0 \quad \frac{\sqrt{2}}{2}]^T, \tag{2.73}$$

where it is concluded that the normal to the yield surface is 45 degrees inclined with respect to principal coordinates.

2.2.4 Willam-Warnke Criterion

The Willam and Warnke (1975) yield surface is a three invariant yield surface that is conical with curved meridians and has a non-circular section which varies along the hydrostatic axis. In this dissertation the Menétrey and Willam (1995) format of the yield surface is described and it is expressed in terms of the Haigh-Westergaard coordinates,

$$F(\xi, \rho, \theta) = \left(\sqrt{1.5}\frac{\rho}{K(\kappa) f_c}\right)^2 + m\left(\frac{\rho}{\sqrt{6}K(\kappa) f_c} r(\theta, e) + \frac{\xi}{\sqrt{3}K(\kappa) f_c}\right) - c(\kappa) = 0. \tag{2.74}$$

In equation (2.74) K is the hardening and κ is the internal plastic parameter and

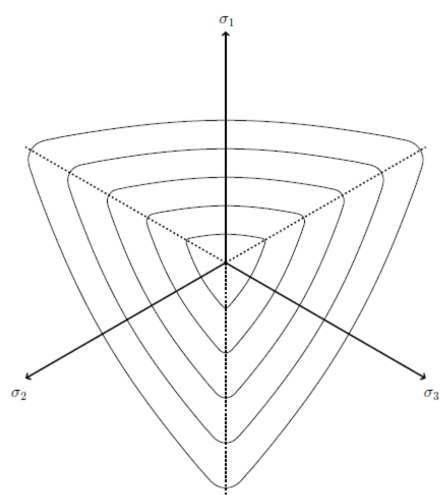

Figure 2.12: Willam-Warnke yield surface in deviatoric plane for varying hydrostatic stress.

the parameters m and r are defined as

$$m = 3\frac{(K(\kappa)f_c)^2 - (\lambda_t f_t)^2}{K(\kappa)f_c\lambda_t f_t}\frac{e}{e+1} \quad \text{and} \tag{2.75a}$$

$$r(\theta, e) = \frac{4(1-e^2)\cos^2\theta + (2e-1)^2}{2(1-e^2)\cos\theta + (2e-1)[4(1-e^2)\cos^2\theta + 5e^2 - 4e]^{1/2}}, \tag{2.75b}$$

where λ_t is a scaling factor for the tensile concrete strength and e is a parameter that defines the roundness of the yield surface. The parameter c controls the softening or the hardening of the yield surface. The normal to the yield surface is expressed as

$$\boldsymbol{n} = \frac{\partial F}{\partial \boldsymbol{\sigma}} = \frac{\partial F}{\partial \xi}\frac{\partial \xi}{\partial \boldsymbol{\sigma}} + \frac{\partial F}{\partial \rho}\frac{\partial \rho}{\partial \boldsymbol{\sigma}} + \frac{\partial F}{\partial \theta}\frac{\partial \theta}{\partial \boldsymbol{\sigma}}, \tag{2.76}$$

where the derivatives of the yield function with respect to the Haigh-Westergaard coordinates are expressed as

$$\frac{\partial F}{\partial \xi} = \frac{m}{\sqrt{3}K(\kappa)f_c}, \tag{2.77a}$$

$$\frac{\partial F}{\partial \rho} = \frac{3\rho}{K^2(\kappa)f_c^2} + \frac{m r(\theta, e)}{\sqrt{6}K(\kappa)f_c} \quad \text{and} \tag{2.77b}$$

$$\frac{\partial F}{\partial \theta} = \frac{m\rho}{\sqrt{6}K(\kappa)f_c}\frac{\partial r(\theta, e)}{\partial \theta}. \tag{2.77c}$$

The derivative of $r(\theta, e)$ with respect to θ is defines as

$$\begin{aligned}\frac{\partial r(\theta, e)}{\partial \theta} &= \frac{(-4(1-e^2)\sin 2\theta) * P_1}{P_1^2} \\ &- \frac{(-2(1-e^2)\sin\theta + 0.5(2e-1)[4(1-e^2)\cos^2\theta + 5e^2 - 4e]^{-1/2}(-4(1-e^2)\sin 2\theta)) * P_2}{P_1^2},\end{aligned} \tag{2.78}$$

where the term P_1 is defined as

$$P_1 = 2(1-e^2)\cos\theta + (2e-1)[4(1-e^2)\cos^2\theta + 5e^2 - 4e]^{1/2} \tag{2.79}$$

and the term P_1 is defined as

$$P_2 = 4(1 - e^2)\cos^2\theta + (2e - 1)^2. \tag{2.80}$$

The derivatives of ξ, ρ and θ with respect to $\boldsymbol{\sigma}$ are expressed as follow

$$\frac{\partial \xi}{\partial \boldsymbol{\sigma}} = \frac{\mathbf{1}}{\sqrt{3}}, \tag{2.81a}$$

$$\frac{\partial \rho}{\partial \boldsymbol{\sigma}} = \frac{\sqrt{2}\boldsymbol{s}}{2\sqrt{J_2}} \quad \text{and} \tag{2.81b}$$

$$\frac{\partial \theta}{\partial \boldsymbol{\sigma}} = \frac{\partial \theta}{\partial \cos 3\theta}\frac{3\sqrt{3}}{2}\frac{(\boldsymbol{s}^2 - \frac{2}{3}J_2\mathbf{1})J_2^{3/2} - \frac{3}{2}J_2^{1/2}J_3\boldsymbol{s}}{J_2^3}, \tag{2.81c}$$

where

$$\frac{\partial \theta}{\partial \cos 3\theta} = -\frac{1}{3\sqrt{1 - \cos^2 3\theta}}. \tag{2.82}$$

2.2.5 Rankine Criterion, St. Venant's Criterion

Rankine [1820-1872] criterion is mostly used for brittle material behavior and it assumes that yielding occurs when the principal stress achieves a certain value, for this reason it is called the maximum principal stress criterion,

$$F = \sigma_1 - \sigma_{y0} = 0. \tag{2.83}$$

In this criterion the normal to the yield criterion is parallel to the direction of maximum principal stress. The St. Venant's [1797-1886] criterion is similar to the Rankine criterion except that the yield function is expressed in terms of principal strains, therefore it is called the maximum principal strain criterion,

$$F = \epsilon_1 - \epsilon_{y0} = 0. \tag{2.84}$$

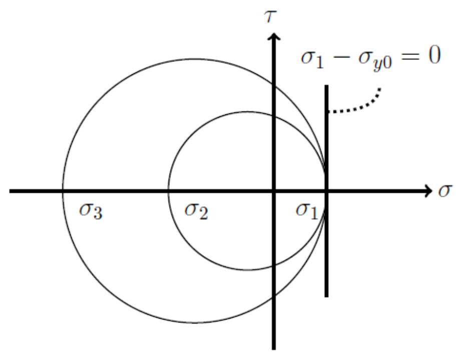

Figure 2.13: Rankine criterion.

This condition provides a cut off condition that can be preceded with plasticity, damage and degradation of the material.

DAMAGE-PLASTICITY

In this section, the damage-plasticity formulations that are used to model concrete behavior are discussed. Two plasticity models of Drucker-Prager and Willam-Warnke are used in order to account for the permanent deformation that retains inside the deteriorated material while the scalar isotropic damage model accounts for the deterioration of the elastic stiffness. At First the damage-plasticity model based on Drucker-Prager model is discussed which is derived by Salari et al. (2004). In this model it is assumed that the plasticity and damage have different loading functions and damage enters the plasticity yield function in terms of effective stresses. For the case of Willam-Warnke plasticity and damage, Menétrey and Willam (1995) format of this yield function which is described by Cervenka and Papanikolaou (2008) is used and the scalar damage is used to model the degradation of the material.

2.3.1 Drucker-Prager and Scalar Damage

The Helmholtz free enery function for this model is

$$\psi = \psi^e(\boldsymbol{\epsilon}^e, D) + \psi^p(\bar{e}^p, D) \tag{2.85}$$

and the Clausius-Duhem inequality takes the form

$$\left(\boldsymbol{\sigma} - \frac{\partial \psi^e}{\partial \boldsymbol{\epsilon}^e}\right) : \dot{\boldsymbol{\epsilon}} + \frac{\partial \psi^e}{\partial \boldsymbol{\epsilon}^e} : \dot{\boldsymbol{\epsilon}}^p - \frac{\partial \psi^e}{\partial \bar{e}^p}\dot{\bar{e}}^p - \frac{\partial \psi^e}{\partial D}\dot{D} \geq 0. \tag{2.86}$$

The pressure sensitive yield function of the Drucker-Prager is expressed as

$$F^p(\boldsymbol{\sigma}, \bar{e}^p, D) = \alpha I_1 + \sqrt{J_2} - (1 - D)K, \tag{2.87}$$

where $\bar{e}^p$ is the effective deviatoric plastic strain, and the term $(1 - D)$ is multiplied by the cohesive resistance of the yield function. α and K may be expressed in terms of uniaxial tensile and compressive strength as

$$\alpha = \frac{1}{\sqrt{3}}\frac{f_c - f_t}{f_c + f_t} \quad \text{and} \tag{2.88a}$$

$$K = \frac{2}{\sqrt{3}}\frac{f_c f_t}{f_c + f_t}. \tag{2.88b}$$

It is worthwhile to mention that if equation (2.87) is divided by $(1 - D)$ the stresses would become the effective stresses. The plastic hardening is assumed to be only dependant on the equivalent deviatoric plastic strain, and the material parameters are expressed in terms of exponential functions proposed by Shao et al. (1998)

$$\alpha = \alpha_m - (\alpha_m - \alpha_0)e^{-b_1 \bar{e}^p} \quad \text{and} \tag{2.89a}$$

$$K = K_m - (K_m - K_0)e^{-b_2 \bar{e}^p}, \tag{2.89b}$$

where subscripts 0 and m denote the initial and maximum values of frictional and cohesive parameters. In this model it is assumed that the volumetric part of the plastic strain does not affect the hardening and it only enters the damage formulation and therefore controlling the softening. It is also possible to introduce adequate softening law to the Drucker-Prager formulation in order to increase the amount of permanent deformation of the material behavior if it is necessary, the softening law proposed in this dissertation is

$$K_s = \left(\frac{\log\left(\bar{e}^p\right)}{\log\left(\bar{e}^p_0\right)} \right) K_{hm}, \tag{2.90}$$

where K_{hm} is the maximum value of hardening variable at the transition between hardening and softening and $\bar{e}^p_0$ is the amount of effective deviatoric plastic strain at the onset of softening. In summary the hardening/softening law may be expressed as follow:

$$K_h = K_m - (K_m - K_0)e^{-b_2\bar{e}^p}, \tag{2.91a}$$

$$K_s = \left(\frac{\log(\bar{e}^p)}{\log(\bar{e}^p_0)} \right) K_{hm} \quad \text{and} \tag{2.91b}$$

$$K = \mathrm{H}(p_2 - \epsilon)K_h + \mathrm{H}(\epsilon - p_2)K_s, \tag{2.91c}$$

where p_2 is a material parameter defining the transition of hardening to softening and H is the heaviside function. The plastic potential is described as

$$G^p(\boldsymbol{\sigma}, \bar{e}^p) = \beta I_1 + \sqrt{J_2}, \tag{2.92}$$

where β is the cohesive resistance of the potential function and defines whether the formulation is associative or non-associative plasticity. The rate of the plastic strain is defined as

$$\dot{\boldsymbol{\epsilon}}^p = \dot{\lambda}\frac{\partial G^p}{\partial \boldsymbol{\sigma}} \tag{2.93}$$

and therefore, the volumetric and deviatoric parts of the plastic strain become

$$\dot{\epsilon}^p_m = \dot{\lambda}\beta, \tag{2.94a}$$

$$\dot{\boldsymbol{e}}^p = \dot{\lambda}\frac{\boldsymbol{s}}{2\sqrt{J_2}}, \tag{2.94b}$$

and therefore

$$\dot{\bar{e}}^p = \sqrt{\frac{2}{3}\dot{\boldsymbol{e}}^p : \dot{\boldsymbol{e}}^p} = \frac{\dot{\lambda}}{\sqrt{3}}. \tag{2.95}$$

Prager's consistency condition assures that stress state remains on the yield surface during loading and it is expressed as

$$\dot{F}^p = \boldsymbol{n} : \dot{\boldsymbol{\sigma}} + \frac{\partial F^p}{\partial \bar{e}^p}\dot{\bar{e}}^p + \frac{\partial F^p}{\partial D}\dot{D} = 0, \tag{2.96}$$

where $\boldsymbol{n}$ is normal to the yield surface and $\dot{\boldsymbol{\sigma}}$ is expressed as,

$$\dot{\boldsymbol{\sigma}} = \mathbb{E}^d : \boldsymbol{\epsilon}^e + \dot{\mathbb{E}}^d : \boldsymbol{\epsilon}^e \tag{2.97}$$

and $\mathbb{E}^d$ is the secant tensor of elastic damage and is given by

$$\mathbb{E}^d = (1 - D)\mathbb{E}^e. \tag{2.98}$$

Therefore equation (2.97) can be reformulated as

$$\dot{\boldsymbol{\sigma}} = \mathbb{E}^d : \left(\boldsymbol{\epsilon} - \dot{\lambda}\boldsymbol{m}\right) - \dot{D}\mathbb{E}^e : \boldsymbol{\epsilon}^e, \tag{2.99}$$

where $\boldsymbol{m}$ is the normal to the plastic potential. The plastic consistency condition can be expressed in terms of the plastic multiplier and damage rate as follow

$$\left(\boldsymbol{n} : \mathbb{E}^d : \boldsymbol{m} - \frac{\partial F^p}{\partial \bar{e}^p}\frac{1}{\sqrt{3}}\right)\dot{\lambda} + \left(\frac{\partial F^p}{\partial \boldsymbol{\sigma}} : \mathbb{E}^e : \boldsymbol{\epsilon}^e - \frac{\partial F^p}{\partial D}\right)\dot{D} = \frac{\partial F^p}{\partial \boldsymbol{\sigma}} : \mathbb{E}^d : \dot{\boldsymbol{\epsilon}}. \tag{2.100}$$

The damage function is expressed in terms of the volumetric strain and it assumes that the deterioration of the material is only due to the expansive volumetric strains and it is expressed as

$$Y_v = \frac{1}{2}K^0\langle\epsilon_v^e\rangle^2 + c\int_0^{\epsilon_v^p} |\sigma_m|\langle \mathrm{d}\epsilon_v^p\rangle, \tag{2.101}$$

where K^0 is the initial bulk modulus and c has different values for tension and compression and it determines the amount of coupling of the dilatant volumetric plastic energy dissipation. The damage function is described in terms of energy and is formulated as

$$F^d(Y_v, D) = Y_v - r(D), \tag{2.102}$$

where $r(D)$ is the energy resistance function and may be expressed in terms of a power function as

$$r(D) = r_0(1-D)^{p-1}, \tag{2.103}$$

where r_0 is the modulus of resilience and is defined as the volumetric strain energy at peak stress in uniaxial tension and p represents the ratio of modulus of resilience and modulus of toughness which is expressed as

$$p = \frac{r_0}{g_f}. \tag{2.104}$$

The damage consistency condition based on Prager's consistency condition is formulated as

$$\dot{F}^d = \frac{\partial F^d}{\partial Y_v}\dot{Y}_v + \frac{\partial F^d}{\partial D}\dot{D}, \tag{2.105}$$

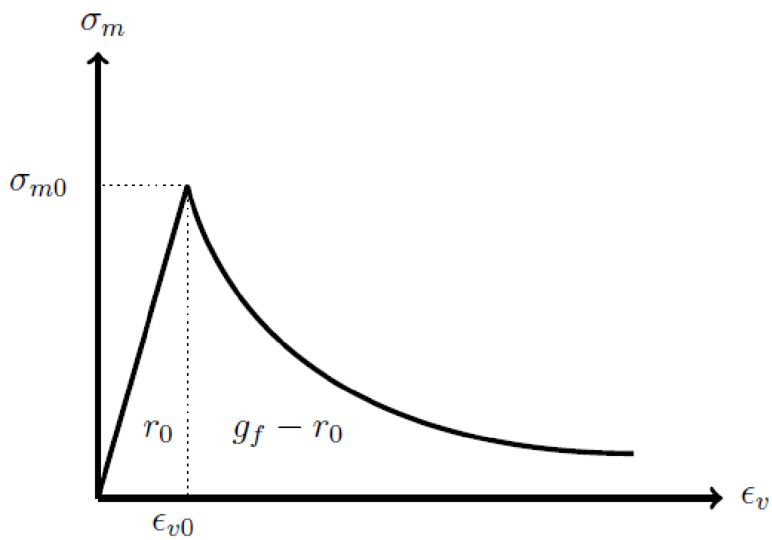

Figure 2.14: Uniaxial stress-strain curve of the damage model.

where

$$\dot{Y}_v = K^0 \langle \epsilon_v^e \rangle \mathbf{1} : \dot{\boldsymbol{\epsilon}} - 3\dot{\lambda} \left(K^0 \langle \epsilon_v^e \rangle \frac{\partial G^p}{\partial I_1} - c|\sigma_m| \langle \frac{\partial G^p}{\partial I_1} \rangle \right) \tag{2.106}$$

and Macaulay brackets $\langle \rangle$ are defined as

$$\begin{aligned} \langle x \rangle = x \qquad & \forall x > 0 \quad \text{and} \\ \langle x \rangle = 0 \qquad & \forall x \leq 0. \end{aligned} \tag{2.107}$$

Finally by substituting equation (2.106) into (2.105) the second consistency condition becomes

$$-3R_d \left(K^0 \langle \epsilon_v^e \rangle \frac{\partial G^p}{\partial I_1} - c|\sigma_m| \langle \frac{\partial G^p}{\partial I_1} \rangle \right) \dot{\lambda} + \dot{D} - R_d K^0 \langle \epsilon_v^e \rangle \mathbf{1} : \dot{\boldsymbol{\epsilon}} = 0, \tag{2.108}$$

where R_d is defined as

$$R_d = \frac{\frac{\partial F^d}{\partial Y_v}}{\frac{\partial F^d}{\partial D}} \quad \text{with} \quad R_d < 0. \tag{2.109}$$

The formulation of damage and plasticity with different loading functions is similar to multi-surface plasticity models and equations (2.100) and (2.109) may be combined to form the matrix format of the consistency condition,

$$\begin{pmatrix} A_{11} & A_{12} \\ A_{21} & A_{22} \end{pmatrix} \begin{pmatrix} \dot{\lambda} \\ \dot{D} \end{pmatrix} = \begin{pmatrix} B_1 \\ B_2 \end{pmatrix}. \tag{2.110}$$

The plastic multiplier and damage rate are expressed as follow

$$\begin{pmatrix} \dot{\lambda} \\ \dot{D} \end{pmatrix} = \frac{1}{A_{11}A_{22} - A_{12}A_{21}} \begin{pmatrix} A_{22} & -A_{12} \\ -A_{21} & A_{11} \end{pmatrix} = \begin{pmatrix} B_1 \\ B_2 \end{pmatrix} \tag{2.111}$$

and finally the loading conditions requires that the coefficient matrix must be positive, A_{11} has to be positive for plasticity, A_{22} has to be positive for damage loading and $A_{11}A_{22} > A_{12}A_{21}$ should hold for combined loading together with

$$\dot{D} > 0 \quad \text{if} \quad A_{11}B_2 - A_{21}B_1 > 0 \quad \text{and} \tag{2.112a}$$

$$\dot{\lambda} > 0 \quad \text{if} \quad A_{22}B_1 - A_{12}B_2 > 0. \tag{2.112b}$$

Now that the background formulations for plasticity, damage and the coupling between these models is described, an implicit backward Euler method in conjunction with Newton-Raphson method is used to find the updated values of the unknown which is explicitly explained and presented in the following chapters.

The elastoplastic damage tangent operator can be achieved analytically based on the aforementioned equations and it has three formats based on the loading conditions, it could be elastodamage, elastoplastic and elastoplastic damage. In the absence of the plasticity the elastodamge tangent operator is expressed as

$$\mathbb{E}^{ed} = \mathbb{E}^{d} + R_d K^0 \langle \epsilon_v^e \rangle \mathbf{1} \otimes (\mathbb{E}^e : \boldsymbol{\epsilon}^e) \tag{2.113}$$

and in the absence of damage the elastoplastic tangent operator becomes

$$\mathbb{E}^{ep} = \mathbb{E}^e - \frac{\mathbb{E}^e : \boldsymbol{n} \otimes \boldsymbol{m} : \mathbb{E}^e}{\boldsymbol{n} : \mathbb{E}^e : \boldsymbol{m} - \frac{\partial F^p}{\partial \bar{e}^p}\frac{1}{\sqrt{3}}} \tag{2.114}$$

where $\boldsymbol{n}$ and $\boldsymbol{m}$ are the normals to the yield and plastic potential. The elastoplastic damage tangent operator is expressed as

$$\mathbb{E}^{epd} = \mathbb{E}^d + R_d K^0 \langle \epsilon_v^e \rangle \mathbf{1} \otimes (\mathbb{E}^e : \boldsymbol{\epsilon}^e) - \frac{\left(\mathbb{E}^d : \boldsymbol{n} + R_d(\boldsymbol{n} : \mathbb{E}^e : \boldsymbol{\epsilon}^e - \frac{\partial F^p}{\partial D})K^0\langle \epsilon_v^e \rangle \mathbf{1}\right) \otimes \left(\mathbb{E}^d : \boldsymbol{m} + 3R_d\left(K^0 \langle \epsilon_v^e \rangle \frac{\partial G^p}{\partial I_1} - c|\sigma_m|\langle \frac{\partial G^p}{\partial I_1}\rangle\right)\mathbb{E}^e : \boldsymbol{\epsilon}^e\right)}{\left(\boldsymbol{n} : \mathbb{E}^d : \boldsymbol{m} - \frac{\partial F^p}{\partial \bar{e}^p}\frac{1}{\sqrt{3}} + 3R_d(\boldsymbol{n} : \mathbb{E}^e : \boldsymbol{\epsilon}^e - \frac{\partial F^p}{\partial D})\left(K^0\langle \epsilon_v^e \rangle \frac{\partial G^p}{\partial I_1} - c|\sigma_m|\langle \frac{\partial G^p}{\partial I_1}\rangle\right)\right)} \tag{2.115}$$

and this is used in order to assemble the global stiffness matrix of the finite element model and to check the global equilibrium conditions.

2.3.2 Willam-Warnke and Scalar Damage

The Helmholtz free energy function has the same form as of the Drucker-Prager plasticity and is

$$\psi = \psi^e(\boldsymbol{\epsilon}^e, D) + \psi^p(\kappa, D) \tag{2.116}$$

and the Clasius-Duhem inequality becomes

$$\left(\boldsymbol{\sigma} - \frac{\partial \psi^e}{\partial \boldsymbol{\epsilon}^e}\right) : \dot{\boldsymbol{\epsilon}} + \frac{\partial \psi^e}{\partial \boldsymbol{\epsilon}^e} : \dot{\boldsymbol{\epsilon}}^p - \frac{\partial \psi^e}{\partial \kappa}\dot{\kappa} - \frac{\partial \psi^e}{\partial D}\dot{D} \geq 0. \tag{2.117}$$

In this model the Menétrey and Willam (1995) format of the Willam-Warnke plasticity model is used, while the damage formulation is kept similar to the one used in connection with Drucker-Prager model. The damage parameter enters the plastic yield function in the form of effective stresses and then this function is multiplied by the term $(1-D)^2$ which takes the form

$$F(\xi,\rho,\theta,D) = \left(\sqrt{1.5}\frac{\rho}{K(\kappa)f_c}\right)^2 + (1-D)m\left(\frac{\rho}{\sqrt{6}K(\kappa)f_c}r(\theta,e) + \frac{\xi}{\sqrt{3}K(\kappa)f_c}\right) - (1-D)^2c(\kappa) = 0, \tag{2.118}$$

where as explained in the theory section, this yield function is presented in terms of Haigh-Westergaard coordinate system, m is the cohesion parameter of the material, $r(\theta,e)$ is a function of θ and e where e defines the roundness of the failure surface,

$$m = 3\frac{(K(\kappa)f_c)^2 - (\lambda_t f_t)^2}{K(\kappa)f_c\lambda_t f_t}\frac{e}{e+1} \quad \text{and} \tag{2.119a}$$

$$r(\theta,e) = \frac{4(1-e^2)\cos^2\theta + (2e-1)^2}{2(1-e^2)\cos\theta + (2e-1)[4(1-e^2)\cos^2\theta + 5e^2 - 4e]^{1/2}}. \tag{2.119b}$$

The hardening variable K is a function of the internal parameter κ that is a function of the volumetric plastic strain, that is in contrast to the hardening variable of the Drucker-Prager formulation, where the internal hardening parameter is a function of effective deviatoric plastic strain,

$$K(\kappa) = K(\epsilon_v^p) = K_0 + (1-K_0)\sqrt{1 - \left(\frac{\epsilon_{v,t}^p - \epsilon_v^p}{\epsilon_{v,t}^p}\right)^2}, \tag{2.120}$$

where $\epsilon_{v,t}^p$ is the volumetric plastic strain at uniaxial material strength and K_0 is the initial value of the hardening which defines the initial yield surface. The function $c(\kappa)$ controls the softening branch of the material behavior and it simulates the decohesion of the material as

$$c(\kappa) = c(\epsilon_v^p) = \left(\frac{1}{1 + \left(\frac{n_1-1}{n_2-1}\right)^2}\right)^2, \tag{2.121}$$

where n_1 and n_2 are functions of volumetric plastic strain defined as

$$n_1 = \frac{\epsilon_v^p}{\epsilon_{v,t}^p} \quad \text{and} \tag{2.122a}$$

$$n_2 = \frac{\epsilon_{v,t}^p + t}{\epsilon_{v,t}^p} \tag{2.122b}$$

and the parameter t controls the slope of the softening branch. In the case of the non-associated flow rule, the Drucker-Prager plastic potential is used and is defined as

$$G^p = \beta I_1 + \sqrt{J_2} \tag{2.123}$$

and therefore recalling from the plasticity theory the rate of plastic strain and internal plastic variable become

$$\dot{\epsilon}^p = \dot{\lambda}\frac{\partial G^p}{\partial \boldsymbol{\sigma}} \quad \text{and} \tag{2.124}$$

$$\dot{\kappa} = -\dot{\lambda}\frac{\partial G^p}{\partial K}. \tag{2.125}$$

The Prager's consistency condition for this yield envelope becomes

$$\dot{F}^p = \frac{\partial F^p}{\partial \boldsymbol{\sigma}} : \dot{\sigma} + \frac{\partial F^p}{\partial \epsilon_v^p}\dot{\epsilon}_v^p + \frac{\partial F^p}{\partial D}\dot{D} = 0, \tag{2.126}$$

where $\dot{\boldsymbol{\sigma}}$ may be expressed as

$$\dot{\boldsymbol{\sigma}} = \mathbb{E}^d : \left(\dot{\boldsymbol{\epsilon}} - \dot{\lambda}\boldsymbol{m}\right) - \dot{D}\mathbb{E}^e : \boldsymbol{\epsilon}^e \tag{2.127}$$

and the volumetric plastic strain rate is given by

$$\dot{\epsilon}_v^p = \mathbf{1} : \dot{\boldsymbol{\epsilon}}^p = \dot{\lambda}\mathbf{1} : \left(\beta\mathbf{1} + \frac{1}{2}\frac{\boldsymbol{s}}{\sqrt{J_2}}\right) = 3\dot{\lambda}\beta \tag{2.128}$$

and finally the consistency condition in terms of plastic multiplier and damage rate become

$$\left(\boldsymbol{n} : \mathbb{E}^d : \boldsymbol{m} - 3\frac{\partial F^p}{\partial \epsilon_v^p}\beta\right)\dot{\lambda} + \left(\boldsymbol{n} : \mathbb{E}^e : \boldsymbol{\epsilon}^e - \frac{\partial F^p}{\partial D}\right)\dot{D} = \boldsymbol{n} : \mathbb{E}^d : \dot{\boldsymbol{\epsilon}}. \tag{2.129}$$

The damage formulation is the same as the one used for Drucker-Prager plasticity model and therefore the second consistency condition based on damage function is expressed as

$$-3R_d\left(K^0\langle\epsilon_v^e\rangle\frac{\partial G^p}{\partial I_1} - c|\sigma_m|\langle\frac{\partial G^p}{\partial I_1}\rangle\right)\dot{\lambda} + \dot{D} - R_d K^0\langle\epsilon_v^e\rangle\mathbf{1} : \dot{\boldsymbol{\epsilon}} = 0. \tag{2.130}$$

The structure of this damage-plasticity model is the same as the one described in the last section. Finally the elastodamage, elastoplastic and elastoplastic tangent operators are expressed in the equations (2.131), (2.132) and (2.133) respectively. In the absence of the plasticity the elastodamge tangent operator is expressed as

$$\mathbb{E}^{ed} = \mathbb{E}^d + R_d K^0\langle\epsilon_v^e\rangle\mathbf{1}\otimes(\mathbb{E}^e : \boldsymbol{\epsilon}^e). \tag{2.131}$$

The elastoplastic tangent operator becomes

$$\mathbb{E}^{ep} = \mathbb{E}^e - \frac{\mathbb{E}^e : \boldsymbol{n}\otimes\boldsymbol{m} : \mathbb{E}^e}{\boldsymbol{n} : \mathbb{E}^e : \boldsymbol{m} - 3\beta\frac{\partial F^p}{\partial \epsilon_v^p}} \tag{2.132}$$

and in the presence of damage and plasticity the elastoplastic damage tangent operator is expressed as

$$\mathbb{E}^{epd} = \mathbb{E}^d + R_d K^0\langle\epsilon_v^e\rangle\mathbf{1}\otimes(\mathbb{E}^e : \boldsymbol{\epsilon}^e) - \frac{\left(\mathbb{E}^d : \boldsymbol{n} + R_d(\boldsymbol{n} : \mathbb{E}^e : \boldsymbol{\epsilon}^e - \frac{\partial F^p}{\partial D})K^0\langle\epsilon_v^e\rangle\mathbf{1}\right)\otimes\left(\mathbb{E}^d : \boldsymbol{m} + 3R_d\left(K^0\langle\epsilon_v^e\rangle\frac{\partial G^p}{\partial I_1} - c|\sigma_m|\langle\frac{\partial G^p}{\partial I_1}\rangle\right)\mathbb{E}^e : \boldsymbol{\epsilon}^e\right)}{\boldsymbol{n} : \mathbb{E}^d : \boldsymbol{m} - 3\beta\frac{\partial F^p}{\partial \epsilon_v^p} + 3R_d(\boldsymbol{n} : \mathbb{E}^e : \boldsymbol{\epsilon}^e - \frac{\partial F^p}{\partial D})\left(K^0\langle\epsilon_v^e\rangle\frac{\partial G^p}{\partial I_1} - c|\sigma_m|\langle\frac{\partial G^p}{\partial I_1}\rangle\right)}, \tag{2.133}$$

where the second term is considering the damage contribution and the third term is the combination of damage and plasticity.

Chapter 3. Failure Diagnostics

Discrete failure of a material is preceded by a hierarchy of kinematic deterioration of the continuum into a discontinuum. This hierarchy is consisted of loss of stability, diffuse failure, localized failure and finally the discrete failure. This topic is comprehensively discussed and explained by Willam and Iordache (2001), Maier et al. (1996) and Willam (2002), in this chapter a summary of these failure indicators is presented in order to have a better vision of localized failure. After this background about the failure indicators, the localization analysis for different yield functions is performed and finally the extended finite element method is described.

FAILURE INDICATORS

In this section, the loss of stability, diffuse failure or loss of uniqueness and localized failure or loss of ellipticity is discussed. The analytical localization analysis is performed and the critical angles and hardening values associated with Drucker-Prager, von Mises and Tresca criteria are presented.

3.1.1 Loss of Stability

Loss of material stability is defined with the loss of positive internal work, this internal work is defined as

$$\mathrm{d}^2W = \frac{1}{2}\dot{\boldsymbol{\epsilon}} : \mathbb{E}^{ep} : \dot{\boldsymbol{\epsilon}} \tag{3.1}$$

and the positiveness of the second order work density is the sufficient condition for the continuity of the material, that is

$$\mathrm{d}^2W = \frac{1}{2}\dot{\boldsymbol{\epsilon}} : \mathbb{E}^{ep} : \dot{\boldsymbol{\epsilon}} > 0\,, \quad \forall\dot{\boldsymbol{\epsilon}} \neq 0. \tag{3.2}$$

In the case of non-associated elastoplasticity where the normal to the yield surface is different from the normal to the plastic potential, the elastoplastic stiffness matrix is not symmetric anymore, and since the second order work density only extracts the symmetric part of the tangent operator the equation (3.2) takes the form

$$\mathrm{d}^2 W = \frac{1}{4}\dot{\boldsymbol{\epsilon}} : \left(\mathbb{E}^{ep} + \mathbb{E}^{epT}\right) : \dot{\boldsymbol{\epsilon}}, \tag{3.3}$$

and therefore the condition for loss of stability becomes

$$\mathrm{d}^2 W = 0\,, \quad \forall \dot{\boldsymbol{\epsilon}} \neq 0, \tag{3.4}$$

where it may be expressed in the form of loss of positive definiteness of the symmetric elastoplastic tensor as

$$\det\left(\frac{1}{2}\left[\mathbb{E}^{ep} + \mathbb{E}^{epT}\right]\right) = 0 \Longrightarrow \lambda_{min}\left(\frac{1}{2}\left[\mathbb{E}^{ep} + \mathbb{E}^{epT}\right]\right) = 0. \tag{3.5}$$

Based on Bromwich bounds, this eigenvalue is the lower bound of the eigenvalues of the non symmetric elastoplastic tensor,

$$\lambda_{min}(\mathbb{E}^{ep}_{sym}) \leq \Re(\lambda_i(\mathbb{E}^{ep})) \leq \lambda_{max}(\mathbb{E}^{ep}_{sym}). \tag{3.6}$$

Based on Maier and Hueckel (1979) the critical hardening value that corresponds to loss of stability is expressed as

$$H = \frac{1}{2}\left[\sqrt{(\boldsymbol{n} : \mathbb{E}^e : \boldsymbol{n})(\boldsymbol{m} : \mathbb{E}^e : \boldsymbol{m})} - \boldsymbol{n} : \mathbb{E}^e : \boldsymbol{m}\right]. \tag{3.7}$$

3.1.2 Diffuse Failure, Loss of Uniqueness

Diffuse failure maintains continuity in displacement rates and the gradient of displacement rates and is defined as a stationary state in the rate of stresses which manifest itself as a limit point in the material response curve, expressed as

$$\dot{\boldsymbol{\sigma}} = 0 \Longrightarrow \mathbb{E}^{ep} : \dot{\boldsymbol{\epsilon}} = 0. \tag{3.8}$$

Based on the equation (3.8), the condition for loss of uniqueness reduces to

$$\det\left(\mathbb{E}^{ep}\right) = 0 \Longrightarrow \lambda_{min}(\mathbb{E}^{ep}) = 0, \tag{3.9}$$

where this condition states that in case of associated plasticity the loss of uniqueness and loss of stability are identical and in the case of non associated plasticity diffuse failure is preceded by loss of stability. The elastoplastic tangent operator is expressed as

$$\begin{gathered}
\mathbb{E}^{ep} = \mathbb{E}^{e} - \frac{1}{H^p}\mathbb{E}^{e} : \boldsymbol{m} \otimes \boldsymbol{n} : \mathbb{E}^{e} \Longrightarrow \\
(\mathbb{E}^{e})^{-1} : \mathbb{E}^{ep} = \mathbb{I} - (\mathbb{E}^{e})^{-1} : \frac{1}{H^p}\mathbb{E}^{e} : \boldsymbol{m} \otimes \boldsymbol{n} : \mathbb{E}^{e},
\end{gathered} \tag{3.10}$$

and since the determinant of the elastic tensor is positive, the condition in equation (3.9) can be expressed as

$$\det\left((\mathbb{E}^{e})^{-1} : \mathbb{E}^{ep}\right) = 1 - \frac{\boldsymbol{n} : \mathbb{E}^{e} : \boldsymbol{m}}{H + \boldsymbol{n} : \mathbb{E}^{e} : \boldsymbol{m}} = 0, \tag{3.11}$$

from which the critical hardening value (H) for loss of uniqueness is achieved.

3.1.3 Loss of Ellipticity

Loss of ellipticity is defined as a jump in the gradient of displacement rate across merging surfaces while the rate of the displacements field remain continuous across the discontinuity surface, that is

$$\dot{\boldsymbol{u}}^{+} = \dot{\boldsymbol{u}}^{-} \Longrightarrow [[\dot{\boldsymbol{u}}]] = 0 \quad \text{and} \tag{3.12a}$$

$$\boldsymbol{\nabla}\dot{\boldsymbol{u}}^{+} \neq \boldsymbol{\nabla}\dot{\boldsymbol{u}}^{-} \Longrightarrow [[\boldsymbol{\nabla}\dot{\boldsymbol{u}}]] \neq 0. \tag{3.12b}$$

According to Maxwell compatibility condition, the jump in the gradient of displacement filed can be expressed as

$$[[\boldsymbol{\nabla}\dot{\boldsymbol{u}}]] = \dot{\gamma}\boldsymbol{M} \otimes \boldsymbol{N}, \tag{3.13}$$

where the scalar value $\dot{\gamma}$ expresses the magnitude of the jump across the discontinuity surface, $\boldsymbol{N}$ is the normal to this surface and $\boldsymbol{M}$ is the polarization vector which defines the direction of the jump i.e., if it is parallel to $\boldsymbol{N}$ it represents an opening mode, if it is perpendicular to $\boldsymbol{N}$ the jump is of shear nature, and other angles declare a mixed mode jump. In order to have equilibrium across the discontinuity surface, it

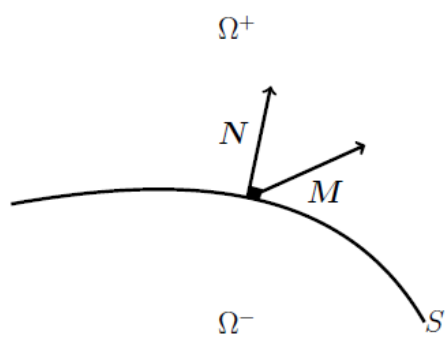

Figure 3.1: Discontinuity surface.

is required that the traction vectors on the sides should be equal and in opposite direction, i.e.,

$$[[\dot{\boldsymbol{t}}]] = \dot{\boldsymbol{t}}^+ - \dot{\boldsymbol{t}}^- = 0. \tag{3.14}$$

According to Cauchy's lemma

$$\begin{aligned} &[[\dot{\boldsymbol{t}}]] = \boldsymbol{N} \cdot [[\dot{\boldsymbol{\sigma}}]] = \boldsymbol{N} \cdot [[\mathbb{E}^{ep} : \dot{\boldsymbol{\epsilon}}]] = \boldsymbol{N} \cdot \mathbb{E}^{ep} : [[\dot{\boldsymbol{\epsilon}}]] \\ \Longrightarrow\ &[[\dot{\boldsymbol{t}}]] = \dot{\gamma}\boldsymbol{N} \cdot \mathbb{E}^{ep} \cdot \boldsymbol{N} \cdot \boldsymbol{M} = \dot{\gamma}\boldsymbol{Q}^{ep} \cdot \boldsymbol{M} = 0, \end{aligned} \tag{3.15}$$

where $\boldsymbol{Q}^{ep}$ is the elastoplastic localization tensor and is defined as

$$\boldsymbol{Q}^{ep} = \boldsymbol{N} \cdot \mathbb{E}^{ep} \cdot \boldsymbol{N}. \tag{3.16}$$

Therefore, the loss of ellipticity happens when the elastoplastic localization tensor (acoustic tensor) is singular, i.e.,

$$\det\left(\boldsymbol{Q}^{ep}\right) = 0 \Longrightarrow \lambda_{min}(\boldsymbol{Q}^{ep}) = 0. \tag{3.17}$$

Based on the equation (3.17) the loss of ellipticity occurs when the minimum eigenvalue of the acoustic tensor is equal to zero, the same argument can be carried out for the case of elastodamage or elastoplastic damage tangent operators. In the case of elastoplastic material behavior the elastoplastic localization tensor may be expressed as

$$\boldsymbol{Q}^{ep} = \boldsymbol{Q}^{e} - \frac{\boldsymbol{N} \cdot \mathbb{E}^{e} : \boldsymbol{m} \otimes \boldsymbol{n} : \mathbb{E}^{e} \cdot \boldsymbol{N}}{H^p}, \tag{3.18}$$

where it can be reformulated as

$$\boldsymbol{Q}^{ep} = \boldsymbol{Q}^{e} - \frac{\boldsymbol{e}_m \otimes \boldsymbol{e}_n}{H^p}, \tag{3.19}$$

where

$$\boldsymbol{e}_m = \boldsymbol{N} \cdot \mathbb{E}^{e} : \boldsymbol{m} \quad \text{and} \tag{3.20a}$$

$$\boldsymbol{e}_n = \boldsymbol{n} : \mathbb{E}^{e} \cdot \boldsymbol{N}. \tag{3.20b}$$

Based on Ottosen and Runesson (1991), the generalized eigenvalue problem is defined as

$$\det\left[\boldsymbol{Q}^{e-1}\cdot\boldsymbol{Q}^{ep}\right]=0, \tag{3.21}$$

where

$$\boldsymbol{Q}^{e-1}\cdot\boldsymbol{Q}^{ep}=\mathbf{1}-\boldsymbol{Q}^{e-1}\cdot\frac{\boldsymbol{e}_m\otimes\boldsymbol{e}_n}{H^p}. \tag{3.22}$$

Therefore the solution of the lowest eigenvalue of equation (3.22) becomes

$$\lambda_{min}\left(\boldsymbol{Q}^{e-1}\cdot\boldsymbol{Q}^{ep}\right)=1-\frac{\boldsymbol{e}_m\cdot\boldsymbol{Q}^{e-1}\cdot\boldsymbol{e}_n}{H+\boldsymbol{n}:\mathbb{E}^e:\boldsymbol{m}} \tag{3.23}$$

and the critical hardening modulus indicating loss of ellipticity may be expressed as

$$H=\boldsymbol{e}_n\cdot\boldsymbol{Q}^{e-1}\cdot\boldsymbol{e}_m-\boldsymbol{n}:\mathbb{E}^e:\boldsymbol{m}. \tag{3.24}$$

LOCALIZATION ANALYSIS

This section covers the analytical solution of the localization analysis of the elastoplastic models which has been discussed thoroughly by Chaves (2003). The localization analysis can be performed for the case of associated and non-associated flow rules, while the non-associated case is divided into the collinear and not collinear cases. In this work the localization analysis of the associated models ae theoretically derived and the localization analysis of the non-associated plasticity and damage models are numerically implemented into the constitutive driver which will be explained in the numerical implementation chapter.

The critical localization angle in the case of associated plasticity is on the $1-3$

plane and based on Chaves (2003) it is defined as

$$\tan^2(\theta_{cr}) = -\frac{n_3 + \nu n_2}{n_1 + \nu n_2}, \tag{3.25}$$

where n_i's are the eigenvalues of the normal to the yield surface. The critical angle is defined as the angle between the first principal axis of the normal to the yield surface, n_1, and the normal to the localization surface. In the case of non-associated flow, the

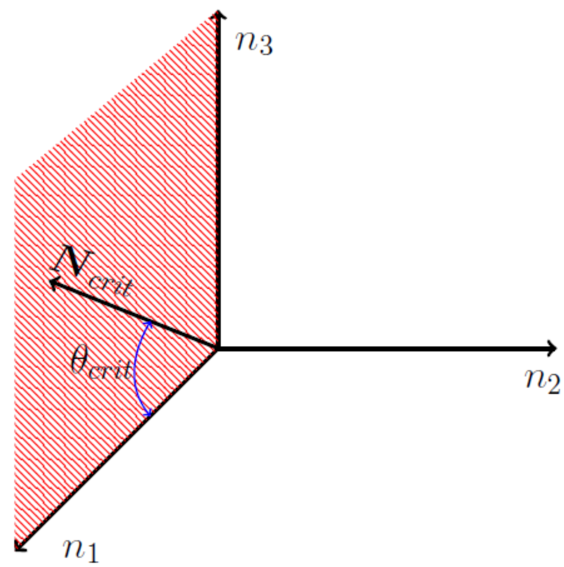

Figure 3.2: Normal to the discontinuity surface, associated flow rule.

normal to the discontinuity surface has components in all the directions. Based on figure (3.3) the components of the normal to the discontinuity surface become

$$N_1 = \cos\phi\cos\alpha, \tag{3.26a}$$

$$N_2 = \cos\phi\sin\alpha, \quad \text{and} \tag{3.26b}$$

$$N_3 = \sin\phi. \tag{3.26c}$$

It is also possible to show the normal to the discontinuity surface with regards to the direction of loading as shown in figure (3.4).

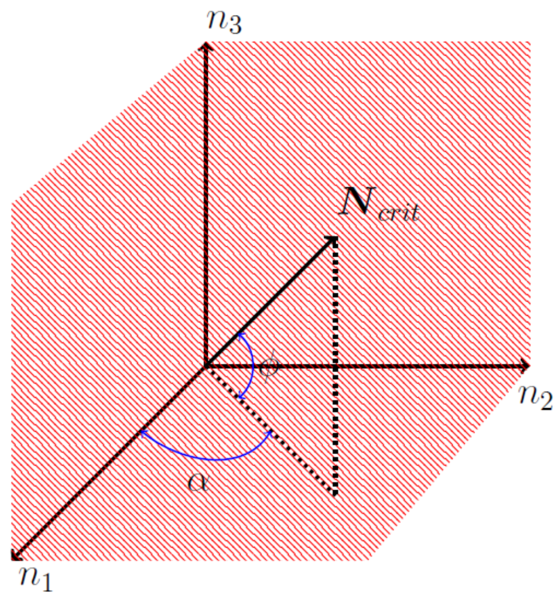

Figure 3.3: Normal to the discontinuity surface, non-associated flow rule.

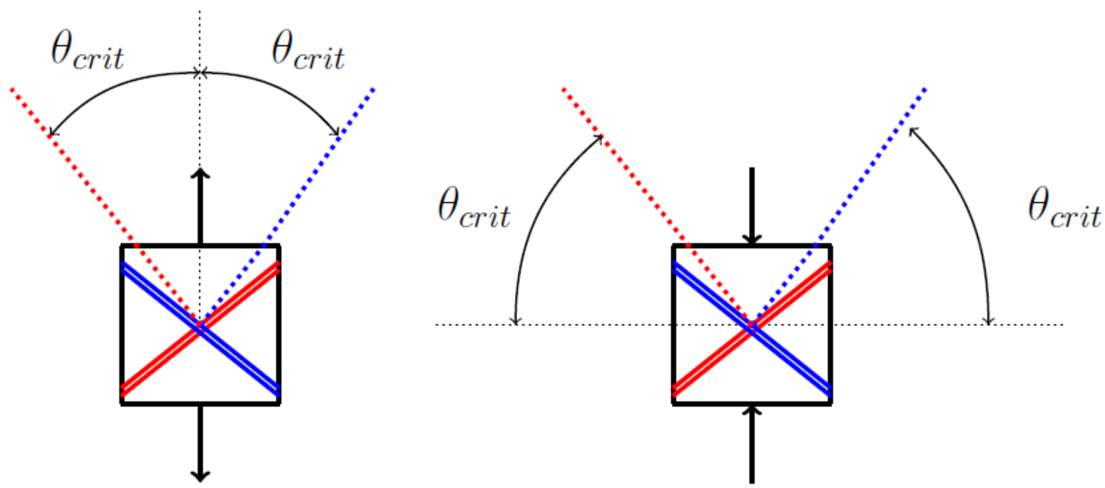

Figure 3.4: Demonstration of the critical angle in tension and compression.

3.2.1 Localization Analysis of Rankine Criterion

The Rankine's criterion is described as

$$F = \sigma_1 - \sigma_{y0} = 0, \tag{3.27}$$

therefore the normal to the yield surface becomes

$$\boldsymbol{n} = \boldsymbol{m} = \frac{\partial F}{\partial \boldsymbol{\sigma}} = \begin{pmatrix} 1 & 0 & 0 \\ 0 & 0 & 0 \\ 0 & 0 & 0 \end{pmatrix}, \tag{3.28}$$

and the critical hardening value for this criterion is zero. In short the results of localization analysis are shown in table (3.1). It is interesting to mention that this confirm

Table 3.1: Localization analysis of Rankine's criterion.

critical angle	$\tan^2(\theta_{cr}) = 0 \Longrightarrow \begin{cases} \theta_{cr1} = 0 \\ \theta_{cr2} = 0 \end{cases}$
critical hardening	$H_{cr} = 0$

the modes of failure associated with the Rankine's criterion, that is the material fails perpendicular to the direction of the principal stress.

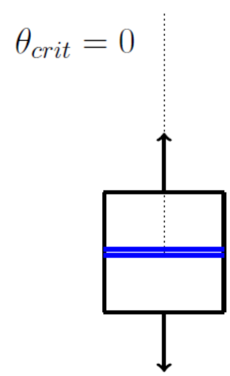

Figure 3.5: Critical angle and failure surface based on Rankine's criterion.

3.2.2 Localization Analysis of von Mises Criterion

The von Mises criterion is describes as

$$F = \sqrt{3J_2} - \sigma_y(K) = 0. \tag{3.29}$$

The normal to the yield surface is defined as

$$\boldsymbol{n} = \frac{\partial F}{\partial \boldsymbol{\sigma}} = \frac{\sqrt{3}\boldsymbol{s}}{2\sqrt{J_2}}, \tag{3.30}$$

where $\boldsymbol{s}$ is described in terms of the principal stresses as

$$\boldsymbol{s} = \begin{pmatrix} \frac{2\sigma_1-\sigma_2-\sigma_3}{3} & 0 & 0 \\ 0 & \frac{2\sigma_2-\sigma_1-\sigma_3}{3} & 0 \\ 0 & 0 & \frac{2\sigma_3-\sigma_1-\sigma_2}{3} \end{pmatrix}. \tag{3.31}$$

Therefore the second invariant of the deviatoric stress tensor becomes

$$J_2 = \frac{1}{2}\sqrt{\sigma_1^2 + \sigma_2^2 + \sigma_3^2} \tag{3.32}$$

and finally based on equation (3.25) the critical angle and hardening values are presented in table (3.2). This provides different critical angles and hardening modulus

Table 3.2: Localization analysis of von Mises criterion.

critical angle	$\tan^2(\theta_{cr}) = -\frac{S_3+\nu S_2}{S_1+\nu S_2}$
critical hardening	$H_{cr} = -\frac{3ES_2^2}{2(S_1^2+S_2^2+S_3^2)}$

based on different loading scenarios which will be thoroughly discussed in the following chapters.

3.2.3 Localization Analysis of Tresca Criterion

The Tresca criterion is defined as

$$F = |\frac{\sigma_1 - \sigma_3}{2}| - \tau_{max} = 0, \tag{3.33}$$

therefore the normal to the yield function becomes

$$\boldsymbol{n} = \boldsymbol{m} = \frac{\partial F}{\partial \boldsymbol{\sigma}} = \begin{pmatrix} \frac{1}{2} & 0 & 0 \\ 0 & 0 & 0 \\ 0 & 0 & -\frac{1}{2} \end{pmatrix}. \tag{3.34}$$

This results in the critical angle and hardening modulus presented in table (3.3). As

Table 3.3: Localization analysis of Tresca criterion.

critical angle	$\tan^2(\theta_{cr}) = 1 \Longrightarrow \begin{cases} \theta_{cr1} = +45^o \\ \theta_{cr2} = -45^0 \end{cases}$
critical hardening	$H_{cr} = 0$

expected, critical angles associated with Tresca criterion are 45 degrees with respect to the principal direction which is in agreement with the pure shear failure mode of ductile materials.

3.2.4 Localization Analysis of Drucker-Prager Criterion

The yield function and plastic potential used to model Drucker-Prager plasticity are

$$F = \alpha I_1 + \sqrt{J_2} - K = 0 \quad \text{and} \tag{3.35a}$$

$$G = \beta I_1 + \sqrt{J_2}, \tag{3.35b}$$

therefore for the case of non-associated flow the normal to the yield and potential functions become

$$\boldsymbol{n} = \alpha \mathbf{1} + \frac{\boldsymbol{s}}{2\sqrt{J_2}} \quad \text{and} \tag{3.36a}$$

$$\boldsymbol{m} = \beta \mathbf{1} + \frac{\boldsymbol{s}}{2\sqrt{J_2}}. \tag{3.36b}$$

Based on Chaves (2003) the critical angle for the non-associated plasticity with collinearity between $\boldsymbol{n}$ and $\boldsymbol{m}$ is expressed as

$$\tan^2\theta_{13} = \frac{[(m_3 - m_1)n_2 + (n_3 - n_1)m_2]\nu + (2n_3 - n_1)m_3 - m_1 n_3}{[(m_1 - m_3)n_2 + (n_1 - n_3)m_2]\nu + (2n_1 - n_3)m_1 - n_1 m_3}. \tag{3.37}$$

The corresponding values of the critical hardening and critical angle are presented in table (3.4), where where

Table 3.4: Localization analysis of non-associated Drucker-Prager criterion.

critical angle	$\tan^2(\theta_{cr}) = \frac{-(1+\nu)(\beta+\alpha)-2(S_3+\nu S_2)}{(1+\nu)(\beta+\alpha)+2(S_1+\nu S_2)}$
critical hardening	$H_{cr} = -\frac{E}{(1-\nu^2)}[A_1 + A_2 + A_3]$

$$A_1 = \frac{[(1-2\nu)S_3 + (1+\nu)\beta][(1-2\nu)S_3 + (1+\nu)\alpha]}{(1-2\nu)}, \tag{3.38a}$$

$$A_2 = \frac{[2(\nu S_2 + S_1) + (1+\nu)(\beta+\alpha)]^2}{4}, \tag{3.38b}$$

$$A_3 = -3(1-\nu)\frac{(1-2\nu)\tau_{oct}^2 + (1+\nu)(\alpha\beta)}{(1-2\nu)}, \tag{3.38c}$$

and τ_{oct} is given by

$$\tau_{oct}^2 = \frac{1}{9}[(\sigma_1 - \sigma_2)^2 + (\sigma_2 - \sigma_3)^2 + (\sigma_3 - \sigma_1)^2]. \tag{3.39}$$

In the case of associated flow rule it is sufficient to substitute β with α.

EXTENDED FINITE ELEMENT METHOD

Extended finite element method is explained and introduced in this section. This method is a particular form of the partition of unity method (PUM) and it has been chosen because of its capability to model crack initiation and propagation without remeshing, because of the availability of the subroutines to modify and enhance the crack propagation and its orientation and because it does not need to conform with internal boundaries. The articles of Belytschko and Black (1999), Moës et al.

(1999), Moës et al. (2000) and Giner et al. (1999) and the manual of Abaqus software(ABAQUS (2012)) from Dassault company are utilized to explain and introduce this model. The governing equations for a cracked body in space are expressed as follow

$$\sigma_{ji,j} + b_i = 0 \quad \text{in} \quad \Omega, \tag{3.40a}$$

$$\sigma_{ij} n_j = t_i \quad \text{on} \quad \Gamma_t, \tag{3.40b}$$

$$\sigma_{ij} n_j = 0 \quad \text{on} \quad \Gamma_{S^+}, \quad \text{and} \tag{3.40c}$$

$$\sigma_{ij} n_j = 0 \quad \text{on} \quad \Gamma_{S^-}, \tag{3.40d}$$

where the boundary condition is

$$\boldsymbol{u} = \bar{\boldsymbol{u}} \quad \text{on} \quad \Gamma_u \tag{3.41}$$

and the domain and its boundaries are depicted in figure (3.6).

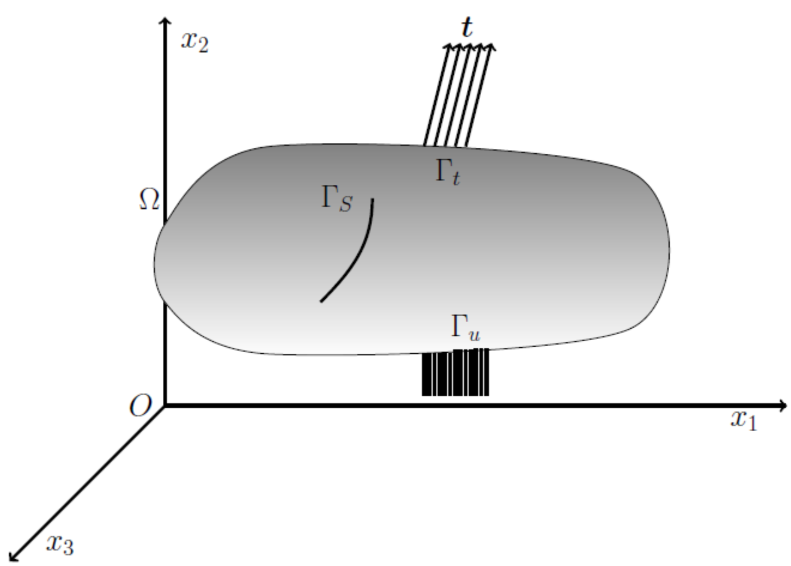

Figure 3.6: The domain and its boundaries.

The weak format of equilibrium equation is defined as

$$\int_\Omega \boldsymbol{\sigma} : \boldsymbol{\epsilon}(\boldsymbol{v}) \mathrm{d}\Omega = \int_\Omega \boldsymbol{b} \cdot \boldsymbol{v} \mathrm{d}\Omega + \int_{\Gamma_t} \bar{\boldsymbol{t}} \cdot \boldsymbol{v} \mathrm{d}\Gamma \quad \forall \boldsymbol{v} \in \mathbb{U}_0, \tag{3.42}$$

where the test function space $\mathbb{U}_0$ is defined as

$$\mathbb{U}_0 = \{\boldsymbol{v} \in \mathbb{V} : \boldsymbol{v} = 0 \quad \text{on} \quad \Gamma_u \boldsymbol{,} \quad \boldsymbol{v} \quad \text{discontinuouson} \quad \Gamma_S\}. \tag{3.43}$$

The space $\mathbb{V}$ is the space related to the trial function. It is observed that the strong and weak formulation is very similar to the continuous formulation, however the difference manifest itself in the discretization of the problem, where the crack is modeled using discontinuous enrichment of the elements. In the most general case of XFEM, the displacement approximation is described as

$$\boldsymbol{u}_{xfem}(\boldsymbol{x}) = \sum_{i\in\Phi} N_i(\boldsymbol{x})\boldsymbol{u}_i + \sum_{i\in\Phi_H} N_i(\boldsymbol{x})H(\boldsymbol{x})\boldsymbol{a}_i + \sum_{i\in\Phi_C} \left[N_i(\boldsymbol{x}) \sum_{\alpha=1}^{4} F_\alpha(\boldsymbol{x})\boldsymbol{b}_{i\alpha}\right], \tag{3.44}$$

where Φ is the set of all nodes in the domain, Φ_H is the set of nodes containing the crack and Φ_C is the set of nodes containing the crack tip. H is the heaviside function, F_α are the crack-tip functions, $\boldsymbol{a}_i$ and $\boldsymbol{b}_{i\alpha}$ are the degrees of freedom of enriched nodes and $\boldsymbol{u}_i$ are physical nodal displacements of non-enriched nodes. As it is observed from figure (3.7) the crack does not have to follow the element edges and it could pass through the elements. For simplicity it is assumed that all the elements are fully cracked, i.e., there is no need to consider crack-tip enrichment functions, therefore the complexity of the problem is reduced while the accuracy of the model is preserved. From equation (3.45) it is concluded that the physical displacement at an enriched node does not correspond to the true displacement, therefore the shifted

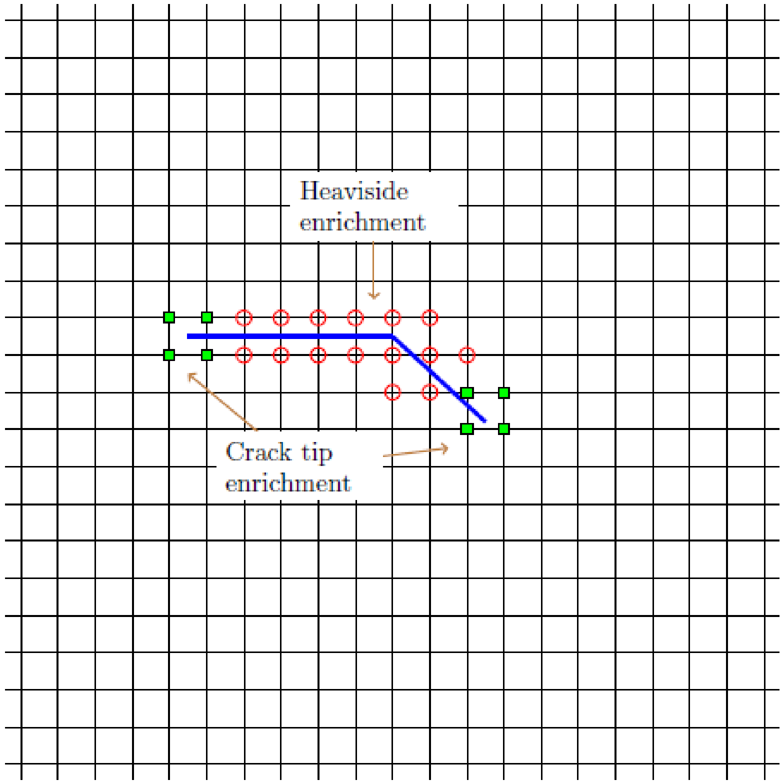

Figure 3.7: Heaviside and crack-tip enrichment.

basis formulation is introduced as a modification to the formulation, expressed as

$$\boldsymbol{u}_{xfem}(\boldsymbol{x}) = \sum_{i \in \Phi} N_i(\boldsymbol{x})\boldsymbol{u}_i + \sum_{i \in \Phi_H} N_i(\boldsymbol{x}) \left[H(\boldsymbol{x}) - H(\boldsymbol{x}_i)\right] \boldsymbol{a}_i. \tag{3.45}$$

In this report it is assumed that the material remains continuous until a certain fracture initiation criterion is met and then crack grows in the direction that has the critical localization properties. The XFEM capability of Abaqus software is used while the initiation and propagation of the crack is controlled by a user subroutine called UDMGINI which will be discussed in the following chapters. Abaqus software has a few capabilities of extended finite element method modeling from which the cohesive segment method with phantom nodes is chosen. This method assumes a traction-separation cohesive behavior for the element and could be used for both brittle and ductile material behaviors. Phantom nodes are superposed on the original

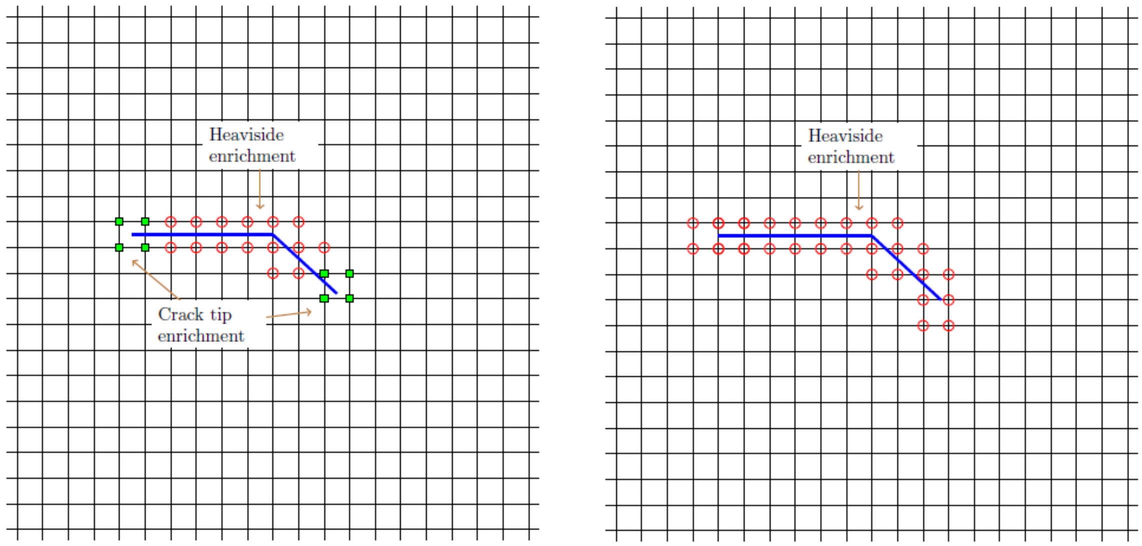

Figure 3.8: Modification of the enrichment by removing crack-tip enrichments.

nodes and are constrained to the original nodes when the element is continuous, however when the element is cracked the element splits into two parts where each part contains a combination of real and phantom nodes. The element is assumed

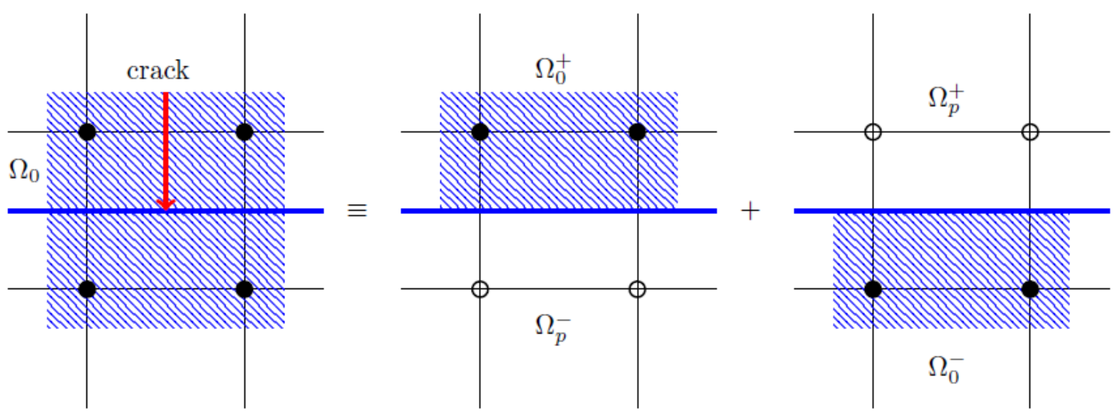

Figure 3.9: Phantom nodes.

to be totally cracked when the cohesive strength of the element becomes zero and the phantom nodes and real nodes move independently. In order to have a set of full interpolation basis, the part of the real domain of the cracked element, Ω_0, is extended to the phantom domain, Ω_p, and therefore the displacement in the real domain, Ω_0, can be interpolated by the nodes of the phantom and real domain. The jump in the displacement field is calculated by only integrating the real part of each domain i.e., Ω_0^+ and Ω_0^-. The traction-separation behavior used in this work is a linear uncoupled behavior expressed as

$$\boldsymbol{t} = \begin{pmatrix} t_n \\ t_s \\ t_t \end{pmatrix} = \begin{pmatrix} K_{nn} & 0 & 0 \\ 0 & K_{ss} & 0 \\ 0 & 0 & K_{tt} \end{pmatrix} \begin{pmatrix} \delta_n \\ \delta_s \\ \delta_t \end{pmatrix} = \boldsymbol{K\delta}, \tag{3.46}$$

where the units of K_{ii} is pressure divided by displacement. The implementation of

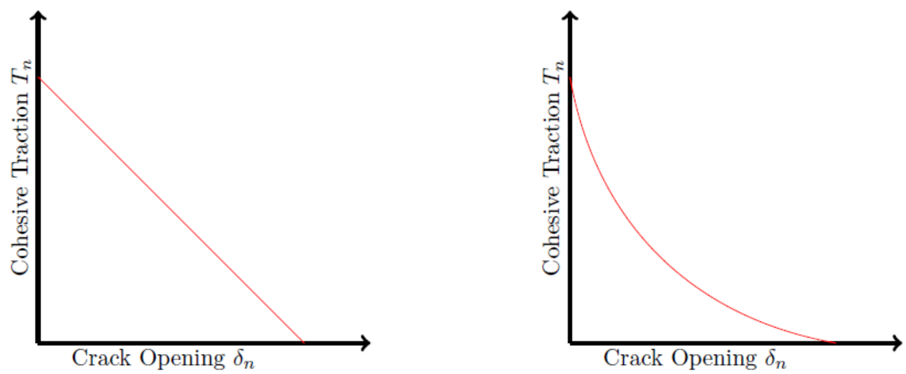

Figure 3.10: Traction-separation behavior, linear and nonlinear.

the user subroutine requires the introduction of a failure criteria and a normal vector defining the direction of cracking. The failure criteria used in this work are the strain format of J_2 plasticity, Tresca and St. Venant in the form of nominal formulation which produces a value between zero to one. The crack propagation occurs when this criteria is equal to one. The direction of the crack is predicted by the localization analysis of the failure criteria as an example in the case of cast iron the Rankine criterions is used and the localization analysis predicts that the crack propagates perpendicular to the direction of the maximum principal stress. The details of the implementation of these models is described in the following chapters.

Chapter 4. Numerical Implementation

In this chapter the numerical implementation of the previously discussed plastic and damage-plasticity models are discussed, and the the numerical localization analysis of these models is described. These problems are static problems and they are solved using a nonlinear displacement control scheme. At each displacement step, for each element and Gauss point the strains are calculated and a constitutive driver is called to calculate the updated values of stresses, plastic strains, damage variables and internal parameters. Afterwards the elastoplastic, elastodamage or elastoplastic tangent operator is calculated and the global stiffness matrix and force vectors are assembled for all the elements and finally the error associated with the displacement guess is calculated, if it is less than the tolerance, it proceeds to next step, otherwise the Newthon-Raphson method is used to update the displacement values. This procedure is repeated until the convergence is achieved. For the constitutive driver, a fully implicit backward Euler method along with the Newthon-Raphson method are utilized to solve for the unknowns which is explained later in this chapter. It should be noted that the proposed models are coded in Matlab software [Matlab (2011)] and Fortran and then they are implemented inside a user subroutine UMAT to be able to connect it to Abaqus software [ABAQUS (2012)]. For detailed information about numerical modeling please refer to Simo and Hughes (1998).

BACKWARD EULER FOR PLASTICITY MODELS

The input values for a plastic constitutive driver are the old stress ${}^{n}\boldsymbol{\sigma}$, the old plastic strain ${}^{n}\boldsymbol{\epsilon}^{p}$, the old strain ${}^{n}\boldsymbol{\epsilon}$, the old internal variables ${}^{n}\underline{\kappa}$ and the strain increment $\Delta\boldsymbol{\epsilon}$. Inside the constitutive driver the trial values are calculated as

$$\boldsymbol{\sigma}^{tr} = {}^{n}\boldsymbol{\sigma} + \mathbb{E}^{e} : \boldsymbol{\Delta}\epsilon, \tag{4.1}$$

$$ {}^{n+1}\boldsymbol{\epsilon} = {}^{n}\boldsymbol{\epsilon} + \boldsymbol{\Delta}\epsilon, \quad \text{and} \tag{4.2} $$

$$ \underline{K}^{tr} = {}^{n}\underline{K}. \tag{4.3} $$

Based on the trial values of stresses and hardening variables, it is now possible to calculate the trial yield function by defining the trial value of the stress invariants

$$ {I_1}^{tr} = \mathbf{1} : \boldsymbol{\sigma}^{tr}, \tag{4.4a} $$

$$ {J_2}^{tr} = \frac{1}{2}\mathbf{1} : \left(\boldsymbol{\sigma}^{tr} - \frac{1}{3}I_1^{tr}\right)^2, \tag{4.4b} $$

$$ {J_2}^{tr} = \frac{1}{3}\mathbf{1} : \left(\boldsymbol{\sigma}^{tr} - \frac{1}{3}I_1^{tr}\right)^3, \tag{4.4c} $$

and therefore

$$ F^{p,tr} = F^{p}(I_1^{tr}, J_2^{tr}, J_3^{tr}, \underline{K}^{tr}), \tag{4.5} $$

where the underline is used because the number of the hardening variables may be different. If the trial yield function is greater than or equal to zero, it means that the trial values that are calculated are passing the yield envelope and they need to be returned to the yield surface with a return mapping, otherwise, the material is still in the elastic range and the trial values are correct, i.e.,

$$ \text{if} \quad F^{p,tr} < 0 \quad \Longrightarrow $$

$$ {}^{n+1}\boldsymbol{\sigma} = \boldsymbol{\sigma}^{tr}, \tag{4.6a} $$

$$ {}^{n+1}\boldsymbol{\epsilon}^{p} = {}^{n}\boldsymbol{\epsilon}^{p}, \tag{4.6b} $$

$$ {}^{n+1}\underline{K} = {}^{n}\underline{K}, \tag{4.6c} $$

$$ {}^{n+1}\Delta\lambda = {}^{n}\Delta\lambda, \quad \text{and} \tag{4.6d} $$

$$\mathbb{E}^{ep} = \mathbb{E}^{e}. \tag{4.6e}$$

In the case of plastic loading, the backward Euler is applied and the incremental problem becomes

$$\dot{\boldsymbol{\sigma}} = \mathbb{E}^{e} : (\dot{\boldsymbol{\epsilon}} - \dot{\boldsymbol{\epsilon}}^{p}) \Longrightarrow \Delta\boldsymbol{\sigma} = \mathbb{E}^{e} : (\Delta\boldsymbol{\epsilon} - \Delta\boldsymbol{\epsilon}^{p}), \tag{4.7}$$

where the incremental plastic strain is

$$\Delta\boldsymbol{\epsilon}^{p} = \Delta t\dot{\lambda}\boldsymbol{m} \Longrightarrow \Delta\boldsymbol{\epsilon}^{p} = \Delta\lambda\boldsymbol{m}. \tag{4.8}$$

Therefore the updated stress becomes

$$^{n+1}\boldsymbol{\sigma} = \underbrace{^{n}\boldsymbol{\sigma} + \mathbb{E}^{e} : \Delta\boldsymbol{\epsilon}}_{\boldsymbol{\sigma}^{tr}} - \Delta\lambda\mathbb{E}^{e} : \boldsymbol{m}. \tag{4.9}$$

Based on the backward Euler method the hardening variable takes the form

$$\dot{\underline{K}} = \frac{\partial\underline{K}}{\partial\underline{\kappa}} \cdot \dot{\underline{\kappa}} \Longrightarrow {}^{n+1}\underline{K} = {}^{n}\underline{K} - \Delta\lambda\frac{\partial\underline{K}}{\partial\underline{\kappa}} \cdot \frac{\partial G^{p}}{\partial\underline{K}}, \tag{4.10}$$

where in the case of single hardening variable it could take the form

$$^{n+1}K = {}^{n}K + \Delta\lambda H, \tag{4.11}$$

where the hardening is defined as

$$H = -\frac{\partial K}{\partial\kappa} \cdot \frac{\partial G^{p}}{\partial K}. \tag{4.12}$$

Now in order to solve for the values of stress, hardening and plastic multiplier that satisfy the conditions in equation (4.13), the Newthon-Raphson method is used and expressed as

$$\dot{\lambda} \geq 0\,, \quad F^p \leq 0\,, \quad \dot{\lambda} F^p = 0. \tag{4.13}$$

In order to use the Newton-Raphson method, the residual functions should be defined as

$$\boldsymbol{R}_{\boldsymbol{\sigma}} = \boldsymbol{\sigma} - \boldsymbol{\sigma}^{tr} + \Delta\lambda \mathbb{E}^e : \boldsymbol{m} = 0, \tag{4.14a}$$

$$R_K = K - {}^nK - \Delta\lambda H = 0, \tag{4.14b}$$

$$R_{\Delta\lambda} = F^p(\boldsymbol{\sigma}, K, \Delta\lambda) = 0, \tag{4.14c}$$

and the vector of unknowns $\underline{X}$ and the residual vector $\underline{R}$ are defined as

$$\underline{X}^T = \begin{pmatrix} \boldsymbol{\sigma} & K & \Delta\lambda \end{pmatrix} \quad \text{and} \tag{4.15a}$$

$$\underline{R}^T = \begin{pmatrix} \boldsymbol{R}_{\boldsymbol{\sigma}} & R_K & R_{\Delta\lambda} \end{pmatrix}. \tag{4.15b}$$

Now that the unknown vectors and residuals are specified, the Newthon-Raphson iteration is acquired to solve for the unknowns as follows:

1. Given the $\underline{X}^{(k)}$ in iteration k, compute $\underline{J}^{(k)} = \frac{\partial \underline{R}}{\partial \underline{X}}$ where $\underline{J}$ is the Jacobian matrix

2. Calculate the unknowns of step $(k+1)$

$\underline{X}^{(k+1)} = \underline{X}^{(k)} + \delta\underline{X}$ where $\delta\underline{X} = -\left[\underline{J}^{(k)}\right]^{-1} \underline{R}^{(k)}$

3. Update the residuals based on the calculated improved solution, $\underline{R}^{(k+1)} = \underline{R}(\underline{X}^{(k+1)})$

4. Check the convergence, if $|\underline{R}^{(k+1)}| <$ TOL, stop, else goto step 1 and continue the iteration.

The jacobian matrix can be explicitly expressed as

$$\underline{J} = \begin{pmatrix} \frac{\partial R_{\boldsymbol{\sigma}}}{\partial \boldsymbol{\sigma}} & \frac{\partial R_{\boldsymbol{\sigma}}}{\partial K} & \frac{\partial R_{\boldsymbol{\sigma}}}{\partial \Delta\lambda} \\ \frac{\partial R_{K}}{\partial \boldsymbol{\sigma}} & \frac{\partial R_{K}}{\partial K} & \frac{\partial R_{K}}{\partial \Delta\lambda} \\ \frac{\partial R_{\Delta\lambda}}{\partial \boldsymbol{\sigma}} & \frac{\partial R_{\Delta\lambda}}{\partial K} & \frac{\partial R_{\Delta\lambda}}{\partial \Delta\lambda} \end{pmatrix}. \tag{4.16}$$

Finally when the return mapping process is finished, the elastoplastic tangent operator is calculated, the global equilibrium is checked and if the tolerance is achieved it proceeds to the next step, otherwise, the updated values of the displacement will enter the constitutive driver in terms of $\Delta\boldsymbol{\epsilon}$ and the process is repeated.

BACKWARD EULER FOR DAMAGE MODEL

In this section the constitutive driver for the case of pure damage is discussed. The damage model that is used here is discussed earlier in the theory chapter, the damage function is expressed as

$$F^d(Y_v, D) = Y_v - r(D), \tag{4.17}$$

where the volumetric strain energy is given by

$$Y_v = \frac{1}{2}K^0\langle\epsilon_v^e\rangle^2 + c\int_0^{\epsilon_v^p} |\sigma_m|\langle \mathrm{d}\epsilon_v^p\rangle \tag{4.18}$$

and for the case of pure damage it is reduced to

$$Y_v = \frac{1}{2}K^0\langle\epsilon_v^e\rangle^2. \tag{4.19}$$

The resistance function is expressed as

$$r(D) = r_0(1-D)^{p-1}. \tag{4.20}$$

The rate of the volumetric strain energy is expressed as

$$\dot{Y}_v = K^0 \langle \epsilon_v^e \rangle \mathbf{1} : \dot{\boldsymbol{\epsilon}}. \tag{4.21}$$

The trial value of the volumetric strain energy is calculated based on the equation (4.19) as

$$Y_v^{tr} = \frac{1}{2} K^0 \epsilon_v^{e,tr} \qquad \text{if} \quad \epsilon_v^{e,tr} > 0, \tag{4.22a}$$

$$Y_v^{tr} = 0 \leq 0, \tag{4.22b}$$

and the trial value of the resistance function is defined as

$$r^{tr} = r_0 (1 - {}^{n}D)^{p-1}. \tag{4.23}$$

The trial damage function is calculated as

$$F^{d,tr} = Y_v^{tr} - r^{tr}. \tag{4.24}$$

In the case that $F^{d,tr}$ is greater than or equal to zero, a constitutive driver is used to calculate the new value of the damage variable D, otherwise the material behavior is elastic and the updated values are as follows:

$$^{n+1}\boldsymbol{\sigma} = \boldsymbol{\sigma}^{tr}, \tag{4.25a}$$

$$^{n+1}D = {}^{n}D, \quad \text{and} \tag{4.25b}$$

$$\mathbb{E}^d = (1 - {}^{n}D)\mathbb{E}^e. \tag{4.25c}$$

If $F^{d,tr} > 0$ then the trial values are an overestimate of the actual values and they need to be corrected. The damage variable needs to be modified to satisfy the residual equation,

$$R_D = F^d = Y_v - r = 0 \tag{4.26}$$

and therefore the updated value for D is defined as

$${}^{n+1}D = {}^{n}D - [J]^{-1}\, {}^{n}R_D. \tag{4.27}$$

The jacobian is defined as

$$J = \frac{\partial R_D}{\partial D} = r_0(p-1)(1 - {}^{n}D)^{p-2} \tag{4.28}$$

and the updated value of D becomes

$${}^{n+1}D = {}^{n}D - \frac{1}{r_0(p-1)(1 - {}^{n}D)^{p-2}}\, {}^{n}R_D. \tag{4.29}$$

The new damage variable, ${}^{n+1}D$, is substituted into the residual function and if the tolerance is achieved, it is used to update the stress and elastodamage tangent operator, otherwise the process is repeated, finally the updated stress tensor and tangent operator are given by

$${}^{n+1}\boldsymbol{\sigma} = \boldsymbol{\sigma}^{tr}\frac{1 - {}^{n+1}D}{1 - {}^{n}D} \quad \text{and} \tag{4.30}$$

$$\mathbb{E}^d = (1 - {}^{n+1}D)\mathbb{E}^e. \tag{4.31}$$

BACKWARD EULER FOR DAMAGE PLASTICITY MODELS

The constitutive model of damage-plasticity model is very similar to the plasticity case except that the damage function is also present. This section is divided into two parts, one for the Drucker-Prager model and the other for Willam-Warnke model. In these models the trial values for damage and plasticity functions are calculated and if both are greater than or equal to zero then the coupled plastodamage constitutive driver is called.

4.3.1 Constitutive Driver for Drucker-Prager and Damage Model

If both the damage and plastic functions are negative the material is still in the elastic region and the variables are expressed as follow:

$$\text{if} \qquad F^{p,tr} < 0 \quad \text{and} \quad F^{d,tr} < 0$$

$$^{n+1}\boldsymbol{\sigma} = \boldsymbol{\sigma}^{tr}, \tag{4.32a}$$

$$^{n+1}\boldsymbol{\epsilon}^p = {}^{n}\boldsymbol{\epsilon}^p, \tag{4.32b}$$

$$^{n+1}\bar{e}^p = {}^{n}\bar{e}^p, \tag{4.32c}$$

$$^{n+1}\Delta\lambda = {}^{n}\Delta\lambda, \tag{4.32d}$$

$$^{n+1}D = {}^{n}D, \tag{4.32e}$$

$$^{n+1}Y_v = Y_v^{tr}, \quad \text{and} \tag{4.32f}$$

$$\mathbb{E}^{epd} = (1 - {}^{n}D)\mathbb{E}^e. \tag{4.32g}$$

In the case that both the damage and plastic functions are positive, the residuals are given by

$$\text{if} \qquad F^{p,tr} \geq 0 \quad \text{and} \quad F^{d,tr} \geq 0$$

$$\boldsymbol{R}_{\boldsymbol{\sigma}} = \boldsymbol{\sigma} - \boldsymbol{\sigma}^{tr} + \Delta\lambda(1 - {}^{n}D + \Delta D)\mathbb{E}^e : \boldsymbol{m} + \Delta D\mathbb{E}^e : (\boldsymbol{\epsilon}^e + \Delta\boldsymbol{\epsilon}) = 0, \tag{4.33a}$$

$$R_{\bar{e}^p} = \bar{e}^p - {}^{n}\bar{e}^p - \frac{\Delta\lambda}{\sqrt{3}} = 0, \tag{4.33b}$$

$$R_{\Delta\lambda} = \alpha I_1 + \sqrt{J_2} - (1 - {}^{n}D + \Delta D)K = 0, \quad \text{and} \tag{4.33c}$$

$$R_D = Y_v - r_0(1 - {}^{n}D + \Delta D)^{p-1}. \tag{4.33d}$$

The residual and variable vectors become

$$\underline{X}^T = \begin{pmatrix} \boldsymbol{\sigma} & \bar{e}^p & \Delta\lambda & D \end{pmatrix} \quad \text{and} \tag{4.34a}$$

$$\underline{R}^T = \begin{pmatrix} \boldsymbol{R_\sigma} & R_{\bar{e}^p} & R_{\Delta\lambda} & R_D \end{pmatrix}. \tag{4.34b}$$

Now that the unknown vectors and residuals are specified, the Newthon-Raphson iteration is acquired to solve for the unknowns as follows:

1. Given the $\underline{X}^{(k)}$ in iteration k, compute $\underline{J}^{(k)} = \frac{\partial \underline{R}}{\partial \underline{X}}$ where $\underline{J}$ is the Jacobian matrix
2. Calculate the unknowns of step $(k+1)$
$\underline{X}^{(k+1)} = \underline{X}^{(k)} + \delta\underline{X}$ where $\delta\underline{X} = -\left[\underline{J}^{(k)}\right]^{-1} \underline{R}^{(k)}$
3. Update the residuals based on the calculated improved solution, $\underline{R}^{(k+1)} = \underline{R}(\underline{X}^{(k+1)})$
4. Check the convergence, if $|\underline{R}^{(k+1)}| < \text{TOL}$, stop, else goto step 1 and continue the iteration.

Finally when the return mapping process is finished, the elastoplastic damage tangent operator is calculated based on equation (2.115).

4.3.2 Constitutive Driver for Willam-Warnke and Damage Model

If both the damage and plastic functions are negative the material is still in the elastic region and the variables are expressed as follow:

$$\text{if} \qquad F^{p,tr} < 0 \quad \text{and} \quad F^{d,tr} < 0$$

$$^{n+1}\boldsymbol{\sigma} = \boldsymbol{\sigma}^{tr}, \tag{4.35a}$$

$$^{n+1}\boldsymbol{\epsilon}^p = {}^{n}\boldsymbol{\epsilon}^p, \tag{4.35b}$$

$$^{n+1}\epsilon_v^p = {}^{n}\epsilon_v^p, \tag{4.35c}$$

$$^{n+1}\Delta\lambda = {}^{n}\Delta\lambda, \tag{4.35d}$$

$$^{n+1}D = {}^{n}D, \tag{4.35e}$$

$$^{n+1}Y_v = Y_v^{tr}, \quad \text{and} \tag{4.35f}$$

$$\mathbb{E}^{epd} = (1 - {}^{n}D)\mathbb{E}^{e}. \tag{4.35g}$$

In the case that both the damage and plastic functions are positive, the residuals are defined as

$$\text{if} \qquad F^{p,tr} \geq 0 \quad \text{and} \quad F^{d,tr} \geq 0$$

$$\boldsymbol{R_\sigma} = \boldsymbol{\sigma} - \boldsymbol{\sigma}^{tr} + \Delta\lambda(1 - {}^{n}D + \Delta D)\mathbb{E}^{e} : \boldsymbol{m} + \Delta D\mathbb{E}^{e} : (\boldsymbol{\epsilon}^{e} + \Delta\boldsymbol{\epsilon}) = 0, \tag{4.36a}$$

$$R_{\epsilon_v^p} = \epsilon_v^p - {}^{n}\epsilon_v^p - 3\Delta\lambda\beta = 0, \tag{4.36b}$$

$$R_{\Delta\lambda} = \left(\sqrt{1.5}\frac{\rho}{K(\epsilon_v^p)f_c}\right)^2 + \\ (1 - {}^{n}D + \Delta D)m\left(\frac{\rho}{\sqrt{6}K(\epsilon_v^p)f_c}r(\theta, e) + \frac{\xi}{\sqrt{3}K(\epsilon_v^p)f_c}\right) - (1 - {}^{n}D + \Delta D)^2 c(\epsilon_v^p) = 0, \tag{4.36c}$$

$$R_D = Y_v - r_0(1 - {}^{n}D + \Delta D)^{p-1}, \tag{4.36d}$$

and therefore the residual and variable vectors become

$$\underline{X}^T = \begin{pmatrix} \boldsymbol{\sigma} & \epsilon_v^p & \Delta\lambda & D \end{pmatrix} \quad \text{and} \tag{4.37a}$$

$$\underline{R}^T = \begin{pmatrix} \boldsymbol{R_\sigma} & R_{\epsilon_v^p} & R_{\Delta\lambda} & R_D \end{pmatrix}. \tag{4.37b}$$

Now that the unknown vectors and residuals are specified, the Newthon-Raphson iteration is acquired to solve for the unknowns as follows:

1. Given the $\underline{X}^{(k)}$ in iteration k, compute $\underline{J}^{(k)} = \frac{\partial \underline{R}}{\partial \underline{X}}$ where $\underline{J}$ is the Jacobian matrix

2. Calculate the unknowns of step $(k+1)$
$\underline{X}^{(k+1)} = \underline{X}^{(k)} + \delta\underline{X}$ where $\delta\underline{X} = -\left[\underline{J}^{(k)}\right]^{-1}\underline{R}^{(k)}$

3. Update the residuals based on the calculated improved solution, $\underline{R}^{(k+1)} = \underline{R}(\underline{X}^{(k+1)})$

4. Check the convergence, if $|\underline{R}^{(k+1)}| < \text{TOL}$, stop, else goto step 1 and continue the iteration.

Finally when the return mapping process is finished, the elastoplastic damage tangent operator is calculated based on equation (2.133).

NUMERICAL IMPLEMENTATION OF LOCALIZATION ANALYSIS

The numerical localization analysis is performed for the damage, plasticity and damage plasticity models introduced in the earlier chapters. The elastic, elastodamage, elastoplasticity and elastoplastic damage localization second order tensors are calculated respectively as

$$\boldsymbol{Q}^{e} = N_i E^{e}_{ijkl} N_k, \tag{4.38a}$$

$$\boldsymbol{Q}^{ed} = N_i E^{ed}_{ijkl} N_k, \tag{4.38b}$$

$$\boldsymbol{Q}^{ep} = N_i E^{ep}_{ijkl} N_k, \quad \text{and} \tag{4.38c}$$

$$\boldsymbol{Q}^{epd} = N_i E^{epd}_{ijkl} N_k. \tag{4.38d}$$

Inside the constitutive driver, after the stresses and strains are updated and the tangent operator is calculated, a function is called to numerically calculate the localization tensors. This is performed by understanding that in the $3D$ case the components of the normal to the localization surface are defined as

$$N_1 = \cos\phi \cos\alpha, \tag{4.39a}$$

$$N_2 = \cos\phi \sin\alpha, \quad \text{and} \tag{4.39b}$$

$$N_3 = \sin\phi. \tag{4.39c}$$

In the case of associated flow and $2D$ modeling they are defined as

$$N_1 = \cos\theta, \tag{4.40a}$$

$$N_2 = 0, \quad \text{and} \tag{4.40b}$$

$$N_3 = \sin\theta, \tag{4.40c}$$

where θ is the in-plane angle in the $1-3$ plane. Based on the above equations, in the general three dimensional case, two loops over ϕ and α are available and in every step the value of the components of the localization tensor are calculated as follows:

$$\begin{aligned}
Q^*_{11} &= N_1E^*_{1111}N_1 + N_1E^*_{1121}N_2 + N_1E^*_{1131}N_3 + N_2E^*_{2111}N_1 + N_2E^*_{2121}N_2 \\
&\quad + N_2E^*_{2131}N_3 + N_3E^*_{3111}N_1 + N_3E^*_{3121}N_2 + N_3E^*_{3131}N_3, \\
Q^*_{12} &= N_1E^*_{1112}N_1 + N_1E^*_{1122}N_2 + N_1E^*_{1132}N_3 + N_2E^*_{2112}N_1 + N_2E^*_{2122}N_2 \\
&\quad + N_2E^*_{2132}N_3 + N_3E^*_{3112}N_1 + N_3E^*_{3122}N_2 + N_3E^*_{3132}N_3, \\
Q^*_{13} &= N_1E^*_{1113}N_1 + N_1E^*_{1123}N_2 + N_1E^*_{1133}N_3 + N_2E^*_{2113}N_1 + N_2E^*_{2123}N_2 \\
&\quad + N_2E^*_{2133}N_3 + N_3E^*_{3113}N_1 + N_3E^*_{3123}N_2 + N_3E^*_{3133}N_3, \\
Q^*_{21} &= N_1E^*_{1211}N_1 + N_1E^*_{1221}N_2 + N_1E^*_{1231}N_3 + N_2E^*_{2211}N_1 + N_2E^*_{2221}N_2 \\
&\quad + N_2E^*_{2231}N_3 + N_3E^*_{3211}N_1 + N_3E^*_{3221}N_2 + N_3E^*_{3231}N_3, \\
Q^*_{22} &= N_1E^*_{1212}N_1 + N_1E^*_{1222}N_2 + N_1E^*_{1232}N_3 + N_2E^*_{2212}N_1 + N_2E^*_{2222}N_2 \\
&\quad + N_2E^*_{2232}N_3 + N_3E^*_{3212}N_1 + N_3E^*_{3222}N_2 + N_3E^*_{3232}N_3, \\
Q^*_{23} &= N_1E^*_{1213}N_1 + N_1E^*_{1223}N_2 + N_1E^*_{1233}N_3 + N_2E^*_{2213}N_1 + N_2E^*_{2223}N_2 \\
&\quad + N_2E^*_{2233}N_3 + N_3E^*_{3213}N_1 + N_3E^*_{3223}N_2 + N_3E^*_{3233}N_3, \\
Q^*_{31} &= N_1E^*_{1311}N_1 + N_1E^*_{1321}N_2 + N_1E^*_{1331}N_3 + N_2E^*_{2311}N_1 + N_2E^*_{2321}N_2 \\
&\quad + N_2E^*_{2331}N_3 + N_3E^*_{3311}N_1 + N_3E^*_{3321}N_2 + N_3E^*_{3331}N_3, \\
Q^*_{32} &= N_1E^*_{1312}N_1 + N_1E^*_{1322}N_2 + N_1E^*_{1332}N_3 + N_2E^*_{2312}N_1 + N_2E^*_{2322}N_2 \\
&\quad + N_2E^*_{2332}N_3 + N_3E^*_{3312}N_1 + N_3E^*_{3322}N_2 + N_3E^*_{3332}N_3, \quad \text{and} \\
Q^*_{33} &= N_1E^*_{1313}N_1 + N_1E^*_{1323}N_2 + N_1E^*_{1333}N_3 + N_2E^*_{2313}N_1 + N_2E^*_{2323}N_2 \\
&\quad + N_2E^*_{2333}N_3 + N_3E^*_{3313}N_1 + N_3E^*_{3323}N_2 + N_3E^*_{3333}N_3,
\end{aligned} \tag{4.41}$$

where $*$ may be replaced by e, ed, ep and epd in order to calculate elastic, elasto-damage, elastoplastic and elastoplastic damage localization tensors. When the localization tensor is calculated for each step, the normalized value of the determinant of the localization tensor for that step is calculated as

$$\mathbb{Q} = \frac{\det[Q^*]}{\det[Q^e]} \tag{4.42}$$

and is saved to a file with the corresponding angles for that value. Then these data are imported into the Matlab software and the localization surfaces are plotted, see figure (4.1) as an example. In the case of associated plasticity or $2D$ models, the loop

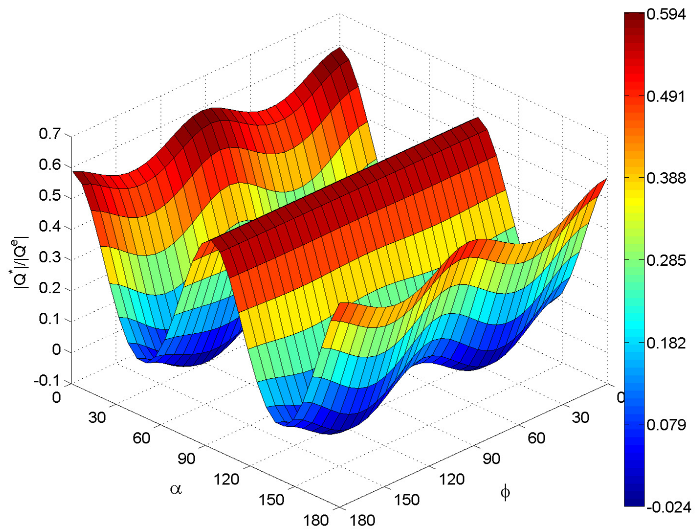

Figure 4.1: 3D numerical localization analysis.

is only designed for angle θ and the corresponding components of the localization tensor become

$$Q^*_{11} = N_1 E^*_{1111} N_1 + N_1 E^*_{1131} N_3 + N_3 E^*_{3111} N_1 + N_3 E^*_{3131} N_3,$$

$$Q^*_{12} = N_1 E^*_{1112} N_1 + N_1 E^*_{1132} N_3 + N_3 E^*_{3112} N_1 + N_3 E^*_{3132} N_3,$$

$$Q^*_{13} = N_1 E^*_{1113} N_1 + N_1 E^*_{1133} N_3 + N_3 E^*_{3113} N_1 + N_3 E^*_{3133} N_3,$$

$$
\begin{aligned}
Q^*_{21} &= N_1 E^*_{1211} N_1 + N_1 E^*_{1231} N_3 + N_3 E^*_{3211} N_1 + N_3 E^*_{3231} N_3, \\
Q^*_{22} &= N_1 E^*_{1212} N_1 + N_1 E^*_{1232} N_3 + N_3 E^*_{3212} N_1 + N_3 E^*_{3232} N_3, \\
Q^*_{23} &= N_1 E^*_{1213} N_1 + N_1 E^*_{1233} N_3 + N_3 E^*_{3213} N_1 + N_3 E^*_{3233} N_3, \\
Q^*_{31} &= N_1 E^*_{1311} N_1 + N_1 E^*_{1331} N_3 + N_3 E^*_{3311} N_1 + N_3 E^*_{3331} N_3, \\
Q^*_{32} &= N_1 E^*_{1312} N_1 + N_1 E^*_{1332} N_3 + N_3 E^*_{3312} N_1 + N_3 E^*_{3332} N_3, \quad \text{and} \\
Q^*_{33} &= N_1 E^*_{1313} N_1 + N_1 E^*_{1333} N_3 + N_3 E^*_{3313} N_1 + N_3 E^*_{3333} N_3.
\end{aligned} \tag{4.43}
$$

The three dimensional graphical representation of the localization analysis is depicted in figure (4.2).

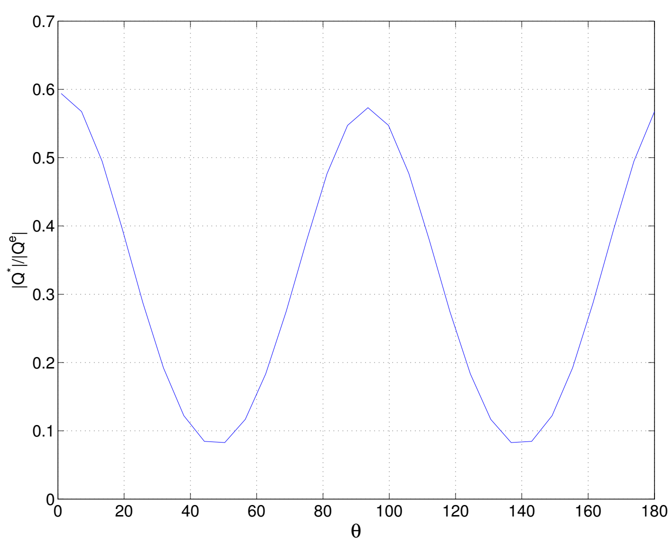

Figure 4.2: 2D and associated numerical localization analysis.

Chapter 5. Experimental Observation

This chapter includes the experimental observations on metallic and cementitious specimens, which is carried out at the University of Houston with a Tinius Olsen testing frame under displacement control. The first section contains the experiments performed on mild steel, cast iron, high strength steel and aluminum. The experiments are monitored with a non-contact photogammetric digital image correlation system, the displacement and strain fields are extracted and the failure mechanisms associated with each material type is observed and discussed. The corresponding load-deformation curves are obtained and the accuracy of DIC system is compared with the results obtained by LVDT.

The second section of this chapter contains the experimental observations on cylindrical concrete specimens, the strain and displacement field data are captured by DIC system and the corresponding load-deformation curves for the uniaxial and cyclic loading scenarios are extracted.

The last section of this chapter is the error analysis of the DIC data. Raw displacement data that are captured using a DIC system are extracted from the Aramis software and are imported into Matlab, then a finite element mesh is generated that covers all the data and using the least square method the best nodal displacement values are obtained, these values are compared with the DIC data and the error associated with this approximation is measured for different element types. Afterwards, infinitesimal and finite strain theories are used to calculate the strain field on the specimen and it is compared with the results obtained from Aramis software.

EXPERIMENTAL OBSERVATION ON METALLIC SPECIMENS

Several perforated and unperforated flat bar specimens made of mild steel, high strength steel, cast iron and aluminum are prepared based on ASTM standard and tested under uniaxial tension. There are a couple of flat bars for each material type and a pair of flat bars for each of the perforated bars. A Tinius Olsen and a

Shore Western testing machine are used for the purpose of axial experiments and a photogrammetric non-contact device is acquired in order to provide additional data in the form of displacement and strain field on the surface of the specimens. The observations of this Digital Image Correlation (DIC) system is compared with the LVDT measurements in order to study the accuracy of the device. The ultimate load capacity and strength of each material is obtained and the effect of perforation on the ductility, strength and load capacity of that material is assessed and compared. Modes of failure and fracture based on the material behavior are explained and the transition of brittle-ductile failure is studied. The load-deformation curves of this experiments are presented and the effect of perforation on the ultimate load capacity and strength of the material is studied.

5.1.1 Experiments

Flat bars that are tested are made of mild steel, high strength steel, cast iron and aluminum, the chemical composition of the alloys are presented in table (5.1).

Table 5.1: Chemical composition of the tested flat bars.

	C	Mn	P	S	Si	Ni	Mo	Cr	Cu
Cast iron	3.09	.76	.022	.19	2.69	.04	<.01	.08	.07
Mild Steel	.16	.41	.01	.004	.045	.07	.01	.08	.24
High Strength	.21	.66	.009	.012	.20	.07	.01	.13	.16

	Al	V	Ti	Nb	Co	B	W	Zr	Sn
Cast iron	.01	<.01	<.01	<.01	.008	<.0005	<.01	<.01	.06
Mild Steel	.023	<.002	<.002	<.002	.007	<.005	<.01	<.01	.009
High Strength	.006	<.002	<.002	<.002	0.007	<.005	<.01	<.01	.006

	Si	Fe	Cu	Mn	Mg	Cr	Zn	Ti	Other
Al 6061	.4-.8	<.7	.15-.4	<.15	.8-1.2	.04-.35	<.25	<.15	.15

These flat bars are made based on ASTM standard, there are two of each flat bar without perforation and there are a pair for each diameter of the perforated flat bar. The geometry of the flat bars is depicted in figure (5.1a). In this figure, Φ is the diameter of the perforations and it varies from a $^1/_{16}$ to $^1/_4$ of an inch. These flat bars are tested in uniaxial tension using displacement control and the rate of the displacement controlled test is kept the same for all test samples in order to eliminate possible strain rate effects. The test is performed on a Tinius Olsen and a Shore Western test frame and the data is recorded using LVDT and Digital Image Correlation (DIC) system. The test setup is depicted in figure (5.1b). The flat bars are placed inside the grips and the photogrammetric non contact digital image correlation system is mounted in front of the specimen according to the instructions of the GOM optical measuring techniques company. The specimens are painted in white and then black speckles of black paint is sprayed on the specimen. The speckle pattern of a painted cast iron specimen is depicted in figure (5.2). Two cameras are placed in front of the specimen in order to have a 3D measurement field, these cameras observe the deformation of the specimen through the images captured at time intervals by various rectangular image details known as facets. These facets are quadrilaterals that include a portion of the specimen in form of pixels and cover n by n pixels of the specimen that are equally distanced from one another. The 2D coordinates of the facets are calculated based on the corners points of the quadrilaterla and center of the facet is calculated by averaging the four corners. Using the information from left and right cameras, the 3D coordinates of the facet points are calculated.

5.1.2 Failure Mechanism

Having all the specimen carefully painted, the tension test is performed on the specimens and the failed specimens are shown in figure (5.4). Metals failure and fracture can be described by three mechanisms that are ductile fracture, cleavage and inter-granular fractue from which the first two are the most common mechanisms.

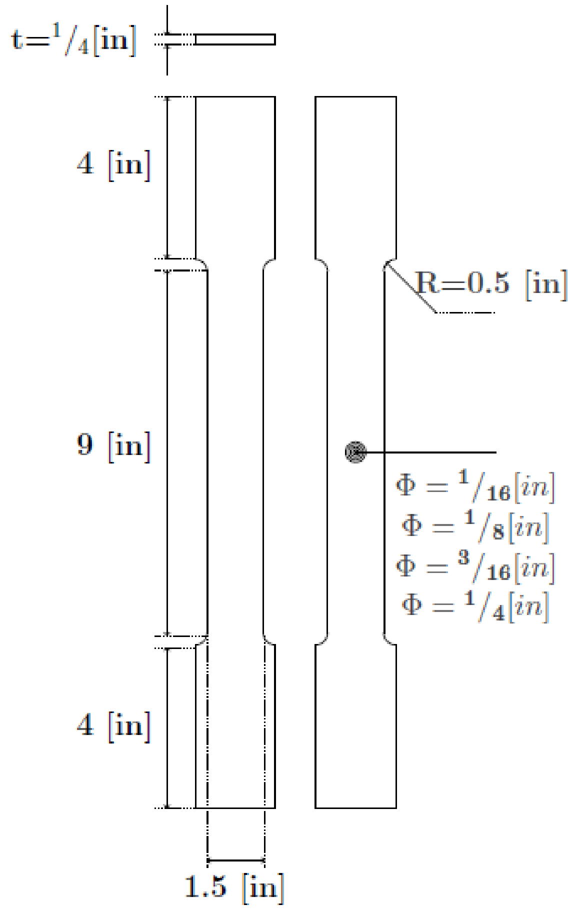

(a) Dimension of the flat bars

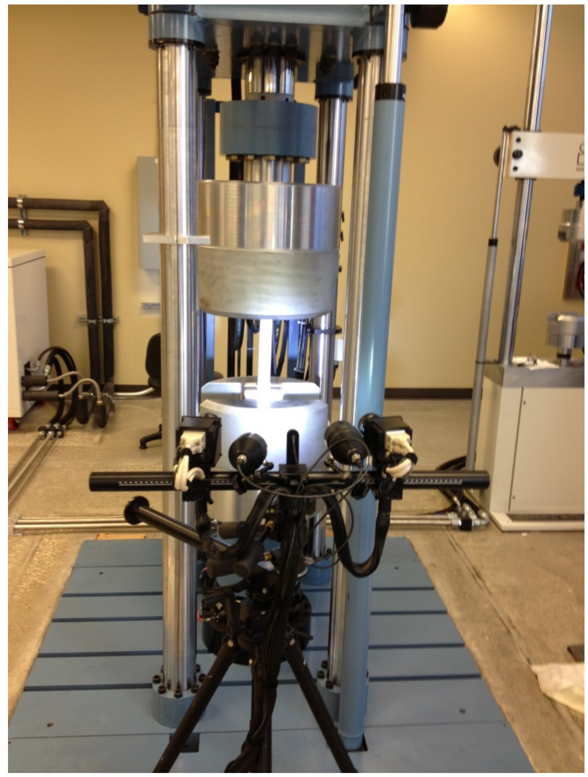

(b) Test setup

Figure 5.1: Dimension of the flat bars and test setup.

Figure 5.2: Speckle pattern on the painted specimen.

Ductile fracture is consisted of three stages, formation of a free surface at an inclusion or second phase material, void growth because of hydrostatic stress and the coalescence of voids. Void nucleation and coalescence are the main cause of failure at the center of the specimen because of the presence of triaxial state of stress and higher density of voids, however because of the lower density of the voids and the shear dominant state of stress close to the edges the material exhibits a shear dominant failure close to the free edges. This explains the failure of mild steel specimen, while in the case of the Aluminum, the failure is a shear dominant failure with an inclined out of plane failure plane. In the case of high strength steel the failure is also a mixed mode of void coalescence and shear failure. It should be noted that since the thickness of the specimens are relatively small in compare to the width of them, the out of plane failure mechanism is a shear failure. In the case of perforated specimens, the cracks tend to grow in the direction of the maximum equivalent strain while the global geometry constraints force the cracks to remain perpendicular to the direction of loading, the presence of these constraints form a zig-zag pattern as described by Anderson (1995) that results in a cleavage failure mechanism of the core material.

Cleavage failure mechanism is the rapid propagation of a crack in a transgranular pattern. This is the most common failure mechanism for brittle metals, however it should be noted that it can be preceded by ductile and plastic behavior. The plane of failure is perpendicular to the direction of loading and for brittle behavior the failure can be explained by the principal of maximum stress. This failure mechanism perfectly describes the failure of the cast iron specimens. Cleavage failure of cast iron flat bars and shear failure of mild steel and high strength steel flat bars are depicted in figure (5.3).

(a) Mild steel

(b) High strength steel

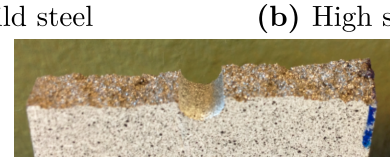

(c) Cast iron

Figure 5.3: Through-the-thickness failure of flat bars.

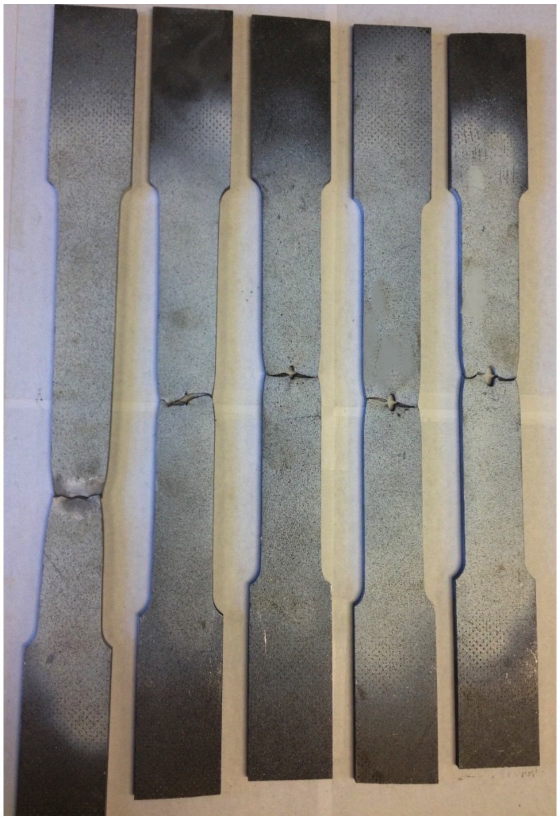

(a) Mild steel

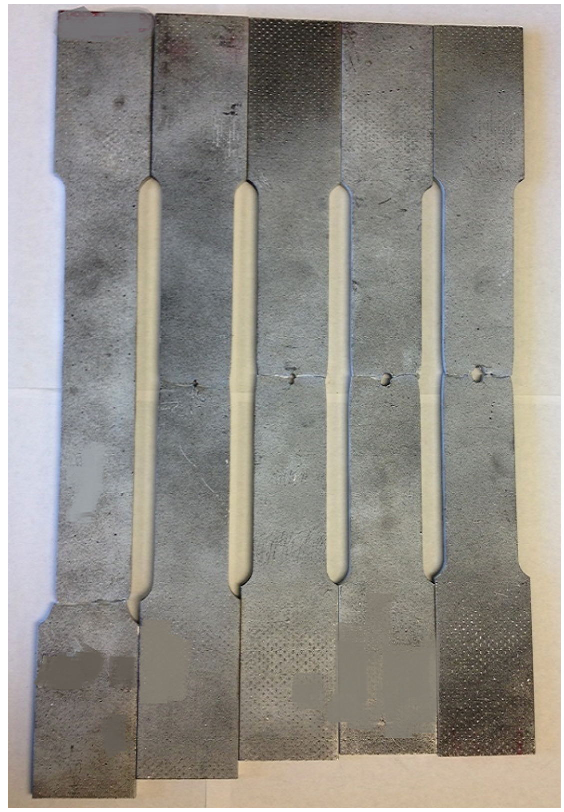

(b) Aluminum

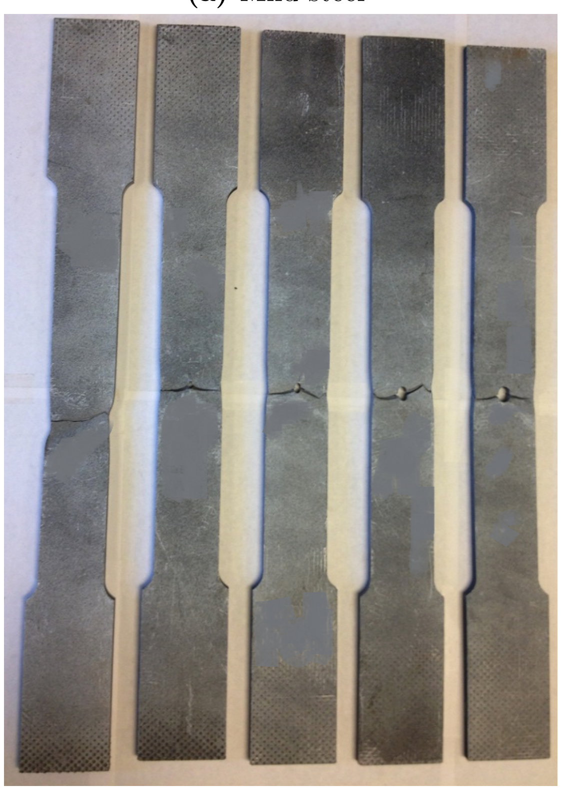

(c) High strength steel

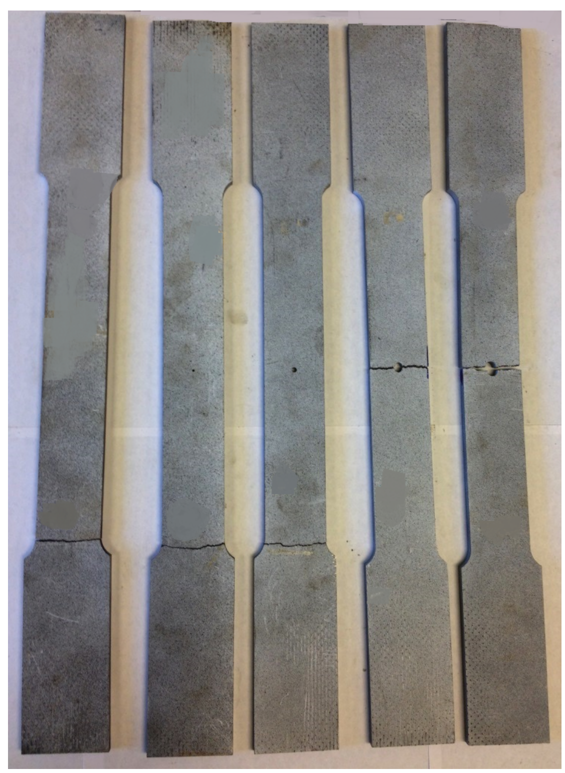

(d) Cast iron

Figure 5.4: Failed flat bars under uniaxial tension test.

5.1.3 Experimental Observations

The load-deformation response curve of the tested flat bars of mild steel, aluminum, high strength steel and cast iron are presented in figures (5.5), (5.6), (5.7) and (5.8) respectively.

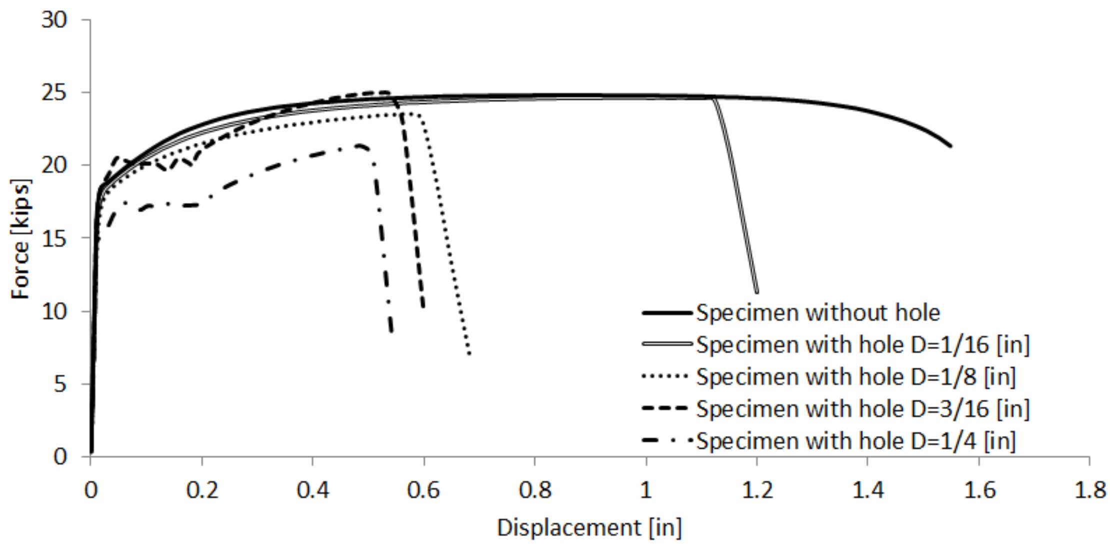

Figure 5.5: Load-deformation curve of mild steel flat bars.

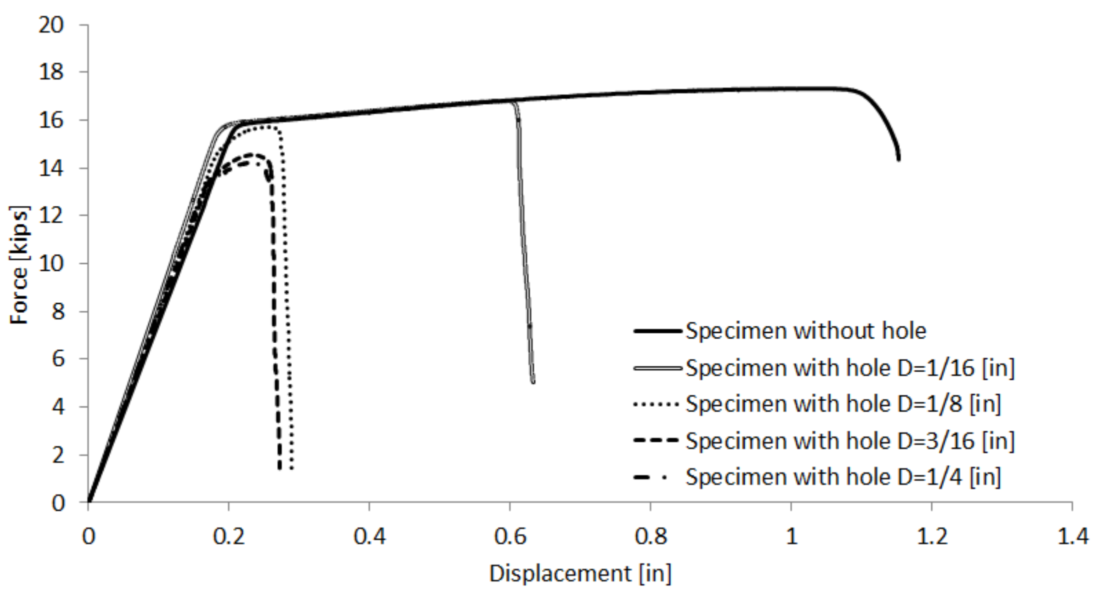

Figure 5.6: Load-deformation curve of aluminum flat bars.

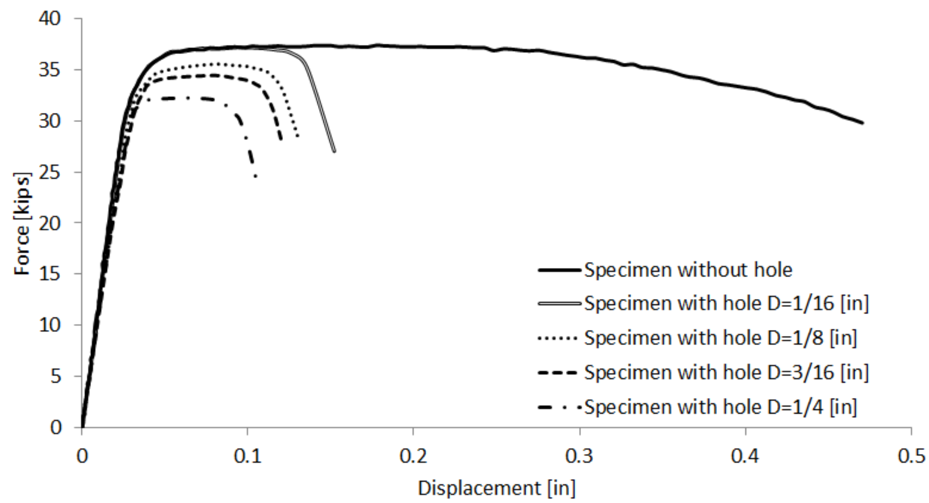

Figure 5.7: Load-deformation curve of high strength steel flat bars.

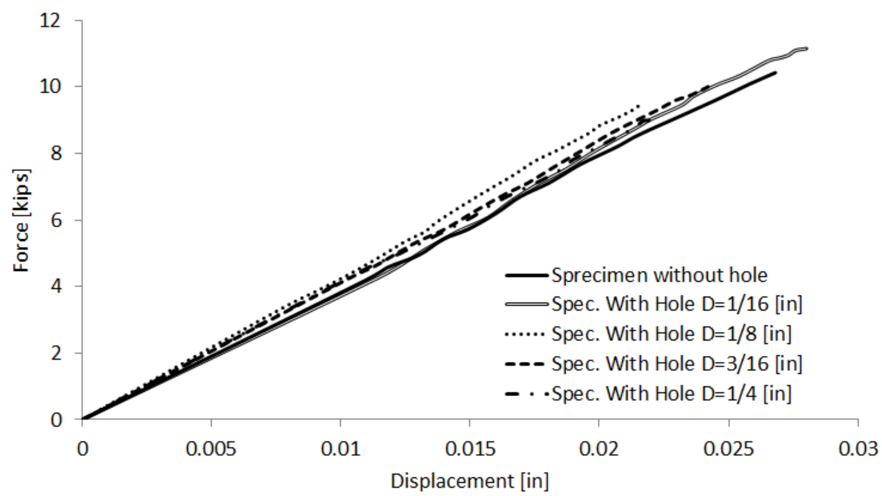

Figure 5.8: Load-deformation curve of cast iron flat bars.

Having the load-deformation curves, it is possible to obtain the stress-strain curves of the flat bars and consequently plot the change in the ultimate load capacity and ultimate strength of these specimen with respect to the circular perforation diameter. In order to have a comparison between different materials, the nominal strength or load capacity of the notched specimens are normalized by the ultimate strength or load capacity of the unnotched specimen. As a result of circular perforation, it is expected the ultimate load capacity of the perforated specimens decrease

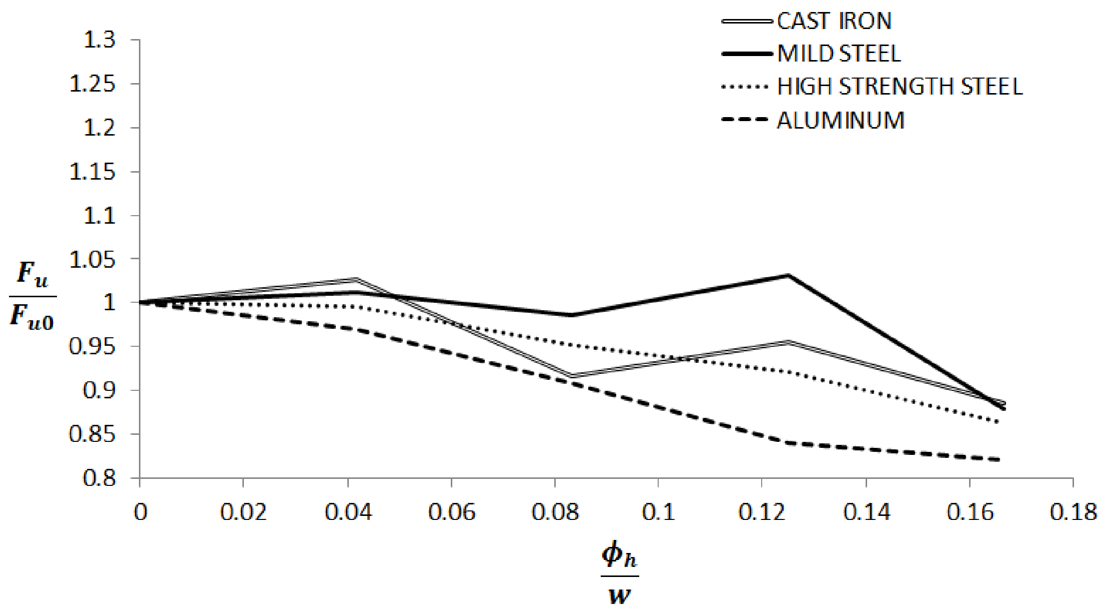

Figure 5.9: Ultimate load ratio of the perforated specimen.

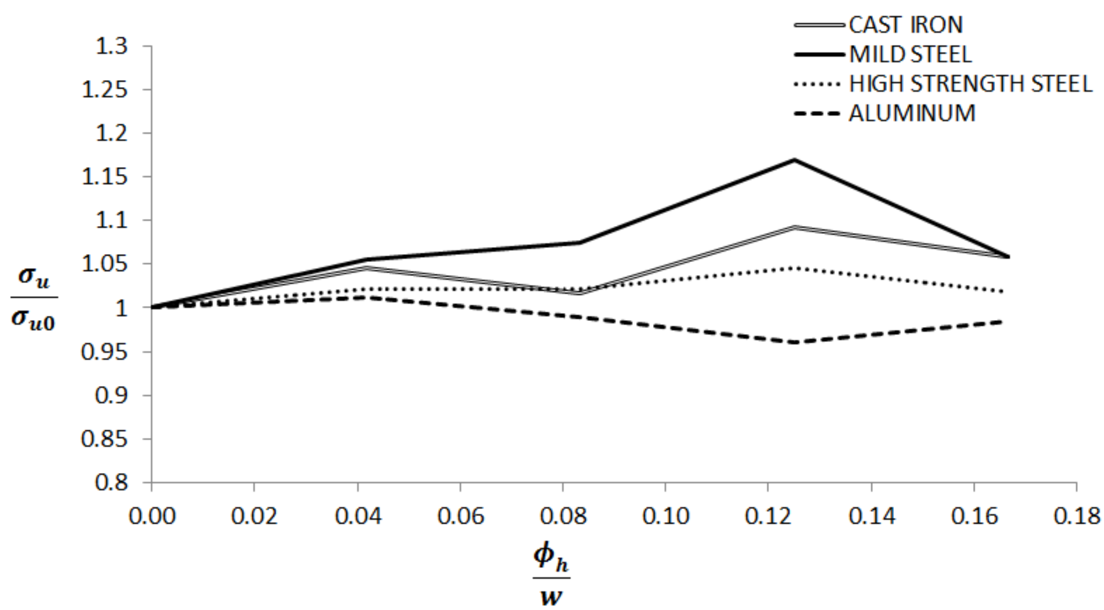

Figure 5.10: Ultimate stress ratio of the perforated specimen.

to a third of the unperforated specimens, but from the figures (5.9) and (5.10) it is observed that the reduction is about 15 percent. It is also concluded that although the ultimate load capacity of the specimens decrease by increasing the hole size, the ultimate tensile strength of those specimens does not change drastically.

5.1.4 Digital Image Correlation

Digital Image Correlation system is used in order to capture the displacement and strain field distribution over the entire region of interest. In order to justify the readings of Digital Image Correlation (DIC) system, a series of test experiments are performed on flat bars made of cast iron. The LVDT is mounted on the Specimen as

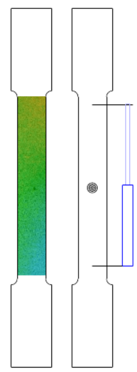

Figure 5.11: Schematic of LVDT and ARAMIS data.

shown in figure (5.11) in order to collect the displacement data during the test. Having the DIC system configured and calibrated, the test is started using displacement control and both the DIC system and the LVDT start to collect the data simultaneously. After the test is over, the displacements are measured in the vicinity of the area that the LVDT is mounted using the post processing toolbox in Aramis software and are compared to that of the LVDT, the results are shown in figure (5.12). Test one, refers to the sample without perforation and the rest are for the samples with different hole sizes, where test two is for the smallest hole size, and test five for the largest. Based on the experiment data the root mean square deviation is calculated and presented in table (5.2).

Table 5.2: Root mean square deviation of ARAMIS and LVDT.

Test	1	2	3	4	5
Error [in]	0.00050502	0.000484562	0.000575622	0.000242378	0.000397895

From the root mean square deviation calculation it is observed that the difference between the LVDT and DIC measurements is negligible.

The results of strain and displacement distribution on the mild steel, cast iron and aluminum specimens are depicted in figures (5.13), (5.14), (5.15) and (5.16). The

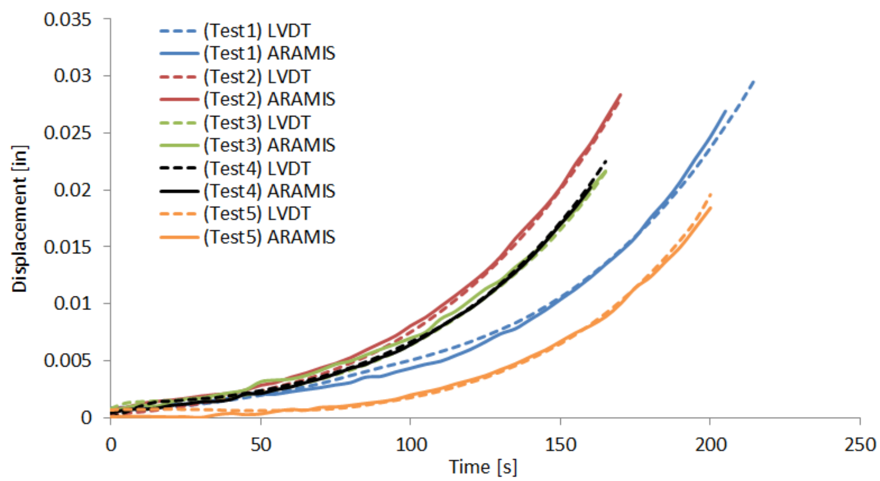

Figure 5.12: Comparison of LVDT and ARAMIS data.

longitudinal strain distribution field on the mild steel specimen with varying diameter is depicted in figure (5.13), these images are showing the formation of shear bands prior to failure that are also present for the case of high strength steel and aluminum specimens.

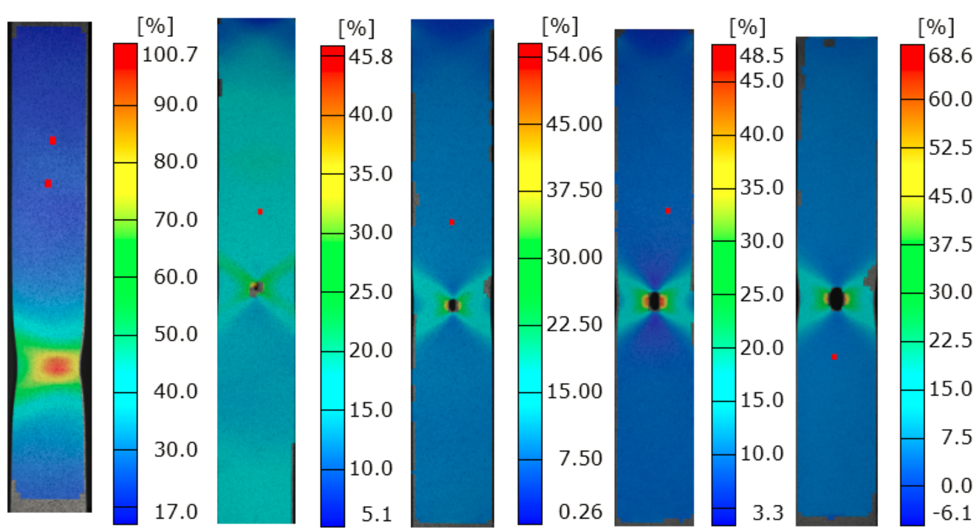

Figure 5.13: Longitudinal strain field on the mild steel specimen.

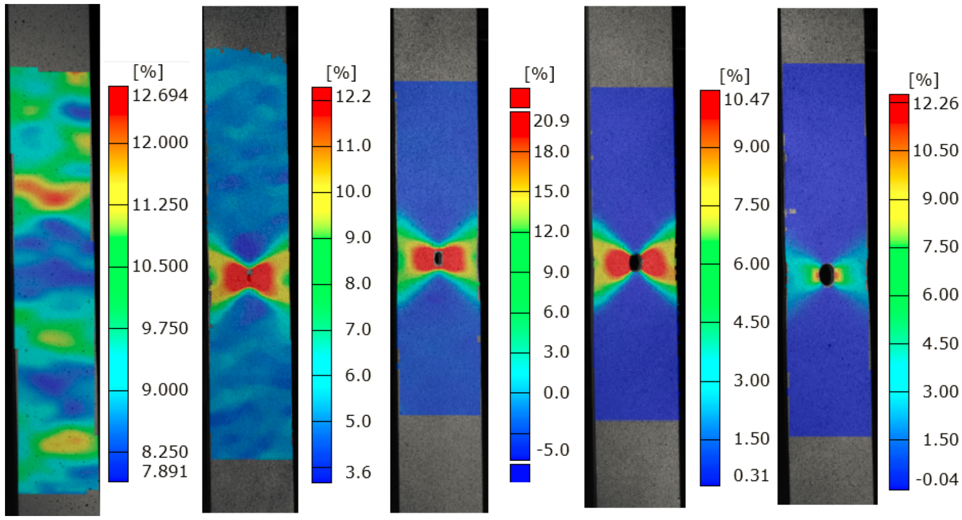

Figure 5.14: Longitudinal strain field on the aluminum specimen.

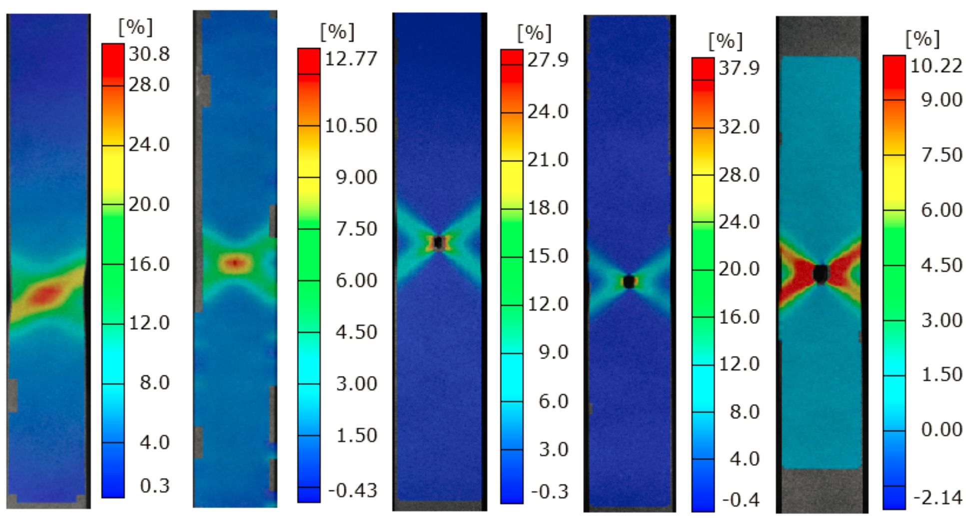

Figure 5.15: Longitudinal strain field on the high strength steel specimen.

The comparison of longitudinal strain distribution in the vicinity of the perforation with the diameter of $^1/_4$ of an inch for mild steel, aluminum, high strength steel and cast iron is shown in figure (5.17). Figure (5.17) clearly shows the presence of shear (L*ü*der) bands for ductile steel, aluminum and high strength steel, while the brittle cast iron does not show shear dependency.

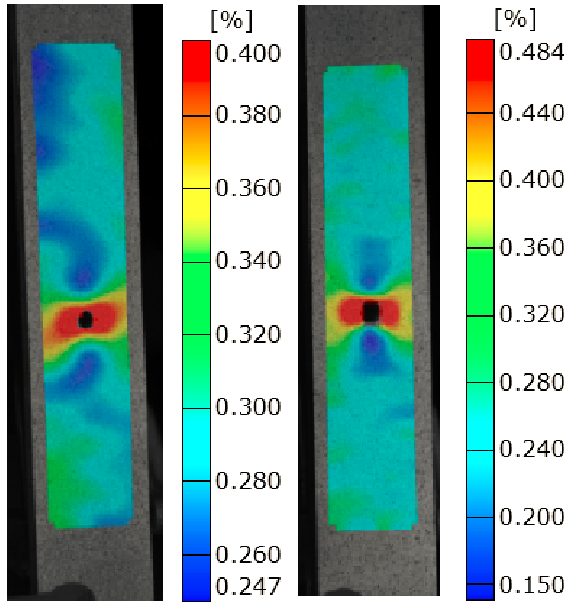

Figure 5.16: Longitudinal strain field on the cast iron specimen.

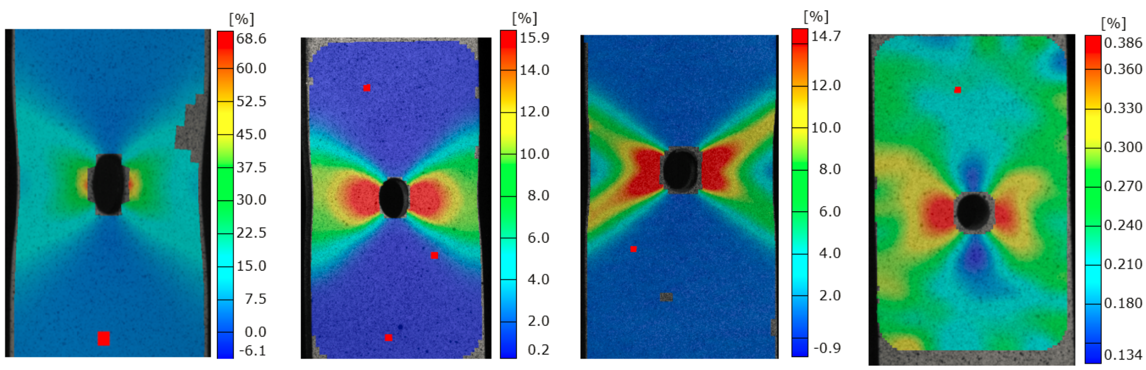

Figure 5.17: Longitudinal strain field, mild steel, aluminum, high strength steel and cast iron.

EXPERIMENTAL OBSERVATIONS ON CEMENTITIOUS SPECIMENS

Concrete cylinders are tested in compression and cyclic loading and unloading in compression. A Tinius Olsen compression machine is used to perform the tests under displacement control for twenty five concrete samples, and a digital image correlation system is used to capture the displacement field data at prescribed load steps and calculates the corresponding field strains. These samples are first painted in white and speckles of black paint is sprayed on the white background. This DIC system which is consisted of two 12 megapixel cameras is mounted in front of the samples in order to continuously record the relative movement of the black dots by assigning quadrilateral image details in form of so-called facets. The data are transferred into a computer and Aramis software is used for post processing reasons.

5.2.1 Experiments

The dimension of the tested specimens is depicted in figure (5.18). The mixture

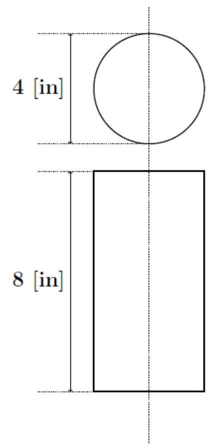

Figure 5.18: Dimension of the concrete specimen.

used to make these concrete specimens are tabulated in table (5.3). The mixture is based on the mass of the components and the values are normalized with respect to the mass of cement content. The fractured specimen under cyclic loading is depicted

Table 5.3: Mixture of the concrete specimens.

	Cement	Water	Sand	Aggregate
Normalized mass	1	0.5	1.53	2.37

in figure (5.19). It is observed that the concrete has failed in the direction perpendicular to the direction of the compression. The corresponding stress-strain curves of the uniaxial and cyclic compression tests are presented in figures (5.20) and (5.21) respectively.

Figure 5.19: Failed concrete specimen.

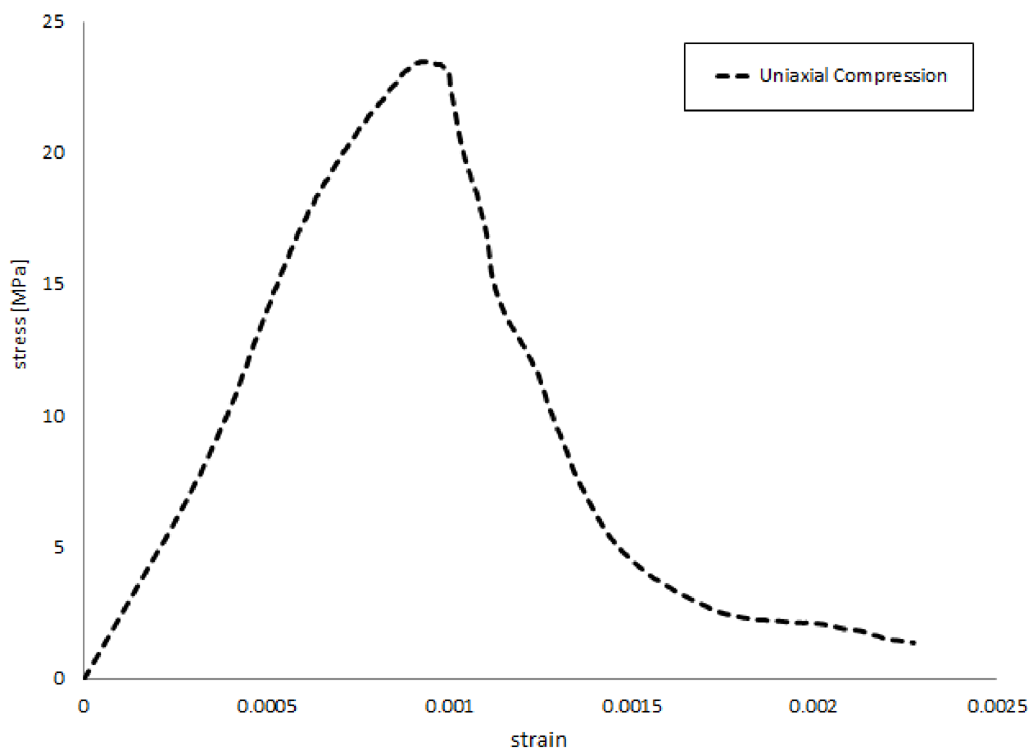

Figure 5.20: Stress-strain curve under uniaxial compression test.

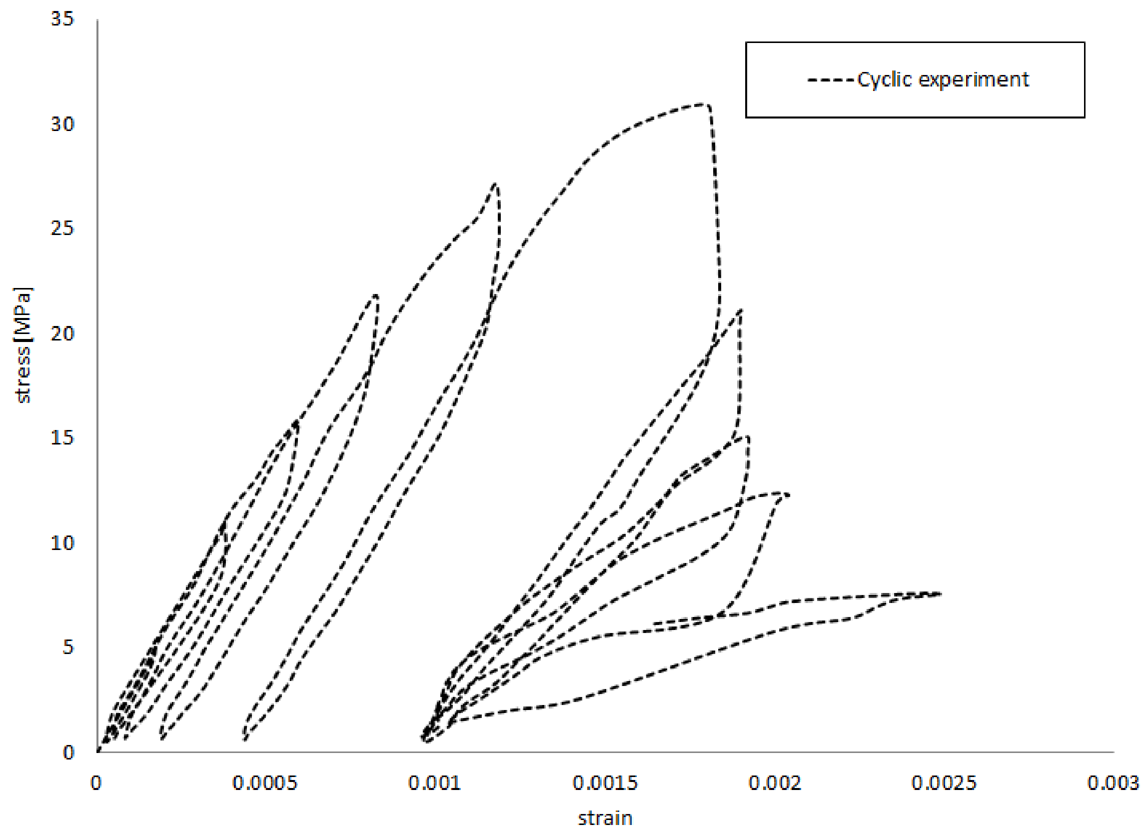

Figure 5.21: Stress-strain curve under cyclic compression test.

5.2.2 Digital Image Correlation Analysis

During the experiments the DIC systems takes pictures of the specimens at a constant pace and records the data on a computer. After the test is completed these data are used to post process the results and find the strain and displacement fields on the samples. The transverse displacement evolution of the concrete sample under compression for different stages of the experiment is depicted in figure (5.22). In the right figures it is observed that there is a jump in the transverse displacement which confirms the cracking of the specimen at that stage. The transverse infinitesimal strain distribution evolution over the concrete specimen for different stages is depicted in figure (5.23). The evolution of the discontinuities and jumps in the strains are visible in different stages of the experiment.

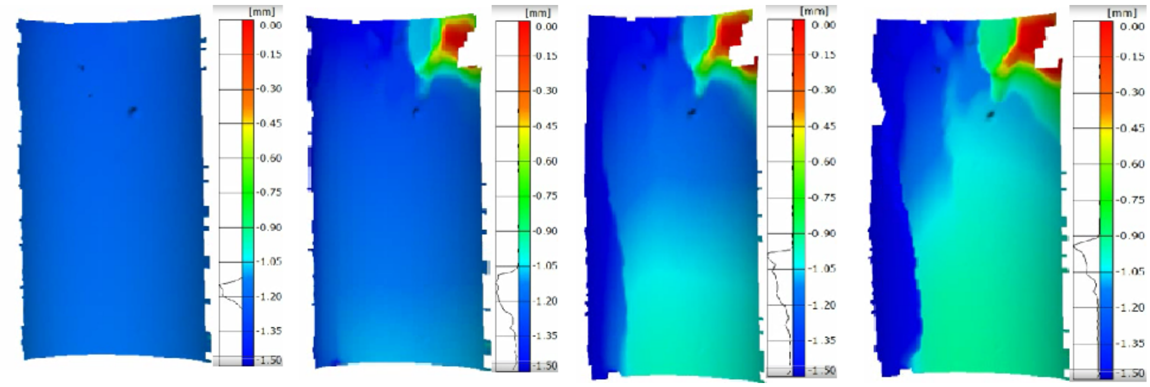

Figure 5.22: Evolution of the transverse displacement [mm] for different stages of the experiment.

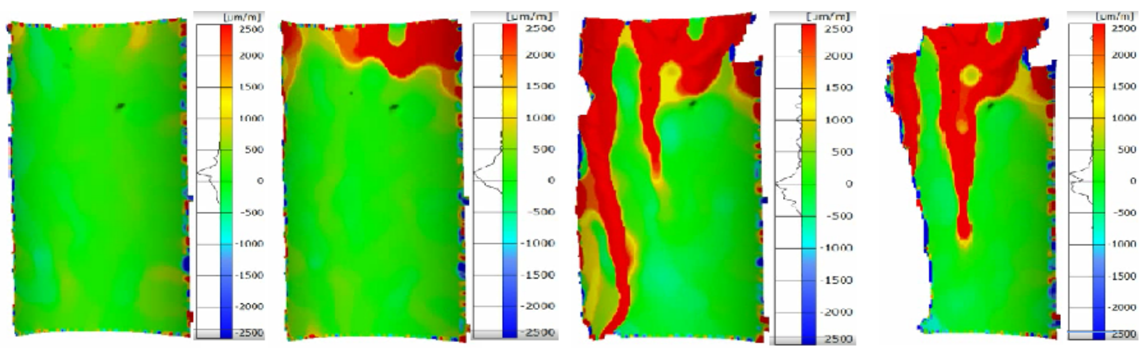

Figure 5.23: Evolution of the transverse strain for different stages of the experiment.

ERROR ANALYSIS OF DIC DATA WITH LEAST SQUARE APPROXIMATION

The facet data that are captured by Digital Image Correlation (DIC) system are used in the Aramis software to come up with field data and distribution of the displacement field and calculating the infinitesimal as well as finite and logarithmic strains. In this section the raw facet data are extracted from the Aramis software and are treated as the exact spatial position and displacement of the material points to come up with the best finite element representation of the displacement field based on the least square method. As an example, the data are extracted from the aluminum sample without perforation, these data are depicted in figure (5.24) where the left image is showing the facet data at the beginning of the tension test and the right image is showing the data prior to failure and cracking of the specimen. The schematic

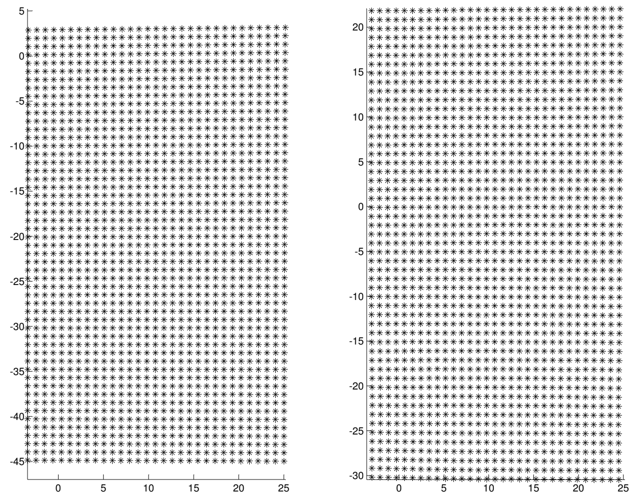

Figure 5.24: Facet data of aluminum flat bar captured by DIC.

of facet data distribution on the perforated aluminum specimen is shown in figure (5.25), note that only a fraction of facet data are shown. Having the facet data, a

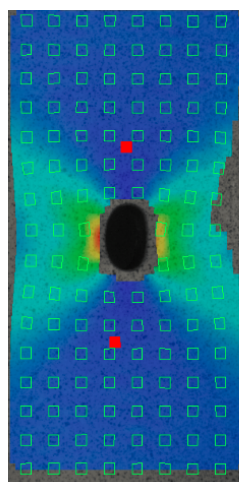

Figure 5.25: Facet distribution on the measurement surface.

finite element mesh is generated on the domain that covers the facet data and the procedures of least square are performed in order to have the nodal displacement values that best represent the facet data and consequently the best approximation of the displacement field based on least square method. This procedure is briefly described here. The goal is to minimize the squared of displacement differences as

$$F = \sum_{i=1}^{NrElm} \sum_{j=1}^{NFP} (\Delta \bar{u}^* - \Delta u^{DIC})_j^2, \tag{5.1}$$

where NFP stands for number of facet points, $\Delta \bar{u}^*$ is the smoothed displacement over an element and $\Delta \boldsymbol{u}^{DIC}$ is the vector of facet data inside each element. For each element $\Delta \bar{u}^*$ may be expressed as

$$\Delta \bar{u}_j^* = N_{ji} \Delta u_i^* \quad \text{or} \quad \Delta \bar{\boldsymbol{u}}^* = \boldsymbol{N}.\Delta \boldsymbol{u}^*, \tag{5.2}$$

where $\Delta \boldsymbol{u}^*$ is the vector of nodal values of displacement which is unknown at this stage. The minimum error is achieved when derivative of function F is set to zero,

$$\frac{\partial F}{\partial \Delta \boldsymbol{u}^*} = 0 \quad \Longrightarrow \quad 2(\Delta \bar{u}_j^* - \Delta u_j^{DIC}) \frac{\partial \Delta \bar{u}_j^*}{\partial \Delta u_k^*} = 0 \quad \Longrightarrow \quad (N_{ji} \Delta u_i^* - \Delta u_j^{DIC}) N_{jk} = 0. \tag{5.3}$$

In equation (5.3) $\boldsymbol{N}$ is the matrix of shape functions associated with the element and number of facet data inside the element. Finally equation (5.3) is expressed in terms of nodal displacements as

$$\Delta \boldsymbol{u}^* = (\boldsymbol{N} \cdot \boldsymbol{N})^{-1} \cdot (\boldsymbol{N} \cdot \Delta \boldsymbol{u}^{DIC}). \tag{5.4}$$

In order to solve this equation and find the best nodal displacement values, a search algorithm is used to locate the facet data associated with each element. In order to find the error of this method and find out what types of element could best represent the facet data three types of elements are chosen, a four node quadrilateral element (Q_4), an eight node serendipity element (Q_8) and a nine node Lagrange element (Q_9). The shape functions are defined as $\boldsymbol{N} = \boldsymbol{P} \cdot \boldsymbol{C}^{-1}$ where for a Q_4 element $\boldsymbol{C}$ and $\boldsymbol{P}$

defined as

$$\boldsymbol{C} = \begin{pmatrix} 1 & x_1 & y_1 & x_1y_1 \\ 1 & x_2 & y_2 & x_2y_2 \\ 1 & x_3 & y_3 & x_3y_3 \\ 1 & x_4 & y_4 & x_4y_4 \end{pmatrix}, \quad \boldsymbol{P} = \begin{pmatrix} 1 \\ x \\ y \\ xy \end{pmatrix}. \tag{5.5}$$

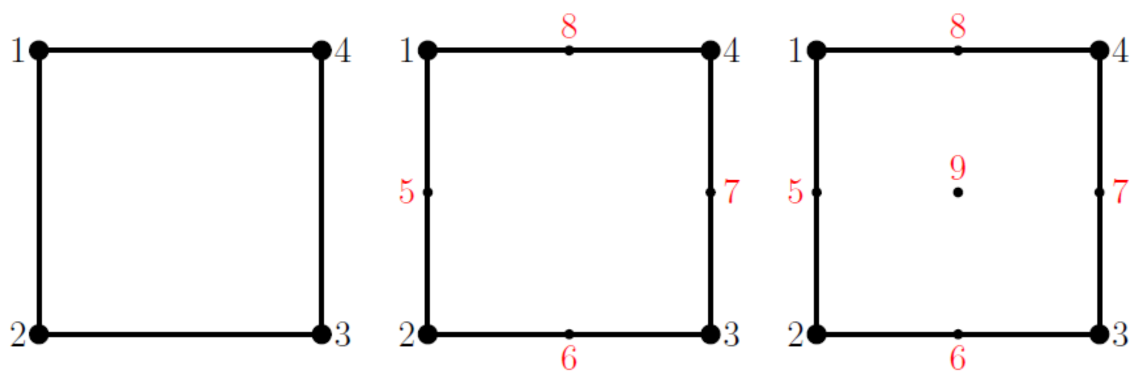

Figure 5.26: Q_4, Q_8 and Q_9 elements.

Similarly the matrix $\boldsymbol{C}$ and vector $\boldsymbol{P}$ associated with Q_8 and Q_9 elements are expressed in equations (5.6) and (5.7),

$$\boldsymbol{C} = \begin{pmatrix} 1 & x_1 & y_1 & x_1y_1 & x_1^2 & y_1^2 & x_1y_1^2 & x_1^2y_1 \\ 1 & x_2 & y_2 & x_2y_2 & x_2^2 & y_2^2 & x_2y_2^2 & x_2^2y_2 \\ 1 & x_3 & y_3 & x_3y_3 & x_3^2 & y_3^2 & x_3y_3^2 & x_3^2y_3 \\ 1 & x_4 & y_4 & x_4y_4 & x_4^2 & y_4^2 & x_4y_4^2 & x_4^2y_4 \\ 1 & x_5 & y_5 & x_5y_5 & 0 & y_5^2 & x_5y_5^2 & 0 \\ 1 & x_6 & y_6 & x_6y_6 & x_6^2 & 0 & 0 & x_6^2y_6 \\ 1 & x_7 & y_7 & x_7y_7 & 0 & y_7^2 & x_7y_7^2 & 0 \\ 1 & x_8 & y_8 & x_8y_8 & x_8^2 & 0 & 0 & x_8^2y_8 \end{pmatrix}, \quad \boldsymbol{P} = \begin{pmatrix} 1 \\ x \\ y \\ xy \\ x^2 \\ y^2 \\ xy^2 \\ x^2y \end{pmatrix} \quad \text{and} \tag{5.6}$$

$$
\boldsymbol{C} = \begin{pmatrix}
1 & x_1 & y_1 & x_1y_1 & x_1^2 & y_1^2 & x_1y_1^2 & x_1^2y_1 & x_1^2y_1^2 \\
1 & x_2 & y_2 & x_2y_2 & x_2^2 & y_2^2 & x_2y_2^2 & x_2^2y_2 & x_2^2y_2^2 \\
1 & x_3 & y_3 & x_3y_3 & x_3^2 & y_3^2 & x_3y_3^2 & x_3^2y_3 & x_3^2y_3^2 \\
1 & x_4 & y_4 & x_4y_4 & x_4^2 & y_4^2 & x_4y_4^2 & x_4^2y_4 & x_4^2y_4^2 \\
1 & x_5 & y_5 & x_5y_5 & x_5^2 & y_5^2 & x_5y_5^2 & x_5^2y_5 & x_5^2y_5^2 \\
1 & x_6 & y_6 & x_6y_6 & x_6^2 & y_6^2 & x_6y_6^2 & x_6^2y_6 & x_6^2y_6^2 \\
1 & x_7 & y_7 & x_7y_7 & x_7^2 & y_7^2 & x_7y_7^2 & x_7^2y_7 & x_7^2y_7^2 \\
1 & x_8 & y_8 & x_8y_8 & x_8^2 & y_8^2 & x_8y_8^2 & x_8^2y_8 & x_8^2y_8^2 \\
1 & x_9 & y_9 & x_9y_9 & x_9^2 & y_9^2 & x_9y_9^2 & x_9^2y_9 & x_9^2y_9^2
\end{pmatrix}, \quad \boldsymbol{P} = \begin{pmatrix} 1 \\ x \\ y \\ xy \\ x^2 \\ y^2 \\ xy^2 \\ x^2y \\ x^2y^2 \end{pmatrix}. \tag{5.7}
$$

In above equations x_i and y_i are x and y coordinates of the nodes of the elements and x and y define the spatial position of the facet data inside the element, finally the multiplication of matrix $\boldsymbol{C}^{-1}$ and vector $\boldsymbol{P}$ provides the value of the shape functions at the facet point of interest. The nodal positions are depicted in figure (5.26), the node numbering is counter clockwise. In order to find out which type of element has a better representation of the facet data with less error, an error analysis is performed for Q_4, Q_8 and Q_9 element types based on the data of the non perforated aluminum at the initial and final stage of the experiment. A closer look at the elements containing facet data is shown in figure (5.27). The error analysis is performed for

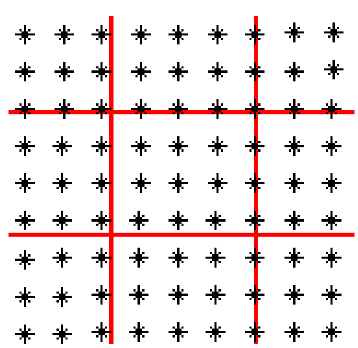

Figure 5.27: Facet data distribution inside the elements.

different number of elements starting from two and increasing to 128 elements as shown in figure (5.28). The results of error analysis for these elements considering

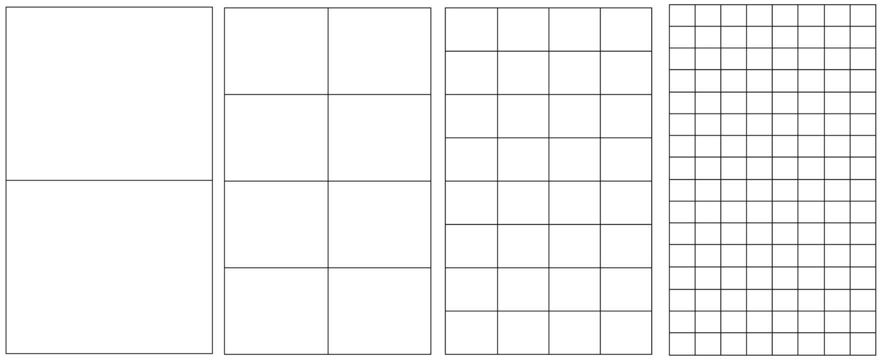

Figure 5.28: Finite element mesh with different number of elements.

three different element types is depicted in figure (5.29). It should be noted that

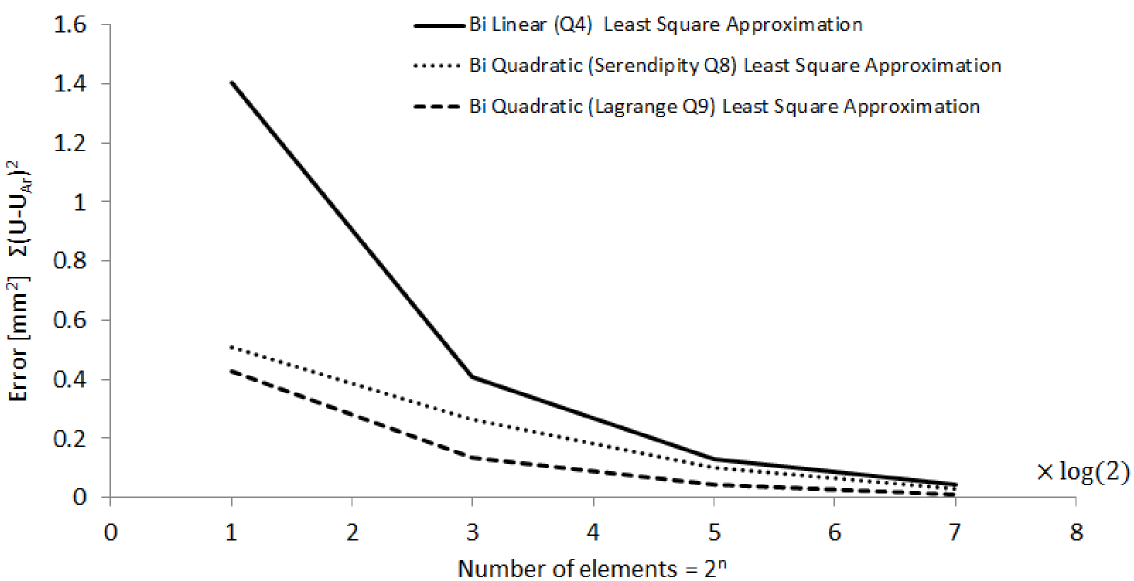

Figure 5.29: Error analysis based on least square for different elements.

the horizontal axis of figure (5.29) is a logarithmic axis in order to have a better presentation of the results. It is observed from this figure that error is decreasing by increasing the number of elements, however if the facet data inside the element are less than the number of nodes, the error is going to increase, i.e., increasing number of elements will only help if the number of facet data are sufficient for each element.

It is also observed that the error associated with the Q_9 element is lower than the two other element types and therefore it is a better choice, however if the number of elements is sufficiently large, the difference is minimal.

Having the best nodal displacement values based on DIC facet data, it is possible to calculate infinitesimal and finite strain distribution. In order to calculate small strain the gradient of the shape functions are calculated at each element and then multiplied by the nodal displacements as

$$\boldsymbol{\epsilon}_{ele} = \boldsymbol{B}.\Delta\boldsymbol{u}_{ele}, \tag{5.8}$$

where

$$\boldsymbol{B} = \begin{pmatrix} \frac{\partial N_1}{\partial x} & 0 & \frac{\partial N_2}{\partial x} & 0 & \dots & \frac{\partial N_i}{\partial x} & 0 \\ 0 & \frac{\partial N_1}{\partial y} & 0 & \frac{\partial N_2}{\partial y} & \dots & 0 & \frac{\partial N_i}{\partial y} \\ \frac{\partial N_1}{\partial y} & \frac{\partial N_1}{\partial x} & \frac{\partial N_2}{\partial y} & \frac{\partial N_2}{\partial x} & \dots & \frac{\partial N_i}{\partial y} & \frac{\partial N_i}{\partial x} \end{pmatrix} \tag{5.9}$$

and

$$\Delta\boldsymbol{u}_{ele} = \begin{pmatrix} \Delta u_{x1} & \Delta u_{y1} & \Delta u_{x2} & \Delta u_{y2} & \dots & \Delta u_{xi} & \Delta u_{yi} \end{pmatrix}^T. \tag{5.10}$$

In order to calculate the finite strains two stages of the experiment is required, one is the initial configuration and the other one is the current configuration. Having the nodal coordinates of initial and current stages, the gradient of displacements are calculated as

$$\boldsymbol{F}(1:2,1:2) = \begin{pmatrix} x_1 \\ y_1 \end{pmatrix} \begin{pmatrix} \frac{\partial N_1}{\partial x} & \frac{\partial N_1}{\partial y} \end{pmatrix} + \begin{pmatrix} x_2 \\ y_2 \end{pmatrix} \begin{pmatrix} \frac{\partial N_2}{\partial x} & \frac{\partial N_2}{\partial y} \end{pmatrix} + \dots + \begin{pmatrix} x_i \\ y_i \end{pmatrix} \begin{pmatrix} \frac{\partial N_i}{\partial x} & \frac{\partial N_i}{\partial y} \end{pmatrix} \tag{5.11}$$

and $\boldsymbol{F}(3,1:2)$ and $\boldsymbol{F}(1:2,3)$ are zero and $\boldsymbol{F}(3,3)$ is equal to one. Therefore the

Green's (Lagrangian) finite strain tensor is expressed as

$$\boldsymbol{E}^G = \frac{1}{2}(\boldsymbol{F} \cdot \boldsymbol{F} - \mathbf{1}). \tag{5.12}$$

Having the proper formulation, the facet data of an aluminum flat bar with circular perforation of $^1/_4$ of inch is extracted in order to perform the least square analysis. Abaqus software is used to generate the finite element mesh. The finite element mesh and facet distribution in the vicinity of the perforation for the finite element mesh are depicted in figures (5.30) and (5.31).

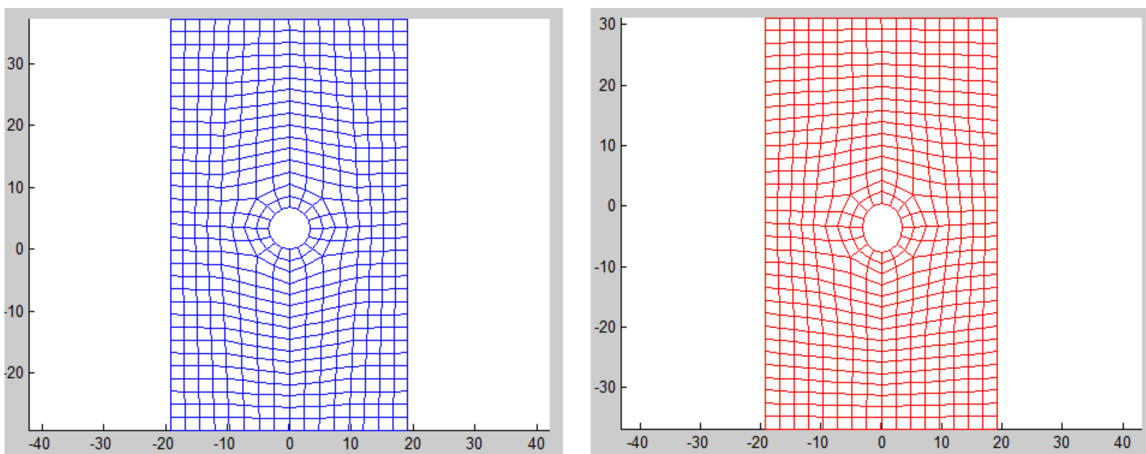

Figure 5.30: Initial and final mesh.

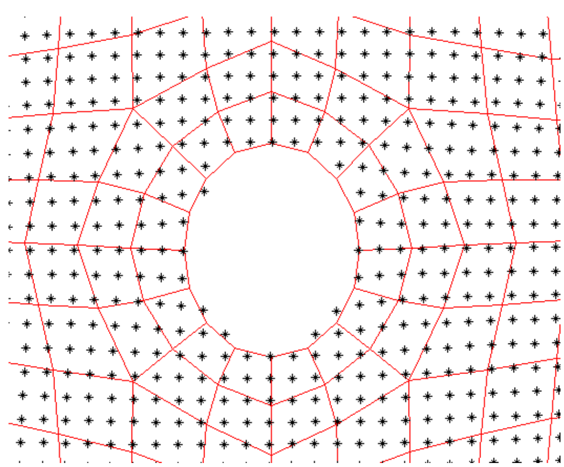

Figure 5.31: Facet distribution in the vicinity of perforation.

The least square analysis based on a Q_4 element is performed and the calculated error is 0.6492 $[mm^2]$. The comparison of the DIC observations and the least square approximation of the facet data are presented in figures (5.32), (5.33), (5.34), (5.35), (5.36) and (5.37). The strain field distribution based on least square approximation of displacement data is showing higher values at the edge of the perforation, this might be due to the fact that the finite element representation of the facet data is capable of presenting strain data at the edge of the circular perforation while the Aramis strain field does not cover there. The same comparison could be made based on finite strain formulation. It should be noted that although the strains are different for the perforated specimen, for the non perforated specimen, the strains are almost the same.

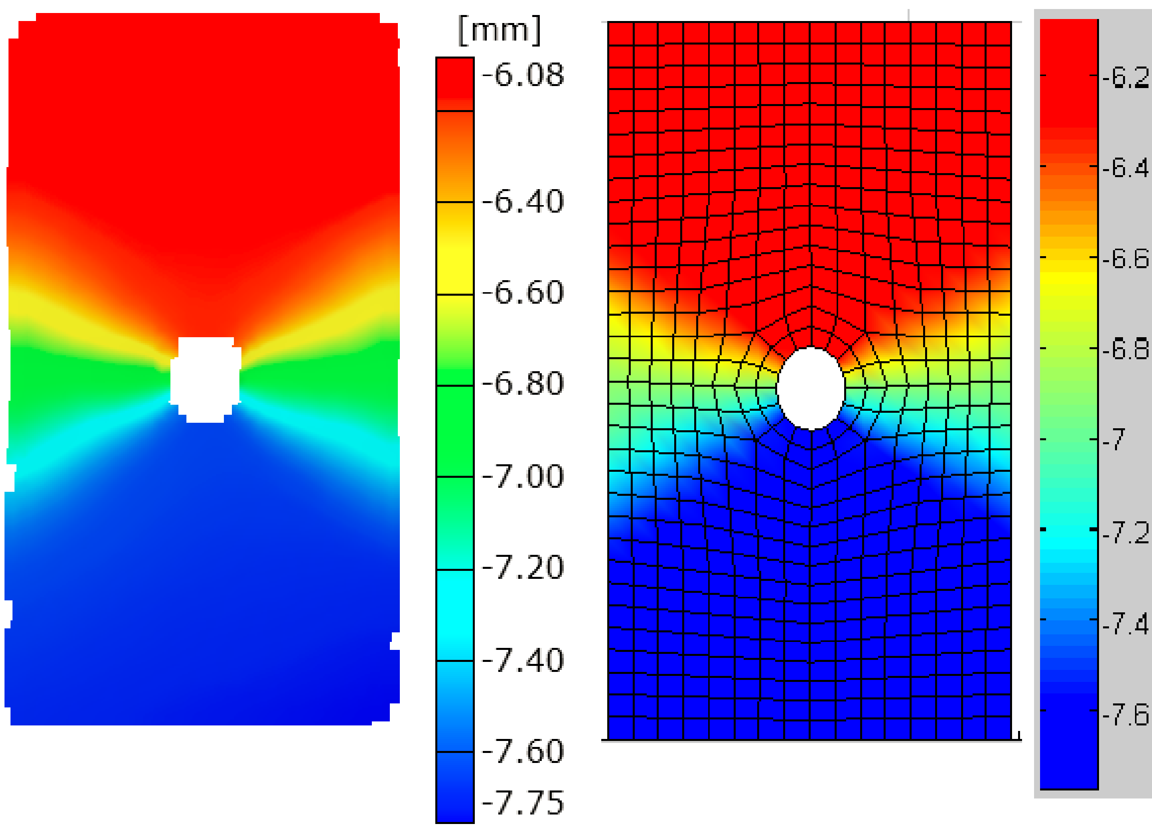

Figure 5.32: Longitudinal displacement [mm], left: DIC observation, right: least square approximation.

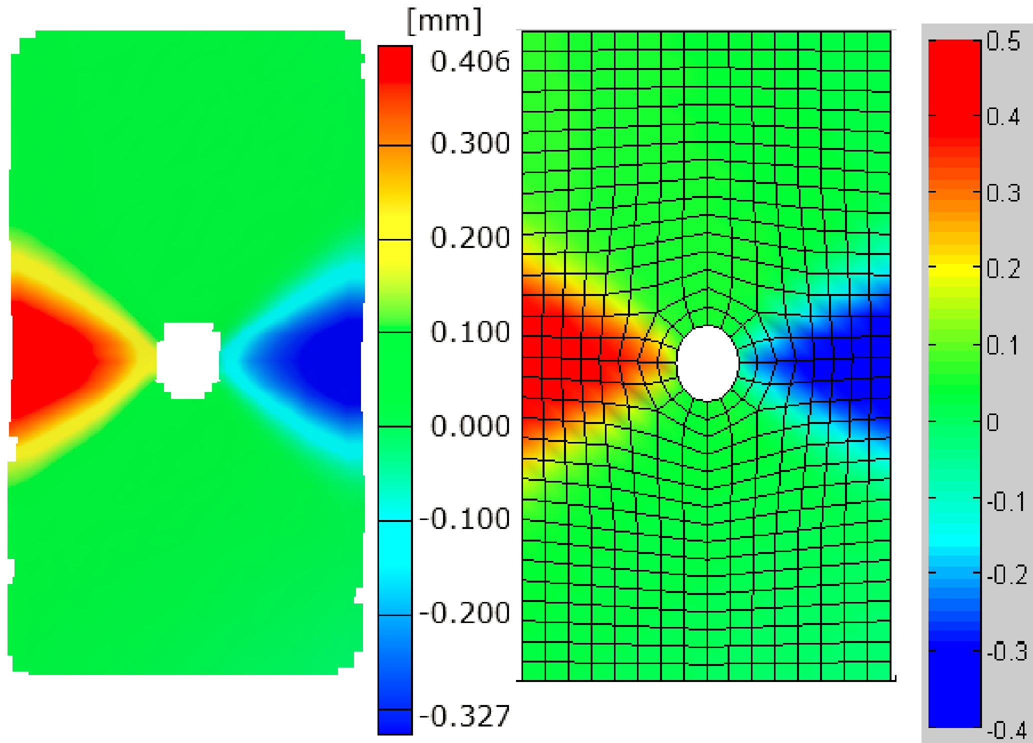

Figure 5.33: Transverse displacement [mm], left: DIC observation, right: least square approximation.

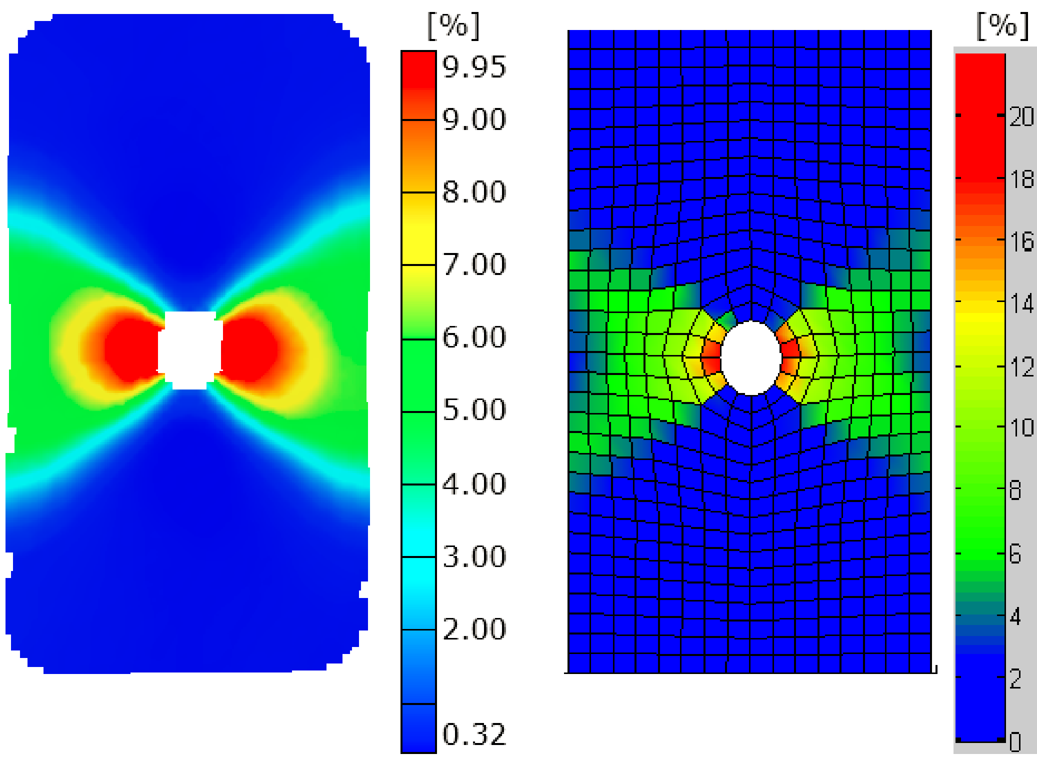

Figure 5.34: Longitudinal strain %, left: DIC observation, right: least square approximation.

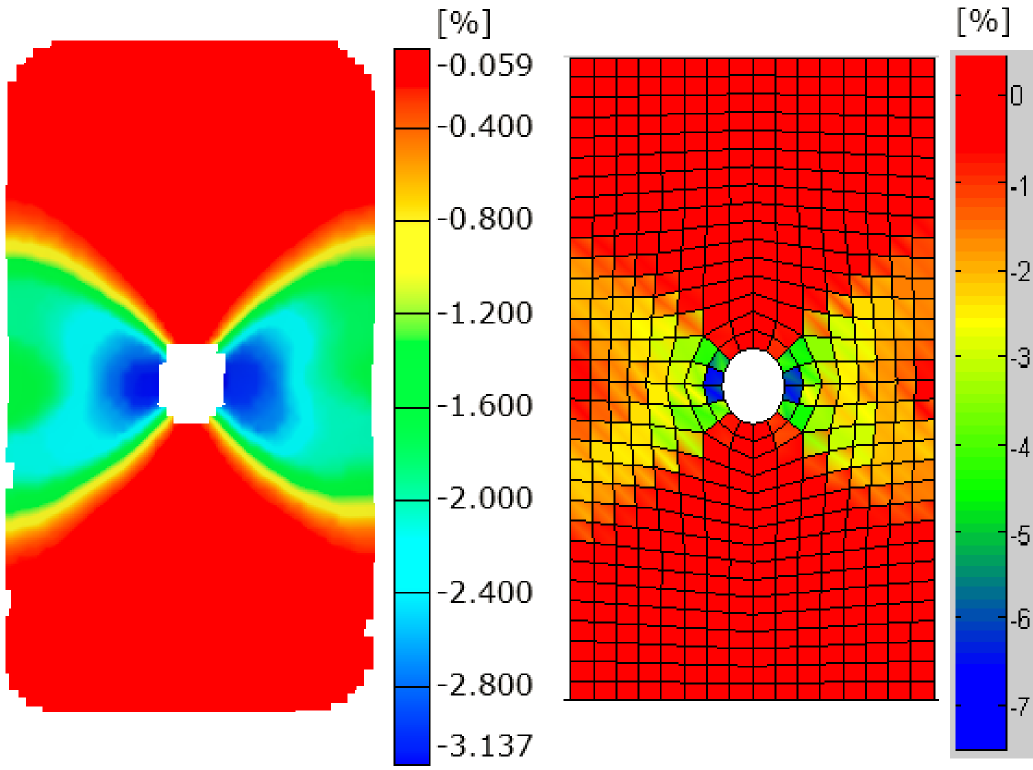

Figure 5.35: Transverse strain %, left: DIC observation, right: least square approximation.

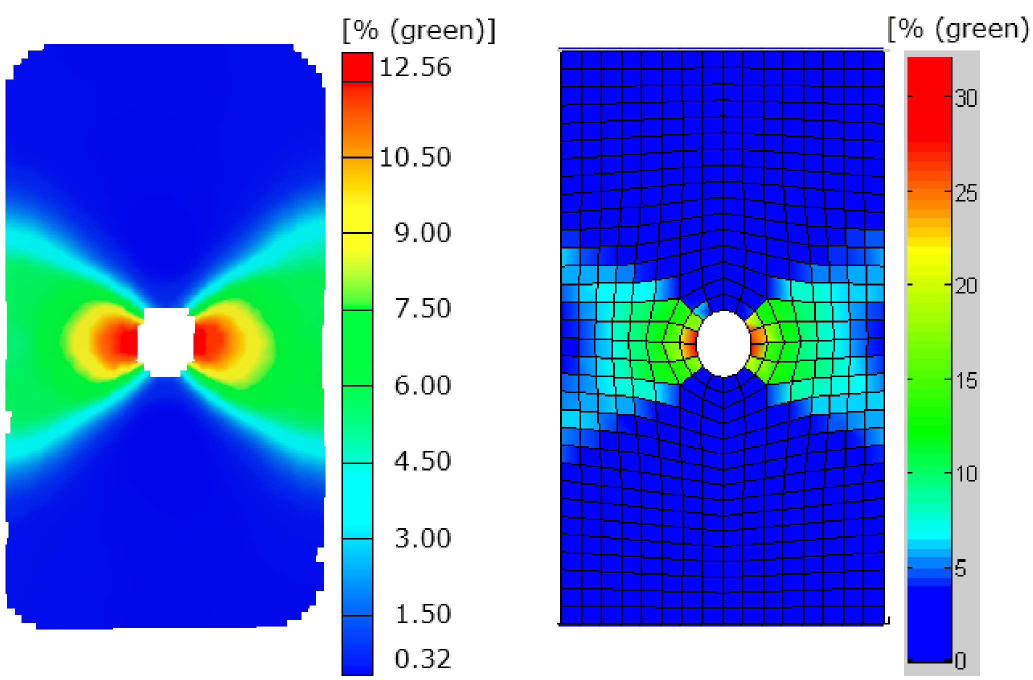

Figure 5.36: Longitudinal finite strain %, left: DIC observation, right: least square approximation.

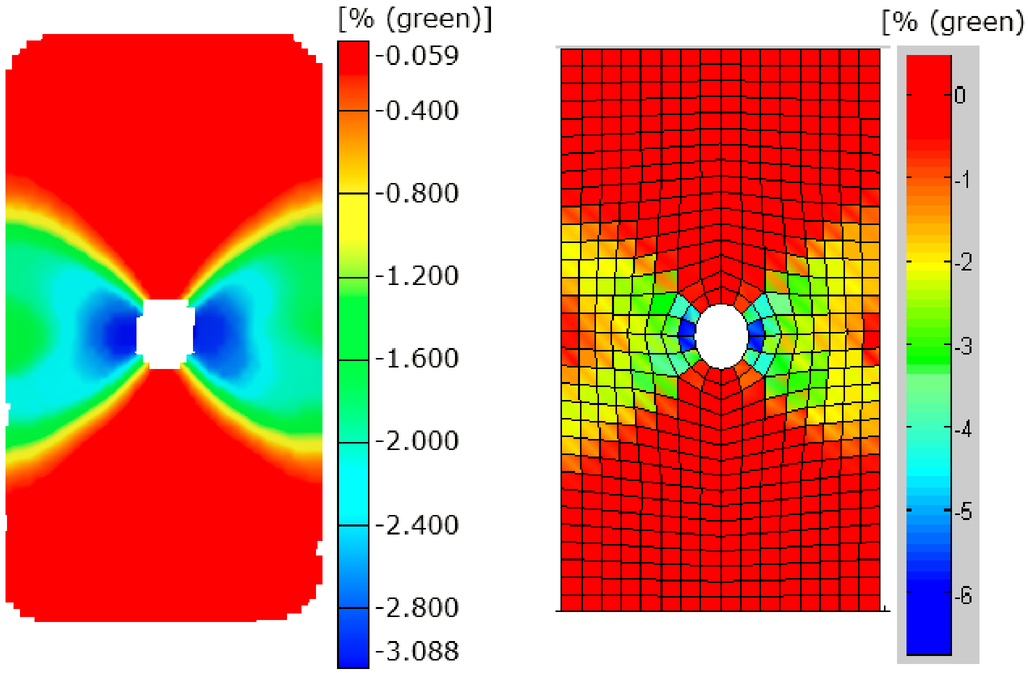

Figure 5.37: Transverse finite strain %, left: DIC observation, right: least square approximation.

In order to investigate this difference in the strain distribution, two cases are studied. The first one is the data derived from DIC based on facet size of 15 pixels and facet step of 9 pixels and the second one has the facet size of 11 pixels and facet step of 7 pixels. The information related to these tests is presented in table (5.4).

Table 5.4: DIC data for different facet size.

	size	step	No.	ϵ_y %	ϵ_x %	ϵ_y^G %	ϵ_x^G %
Test 1	15	9	3598	0.32↔9.95	-0.06↔-3.14	0.32↔12.56	-0.06↔-3.088
Test 2	11	7	7989	-1.17↔12.55	-3.91↔2.45	-1.1↔32.3	-7.83↔4.45

From these two different tests, it is observed that the change in the facet size has drastically affected the infinitesimal and finite strain values calculated by Aramis software and in extreme cases the difference is about 200% as shown in figure (5.38). Both of these facet data are extracted and the best finite element approximation of the displacement field is calculated based on the least square method. Based on the equations mentioned earlier the infinitesimal and final strains are derived and the results are shown in table (5.5).

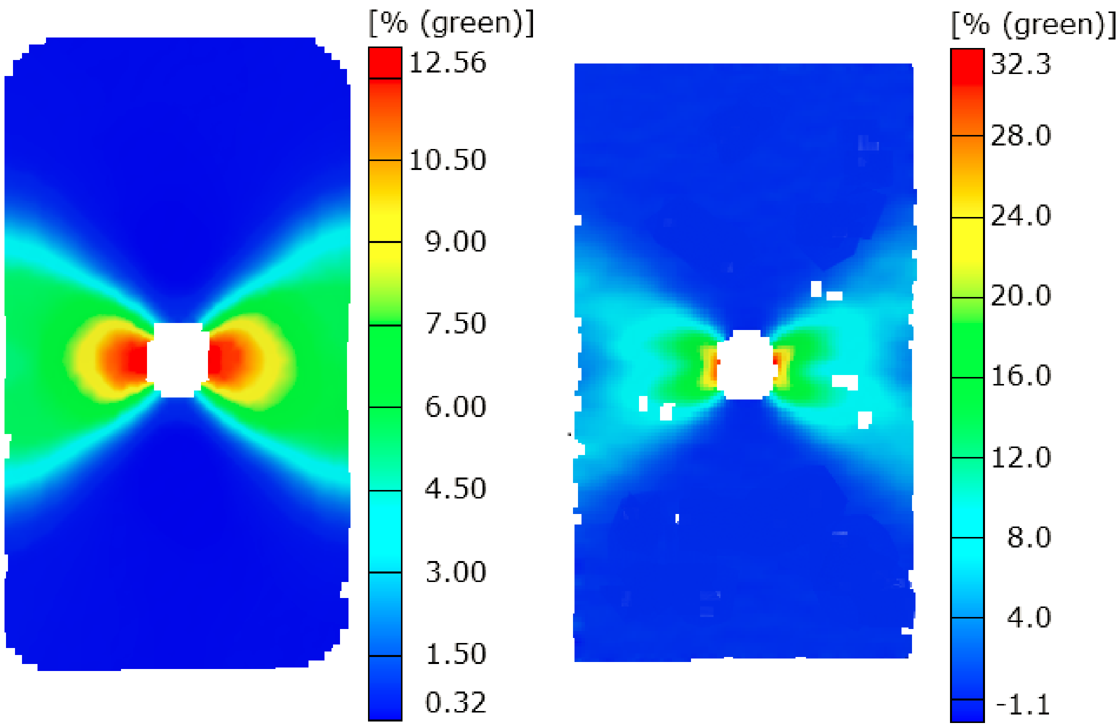

Figure 5.38: Difference in strain for the same stage due to different facet sizes.

Table 5.5: FE appoximation of the facet data for difeerent facet sizes.

	ϵ_y %	ϵ_x %	ϵ_y^G %	ϵ_x^G %
Test 1	-0.04↔ 21.96	-7.49↔0.46	-0.04↔32.14	-6.73↔0.46
Test 2	-0.81↔21.51	-6.43↔0.46	-0.79↔ 31.19	-5.87↔0.74

From table (5.5) it is concluded that the change in the number of facets does not significantly change the finite and infinitesimal strains of the least square approximation and therefore confirms the robustness of the results obtained by the least square approximation and finite element discretization. The comparison of strain distribution in the vicinity of perforation for different facet sizes is depicted in figure (5.39).

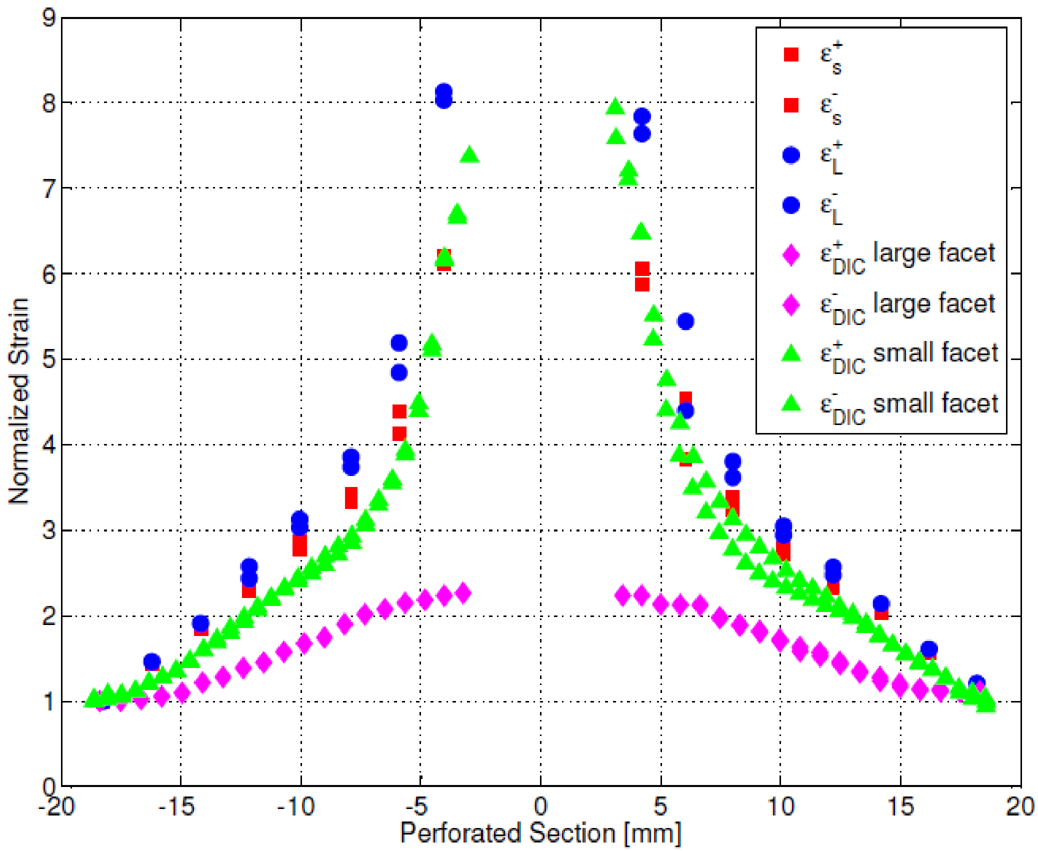

Figure 5.39: Difference in strain distribution in the vicinity of perforation at the same load stage for different facet sizes.

Chapter 6. Simulations

This chapter includes the results of numerical modeling of the fracture of ductile and brittle materials earlier introduced in this dissertation. The first section is dedicated to numerical results obtained for metallic specimens and starts with the calibration of the numerical models proposed for mild steel, aluminum, high strength steel and cast iron based on the experimental observations performed on the flat bars. Then the concept of inelastic XFEM is introduced by coupling localization analysis and extended finite element and the ductile and brittle behavior of these specimens is examined and investigated by acquiring different failure criteria and localization properties.

The second part of this chapter is the numerical modeling of concrete specimen and contains the calibration of the concrete models proposed earlier based on the uniaxial and cyclic experiments performed on concrete cylinders. Then the numerical localization analysis is performed for the damage, plastic and damage-plasticity models where the differences of the localization properties of these models is discussed and assessed based on the observations achieved by experiments.

SIMULATION OF METALLIC SPECIMENS

In order to simulate the behavior of the metallic specimens, the experimental data of the non perforated specimens is extracted and used for calibration of the proposed models in this work. These models includes the von Mises istotropic hardening/softening plasticity formulation for mild steel, high strength steel and aluminum and the St. Venant criterion for cast iron. These criteria are used in order to trigger the onset of plastification for the ductile specimens and the onset of brittle failure for cast iron, however for the case of ductile material another criterion has to be achieved before the material behavior becomes unstable and the crack growth rapidly ruptures the specimen, this criterion is expressed in terms of the strain invariants since it is preceded by huge plastification. The second deviatoric invariant is more important in this work because of the nature of the ductile failure, however the first invariant could also be of importance. In summary, two criteria are required for ductile failure, the first one in terms of stresses to account for plasticity and the second one in terms of strains to initiate cracking, while for the brittle failure one criterion is sufficient and it could be either in terms of strains or stresses. Afterwards the direction of the failure is predicted based on the localization analysis of the failure criteria. It should be noted that in this work the localization analysis of the strain format of the von Mises and Tresca criteria is considered for ductile material while for the cast iron the localization properties of the St. Venant or Rankine criteria is used.

6.1.1 Calibration of the Numerical Models

In the case of mild steel, a linear elastic numerical model is assumed up to the yielding, the von Mises plasticity with isotropic hardening coupled with extended finite element method and localization analysis is used for the post yield behavior and this model is calibrated with the experimental results obtained from the non-perforated experiments. The comparison of the calibrated model and experimental results is depicted in figure (6.1). The stress values that are used for calibration are the true stress values and are obtained as

$$\sigma^{true} = (1 + \epsilon^{nom})\, \sigma^{nom}. \tag{6.1}$$

The corresponding load-deformation curves of the calibrated models for mild steel and aluminum in the case of non-perforated specimens are depicted in figures (6.1) and (6.2) respectively. In these pictures the continuous line is used for the simulation results and the dotted line is used for the experimental data. The stress-strain curve of the calibrated model for cast iron is depicted in figure (6.3).

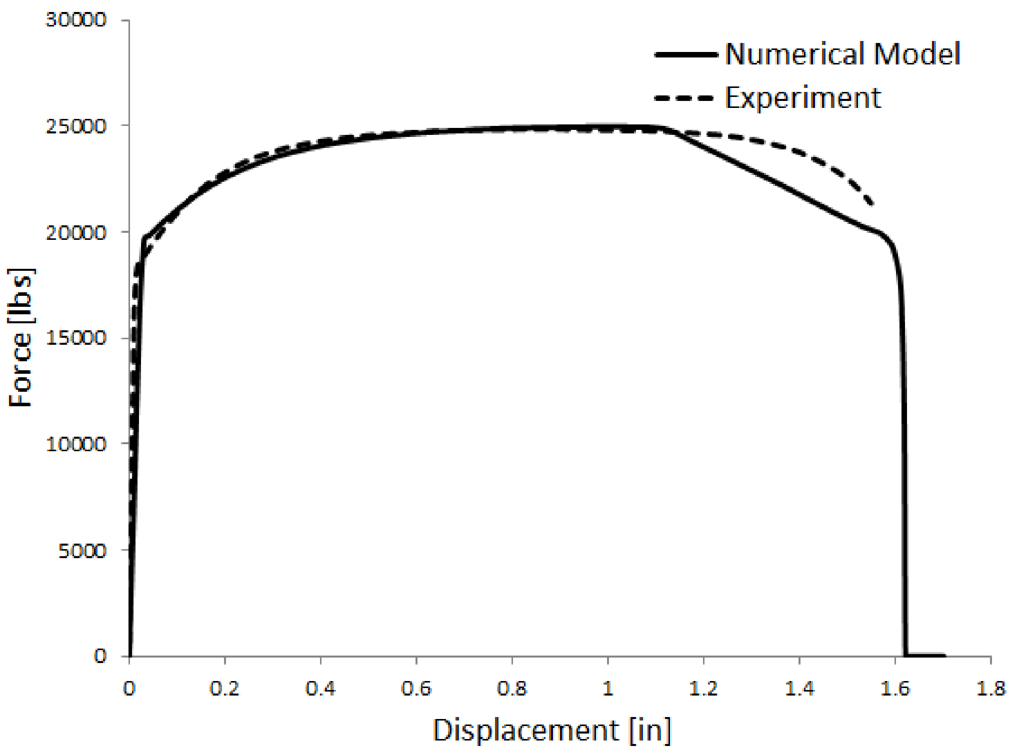

Figure 6.1: Comparison of the load-deformation of the experiment and numerical model for mild steel.

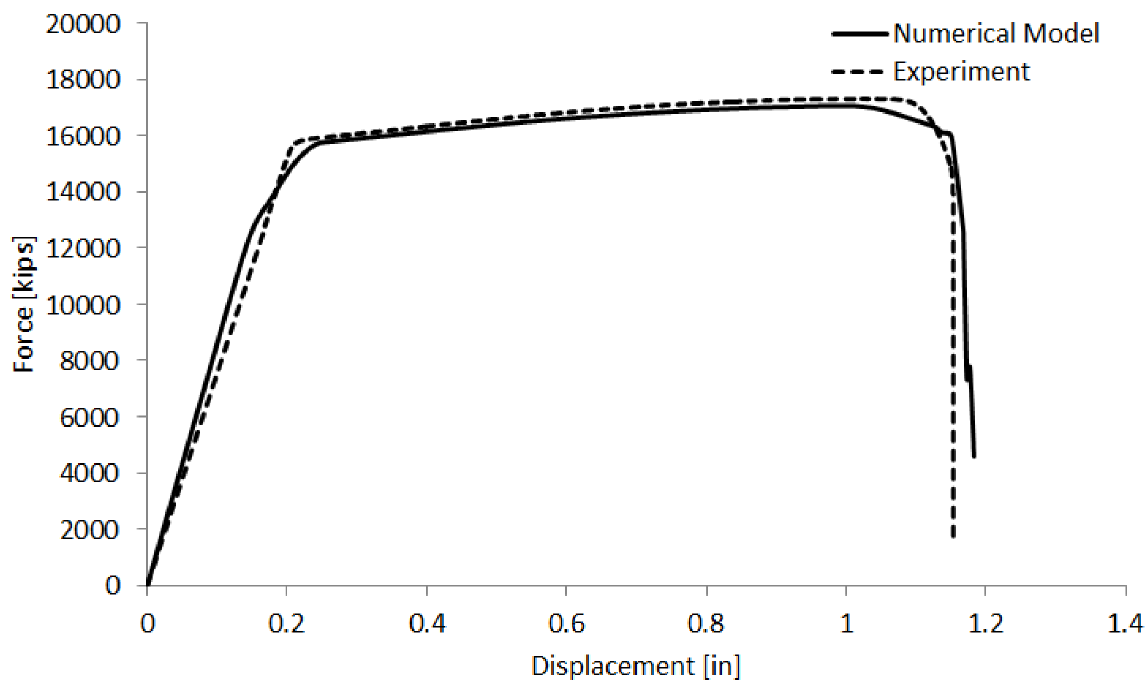

Figure 6.2: Comparison of the load-deformation of the experiment and numerical model for aluminum.

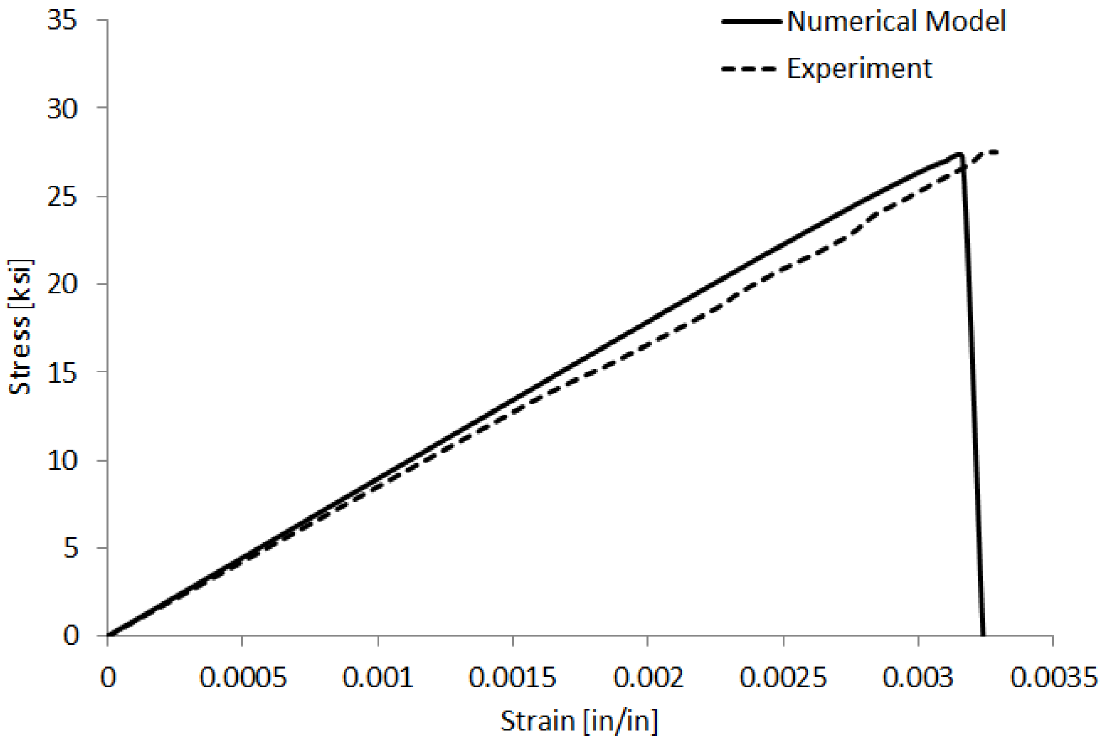

Figure 6.3: Comparison of the stress-strain curves of the experiment and numerical model for cast iron.

6.1.2 Analysis of the Failure Direction

In this part three different failure criteria are implemented in UDMGINI in order to trigger the onset of discrete failure and cracking. The header of the UDMGINI subroutine is depicted in figure (6.4). These criteria are St. Venant's maximum principal strain which is used for cast iron, Tresca maximum shear stress and von Mises that are used for mild steel and aluminum specimens. Since cast iron has a brittle behavior the St. Venant or Rankine criteria can be used for the initiation of the failure and the localization analysis of these criteria will result in a failure direction that is perpendicular to the direction of the maximum principal stress or strain. A comparison of the experimental observations and numerical models for the perforated cast iron specimen is presented in figure (6.5). For the ductile materials that are used here, the Tresca and von Mises criteria are used to predict the failure directions. For Tresca criteria the localization analysis is performed earlier in this

```fortran
C     Written by Shahriyar Beizaee
C     University of Houston
C     Department of Civil and Environmental Engineering

      SUBROUTINE UDMGINI(FINDEX,NFINDEX,FNORMAL,NDI,NSHR,NTENS,PROPS,
     1 NPROPS,STATEV,NSTATEV,STRESS,STRAIN,STRAINEE,LXFEM,TIME,
     2 DTIME,TEMP,DTEMP,PREDEF,DPRED,NFIELD,COORDS,NOEL,NPT,
     3 KLAYER,KSPT,KSTEP,INC,KDIRCYC,KCYCLELCF,TIMECYC,SSE,SPD,
     4 SCD,SVD,SMD,JMAC,JMATYP,MATLAYO,LACCFLA,CELENT,DROT,ORI)
C
      INCLUDE 'ABA_PARAM.INC'
C
      DIMENSION FINDEX(NFINDEX),FNORMAL(NDI,NFINDEX),COORDS(*),
     1 STRESS(NTENS),STRAIN(NTENS),STRAINEE(NTENS),PROPS(NPROPS),
     2 STATEV(NSTATEV),PREDEF(NFIELD),DPRED(NFIELD),TIME(2),
     3 JMAC(*),JMATYP(*),DROR(3,3),ORI(3,3)
C
```

Figure 6.4: UDMGINI function for implementation of failure criteria and localization analysis.

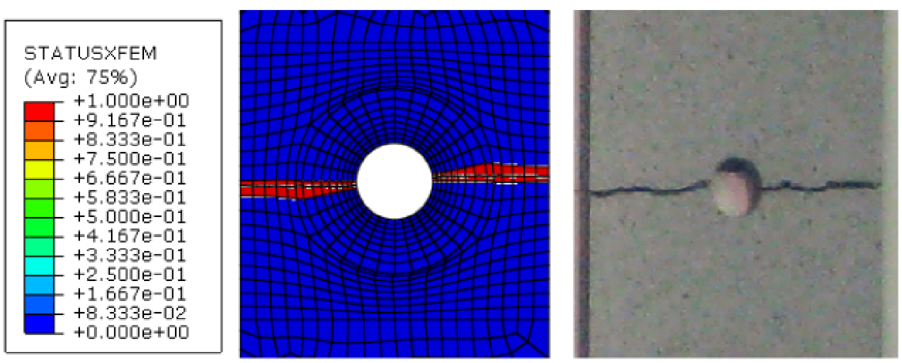

Figure 6.5: Comparison of the XFEM and experimental result for cast iron.

work and the critical angles are determined to be ±45 degrees. This predicts that the normal to failure surface is inclined 45 degrees in the plane of $n_1 - n_3$ and based on the direction of the n_3 vector this surface could be inclined on the surface and perpendicular to the direction of loading in the out of plane direction or it could be inclined in the out of plane direction and normal to the direction of the loading on the plane. The failure surface based on the second case of the $n_1 - n_3$ surface is presented in figure (6.6).

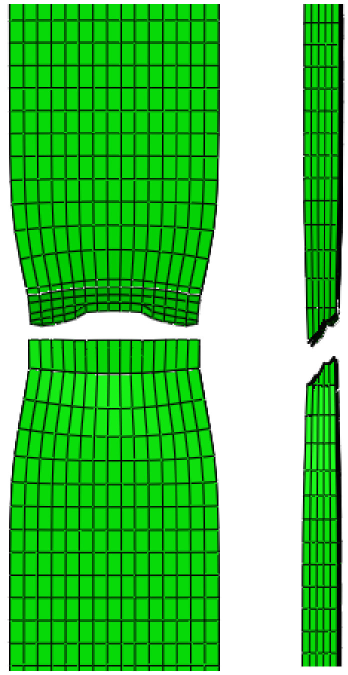

Figure 6.6: Failure surface based on localization analysis of Tresca Criterion.

For von Mises criteria, the localization analysis provides different results for an associated in compare to a non-associated plasticity model, also this model has different critical angles based on the type of loading and whether the model is a $3D$ model or $2D$ plane stress or plane strain. The results of localization analysis for the associated case are summarized in table (6.1), where $f(\nu)$ is defined as

Table 6.1: Critical angles of associated von Mises plasticity based on localization analysis.

	Tension	Compression	Shear	Biaxial tension
Plane Stress θ_{crit}	35.26	54.74	45.00	0.00
Plane Strain θ_{crit}	45.00	45.00	45.00	45.00
Three Dimensional θ_{crit}	f(ν)	f(ν)	f(ν)	f(ν)

$$\theta_{crit} = \pm \text{atan}\sqrt{-\frac{n_3 + \nu n_2}{n_1 + \nu n_2}}. \tag{6.2}$$

The comparison of the inelastic XFEM modeling of associated von Mises plasticity for the case of plane stress and plane strain under compressive loading is depicted in figure (6.7). The critical angle for plane stress case under compression is 54.74 with

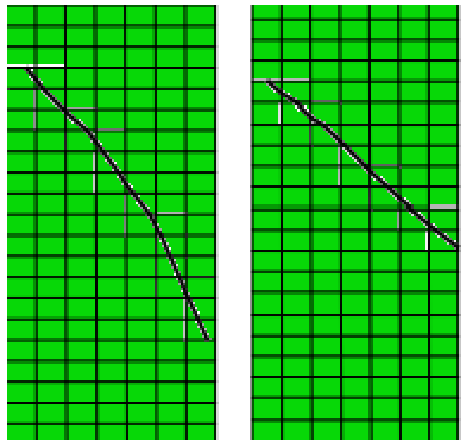

Figure 6.7: Critical angle for plane stress and plane strain under compression for associated von Mises plasticity.

respect to the direction of maximum principal and this angle is 45 degrees for the case of plane strain. As an example, for the case of three dimensional modeling and

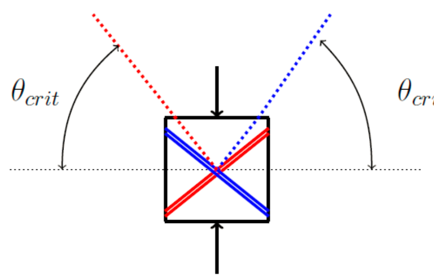

Figure 6.8: Critical angle for compression.

uniaxial tension, the critical angle for von Mises associated plasticity is calculated as

$$\boldsymbol{\sigma} = \begin{pmatrix} \sigma \\ 0 \\ 0 \\ 0 \\ 0 \\ 0 \end{pmatrix} \rightarrow \boldsymbol{s} = \begin{pmatrix} \frac{2\sigma}{3} \\ \frac{-\sigma}{3} \\ \frac{-\sigma}{3} \\ 0 \\ 0 \\ 0 \end{pmatrix} , \boldsymbol{n} = \frac{\sqrt{3}\boldsymbol{s}}{2\sqrt{\mathrm{J}_2}} \rightarrow \boldsymbol{n} = \begin{pmatrix} 1 \\ -\frac{1}{2} \\ -\frac{1}{2} \\ 0 \\ 0 \\ 0 \end{pmatrix} \rightarrow \tan^2(\theta_{crit}) = \frac{1+\nu}{2-\nu} \qquad (6.3)$$

In this work the general case of associated von Mises plasticity localization analysis is used to find the critical angle of localization. For this reason at every step of loading, for each element and gauss point the principal values and directions of the normal to the yield function are calculated and based on that the critical angle is calculated and it is multiplied by a rotation matrix to transform it to the global coordinates. In the case that the equivalent von Mises strain reaches the critical value, the crack is initiated and will propagate in the direction perpendicular to the critical angle, i.e.,

$$\text{if} \quad F = \frac{\epsilon_{eq}}{\epsilon_{cr}} = 1 \quad \text{then} \quad \theta_{crit} = \pm \text{atan}\sqrt{-\frac{n_3 + \nu n_2}{n_1 + \nu n_2}} \tag{6.4}$$

where this angle is on the $n_1 - n_3$ plane as shown in figure (6.9).

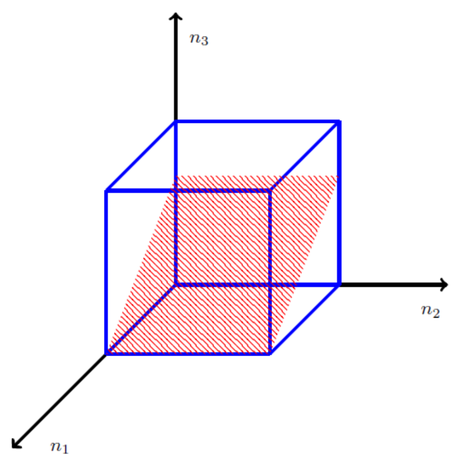

Figure 6.9: Crack surface.

Failure Directions, Rankine

Based on the Rankine criterion, the normal to the localization surface is parallel to the direction of maximum principal stress. The localization analysis of this model is used to investigate the behavior of the brittle cast iron flat bars. The boundary conditions and loading are designed in a manner to simulate the experimental tests. Five layers of brick elements are used in the thickness direction and the global element size is $0.35[in]$, this is shown in figure (6.10). For the case of perforated flat bars, four layers of elements are used and the global element size is $0.35[in]$ while finer elements are used in the vicinity of the perforation, this is shown in figure (6.11).

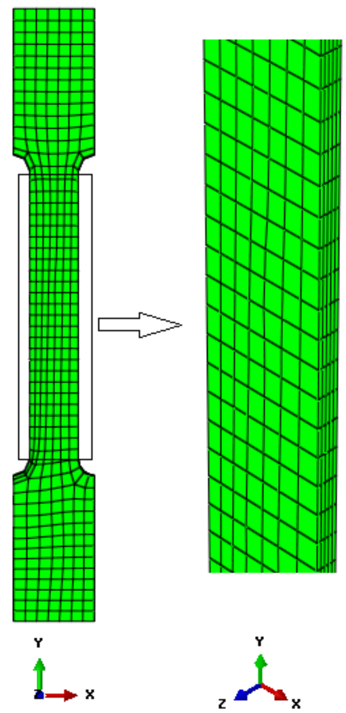

Figure 6.10: Mesh of the flat bar.

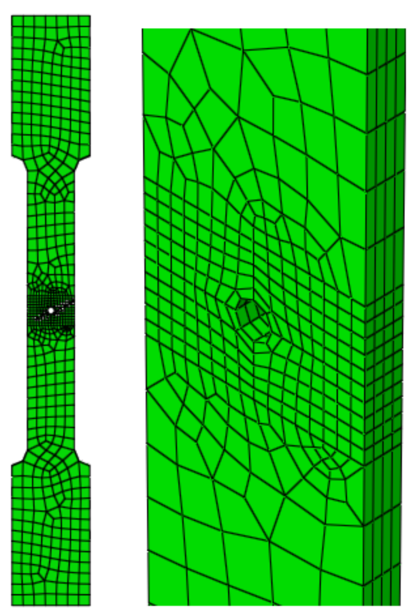

Figure 6.11: Mesh of the perforated flat bar.

The longitudinal stress distribution for the cast iron specimen in different stages of loading is depicted in figure (6.12).

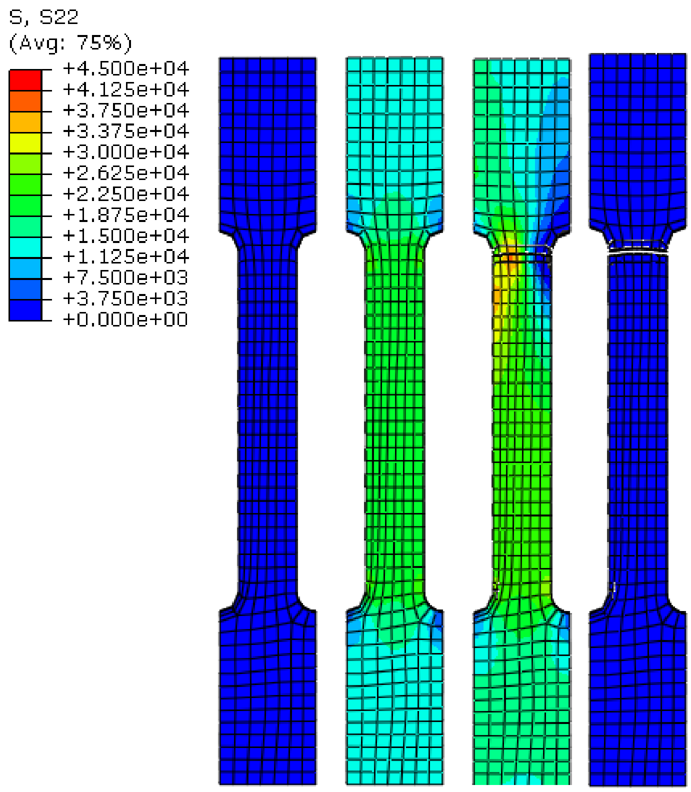

Figure 6.12: Distribution of the longitudinal stress at different stages of loading.

The failure direction of the perforated cast iron specimen is presented in figure (6.13).

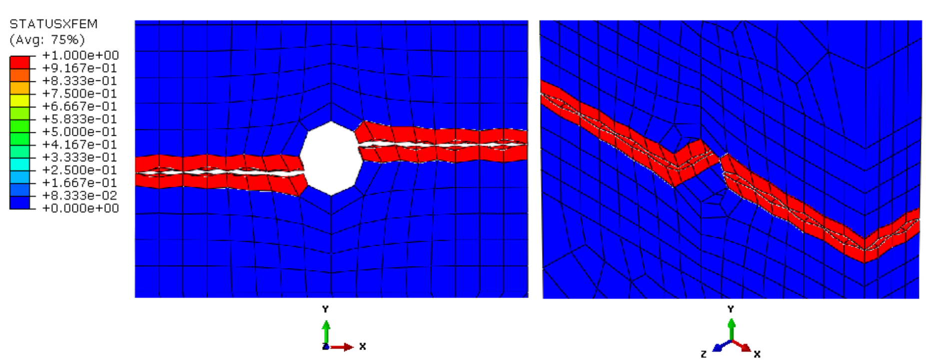

Figure 6.13: Isometric and front view of the cracked specimen.

Failure Directions, Tresca

Tresca criterion is used for modeling the behavior of ductile material and it predicts that the critical angle of the normal to the localization surface is 45 degrees for all the loading conditions, therefore it is assumed as a priori for initial investigation of the failure surface in compare to von Mises where this angle is varying based on the loading conditions. For this model the same mesh as described in the previous section is used. If the $n_1 - n_3$ surface is parallel to the front surface of the specimen, then the crack would be inclined on the surface of the specimen, and if the $n_1 - n_3$ surface is perpendicular to the surface of the specimen, the crack would be inclined through the dept of the specimen and it would be horizontal on the surface, this is shown in figure (6.14).

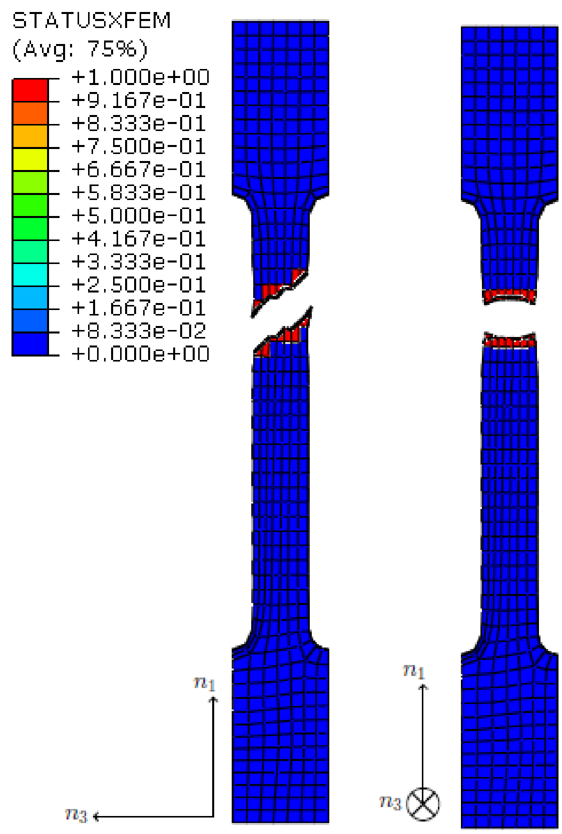

Figure 6.14: Comparison of the failure surface for different principal directions $n_1 - n_3$.

Failure Directions, von Mises Plasticity

The localization analysis of the associated von Mises plasticity is applied to the ductile flat bars in order to investigate the behavior of this model. The same mesh as depicted in figure (6.10) is used. The evolution of the von Mises stress and maximum principal strain distributions from the beginning of the test, onset of plastification, cracking and failure are depicted in figures (6.15) and (6.16) respectively. These

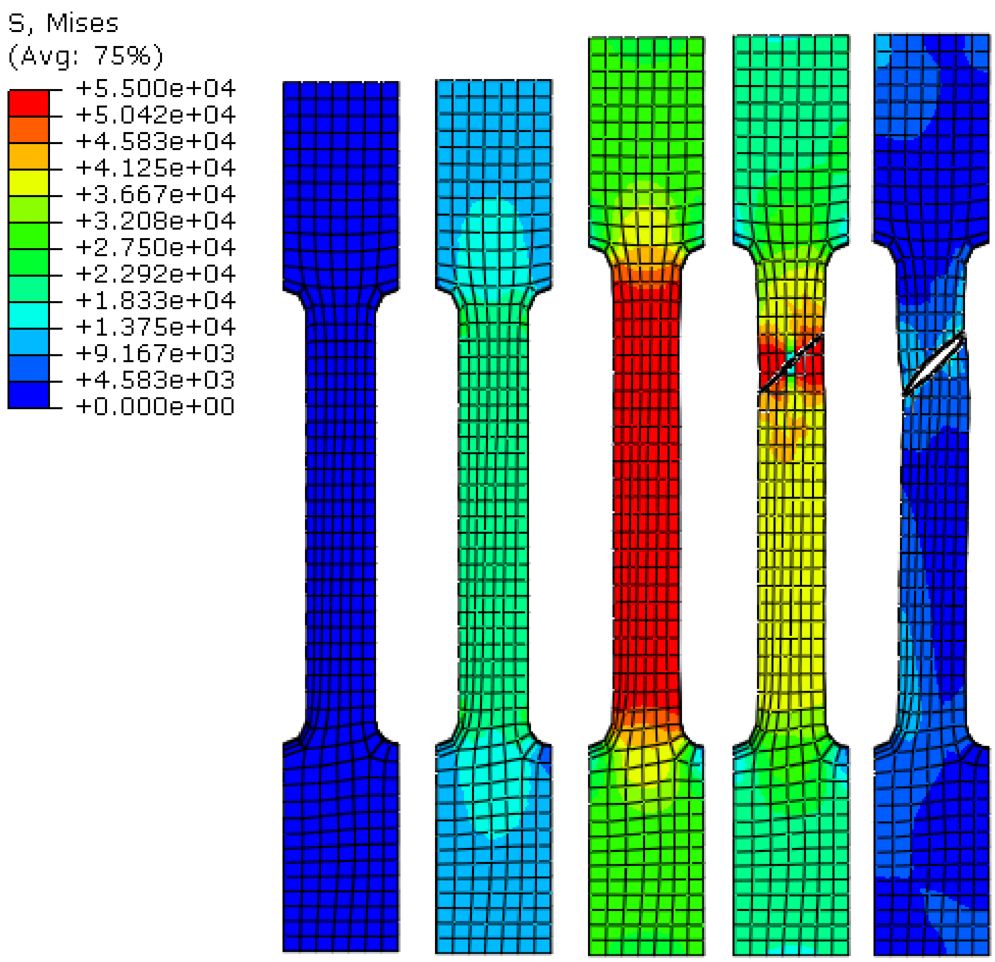

Figure 6.15: Distribution of the von Mises stress at different stages of loading.

results confirm the calculations of the localization analysis of the von Mises associated plasticity, wich predicts that the crack is inclined with an angle approximately 41 degrees. The directions of the maximum and minimum principals at the onset of cracking is presented in figure (6.17). This shows that the $n_1 - n_3$ surface is parallel to

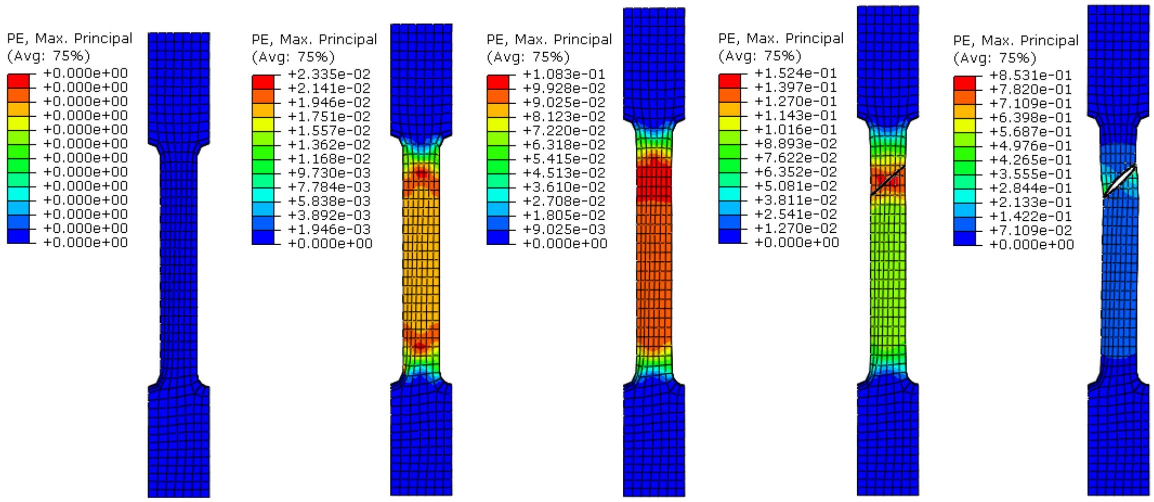

Figure 6.16: Distribution of the plastic strain at different stages of loading.

the surface of the specimen and n_1 is in the direction of loading. The calibrated model

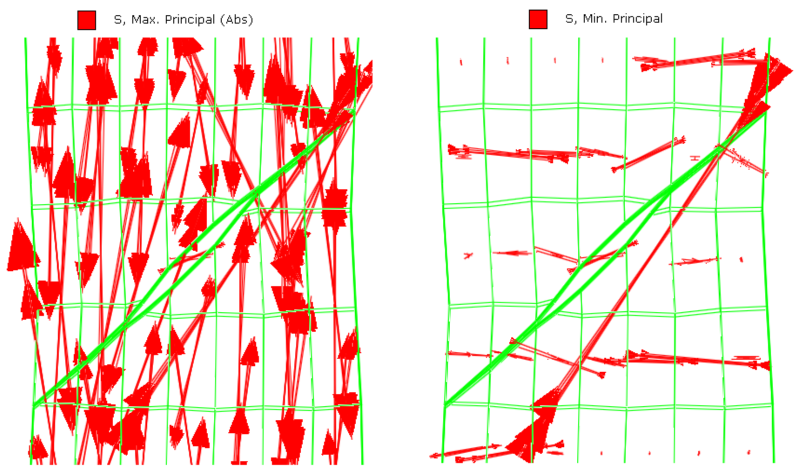

Figure 6.17: Direction vectors of maximum and minimum principal stresses.

is used for the perforated specimen and the evolution of the crack and plastic strain for the flat bar with $^1/_4$ circular diameter is depicted in figure (6.18). A magnified view of the cracked surface for the perforated specimen is presented in figure (6.19). It is observed that not only there is in-plane inclination of the crack surface in the $x - y$ plane, but also the crack is inclined in the $x - z$ plane.

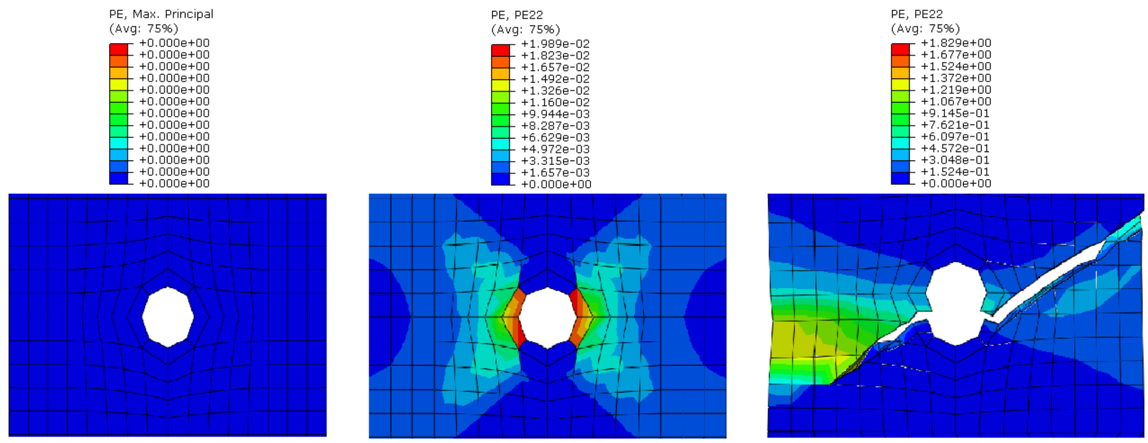

Figure 6.18: Distribution of the plastic strain at different stages of loading.

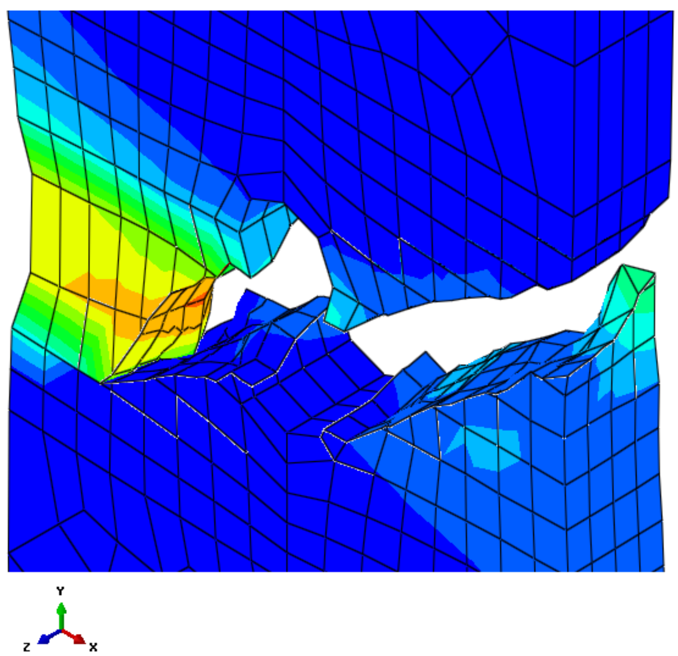

Figure 6.19: Isometric view of the cracked specimen.

SIMULATION OF CONCRETE SPECIMENS

In order to simulate the behavior of concrete the experimental data are extracted and used in order to calibrate the numerical model introduced earlier in this work. This numerical model is a Drucker-Prager plasticity model coupled with scalar damage where the plasticity and damage functions are separate and damage enters the yield function in terms of effective stresses. The benefit of using plasticity models for concrete is that it provides the capability of simulating the permanent deformation in the case of unloading while the damage models will have an unloading path that returns to initial values of strains. In order to investigate and calibrate this model, experimental observations are performed for concrete under uniaxial compression as well as concrete under cyclic compression. The cyclic behavior of the concrete is depicted earlier in this work and in this section the numerical model is calibrated based on that and the axial experiments. The numerical model is written in Fortran and then connected to Abaqus software using user subroutine UMAT. This provides the capability of using this model for a variety of geometries and loading scenarios. The heading of the UMAT subroutine is depicted in figure (6.20).

```
      SUBROUTINE UMAT(STRESS, STATEV, DDSDDE, SSE, SPD, SCD, RPL,
     . DDSDDT, DRPLDE, DRPLDT, STRAN, DSTRAN, TIME, DTIME, TEMP, DTEMP,
     . PREDEF, DPRED, CMNAME, NDI, NSHR, NTENS, NSTATV, PROPS, NPROPS,
     . COORDS, DROT, PNEWDT, CELENT, DFGRD0, DFGRD1, NOEL, NPT, LAYER,
     . KSPT, KSTEP, KINC)
C
      INCLUDE 'ABA_PARAM.INC'
C
      CHARACTER*80 CMNAME
      DIMENSION STRESS(NTENS), STATEV(NSTATV), DDSDDE(NTENS, NTENS),
     . DDSDDT(NTENS), DRPLDE(NTENS), STRAN(NTENS), DSTRAN(NTENS),
     . PREDEF(1), DPRED(1), PROPS(NPROPS), COORDS(3), DROT(3, 3),
     . DFGRD0(3, 3), DFGRD1(3, 3)
```

Figure 6.20: User subroutine UMAT.

6.2.1 Calibration of the Damage-Plasticity Model

The Drucker-Prager plasticity and damage model behavior for cyclic compression behavior is depicted in figure (6.21). The plotted figure is based on the calibration data used in Salari et al. (2004) and it is tabulated in table (6.2). This model is also

Table 6.2: Parameters used in damage-plasticity model from Salari et al. (2004).

E [MPa]	ν	α_0	α_m	b_1	K_0 [MPa]	K_m [MPa]	b_2	β	c_t	c_c	p
21500	0.192	0.23	0.23	0	6.27	8.16	5000	0.115	1.0	0.1	0.01

calibrated with the experimental results obtained from in-house experiments and the

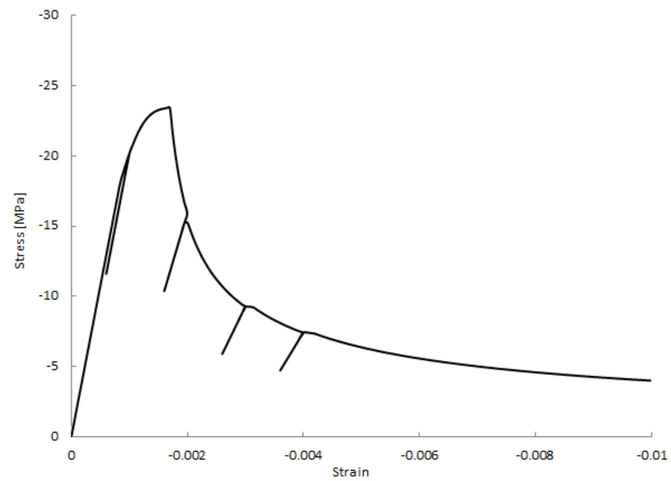

Figure 6.21: Cyclic behavior of the damage plasticity model under compression.

results are tabulated in table (6.3). The comparison of the stress-strain curves for uniaxial compression and cyclic compression tests based on the calibrated data are depicted in figures (6.22) and (6.23) respectively.

Table 6.3: Parameters calibrated based on the experiments at the University of Houston.

E [MPa]	ν	α_0	α_m	b_1	K_0 [MPa]	K_m [MPa]	b_2	β	c_t	c_c	p
27000	0.2	0.36	0.36	0	3.27	9.16	1500	0.11	1.0	0.5	0.7

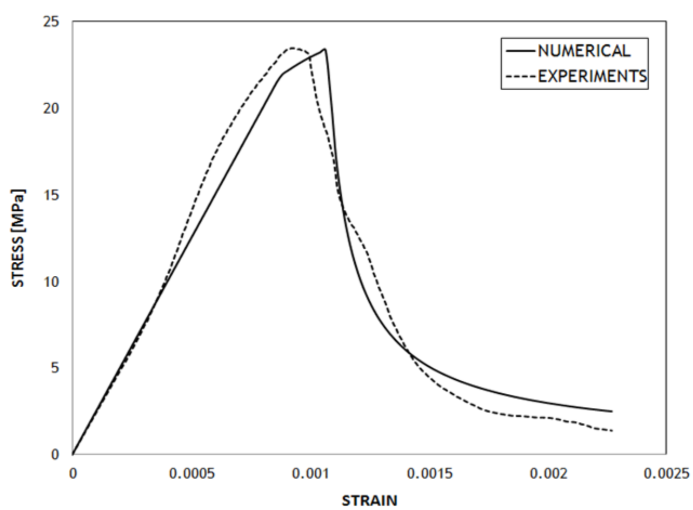

Figure 6.22: Comparison of the experimental and numerical model for uniaxial compression test.

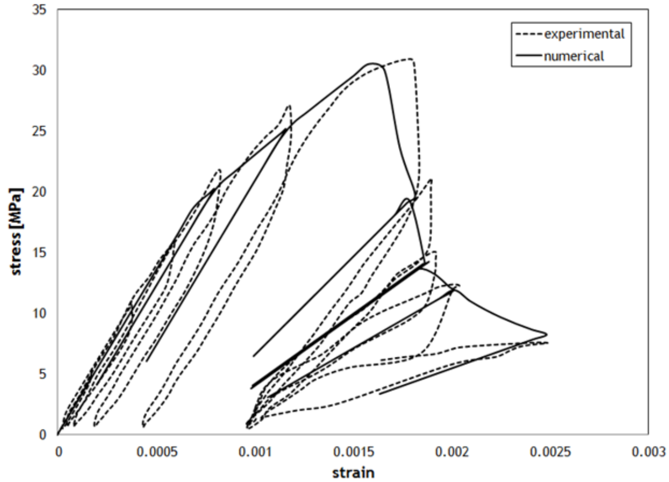

Figure 6.23: Comparison of the experimental and numerical model for cyclic compression test.

These calibrated parameters are used in the model in order to calculate the numerical localization properties of the damage, plasticity and damage-plasticity models. The localization analysis for the damage, plasticity and damage-plasticity models under uniaxial tension of a unit brick are depicted in figures (6.24), (6.25) and (6.26) respectively. Also the comparison of the localization analysis of these models is depicted in figure (6.27).

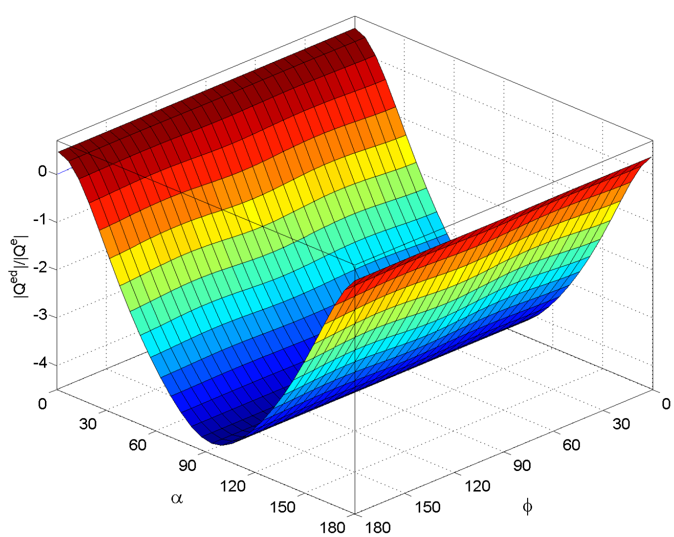

Figure 6.24: Localization analysis of the damage model for tension test.

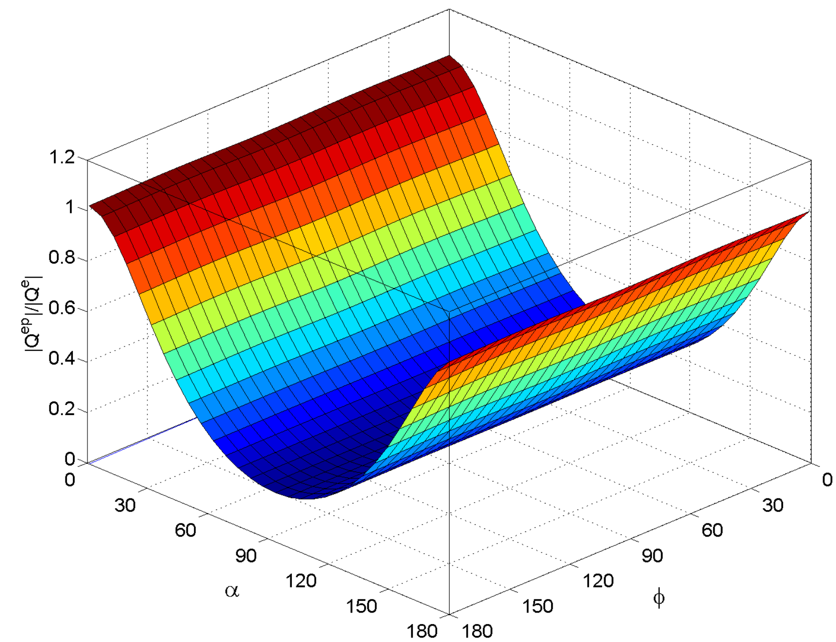

Figure 6.25: Localization analysis of the plastic model for tension test.

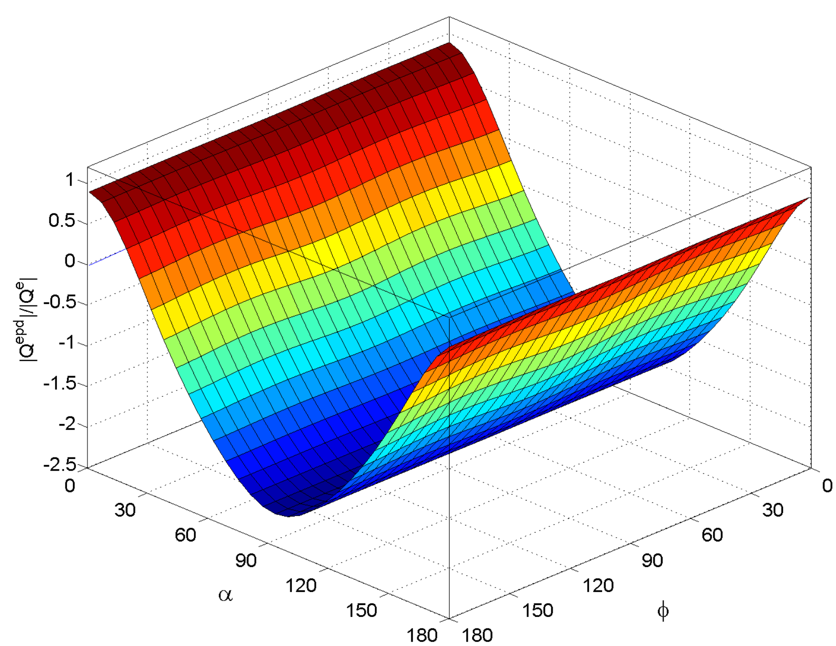

Figure 6.26: Localization analysis of the damage-plastic model for tension test.

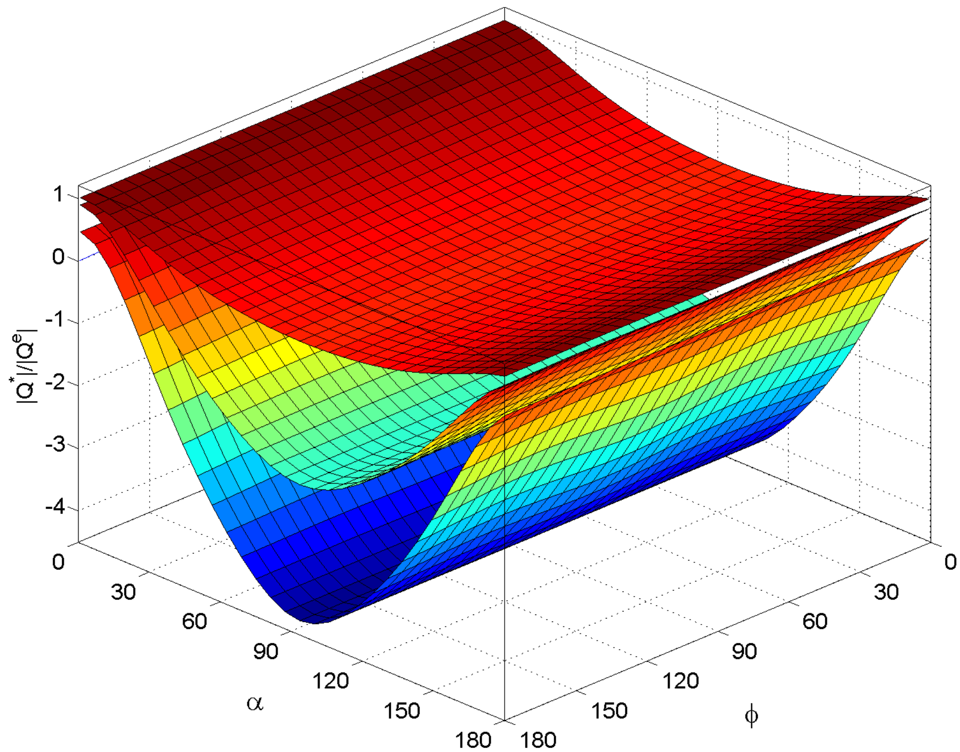

Figure 6.27: Comparison of the localization analysis of the plastic (top), damage-plasticity (middle) and damage (bottom) models for tension test.

In the case of compression, since the damage model is based on the positive volumetric strains, the pure damage model is not activated and therefore there is no localization analysis for that case, but in the case of damage-plasticity the positive volumetric plastic strains will trigger the damage initiation as discussed earlier in equation (2.101). The localization properties of the plastic and damage-plasticity models for compression test are presented in figures (6.28) and (6.29) respectively. The comparison of the localization analysis of damage-plasticity and plasticity models is depicted in figure (6.30). It is observed that the damage-plasticity model is more susceptible to loss of ellipticity in compare to the plasticity model and therefore it is expected that the formation of weak discontinuities be a priori for the combined damage-plasticity formulation.

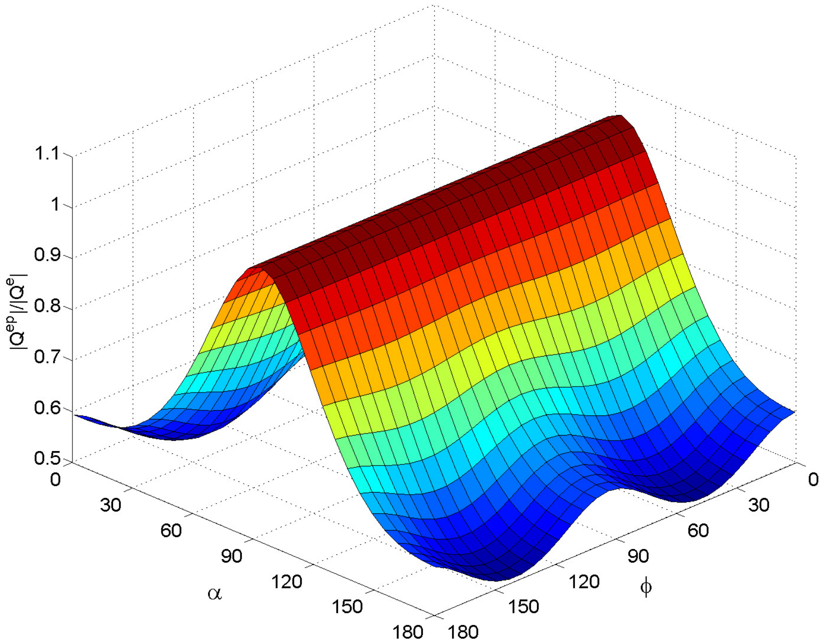

Figure 6.28: Localization analysis of the plastic model for compression test.

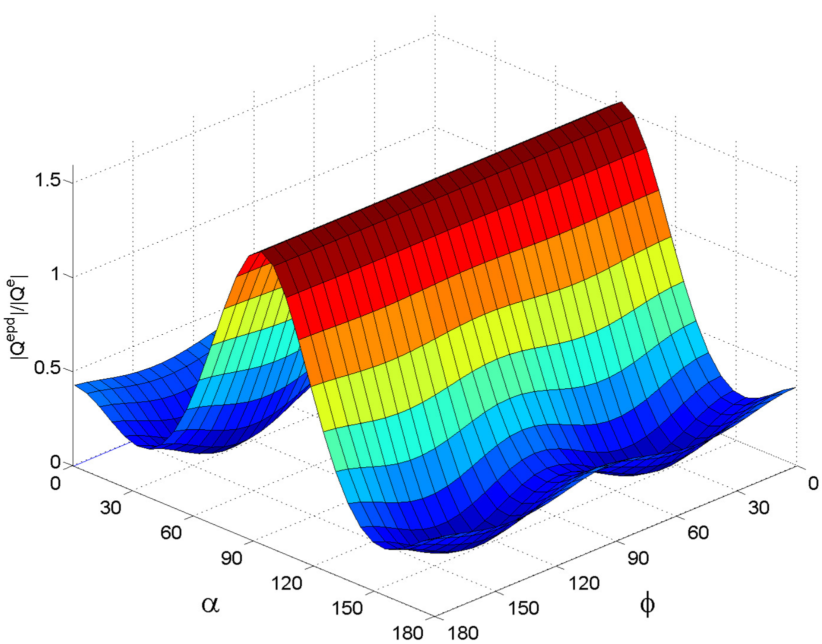

Figure 6.29: Localization analysis of the damage-plastic model for compression test.

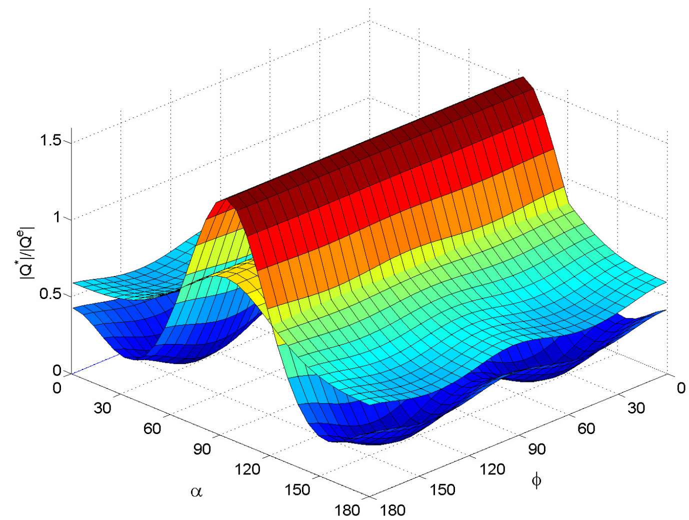

Figure 6.30: Comparison of the localization analysis of the plastic and damage-plasticity models for compression test.

In the case of associated plasticity it is expected to see lower critical values of the localization analysis, the comparison of the associated and non-associated damage-plasticity models is depicted in figure (6.31).

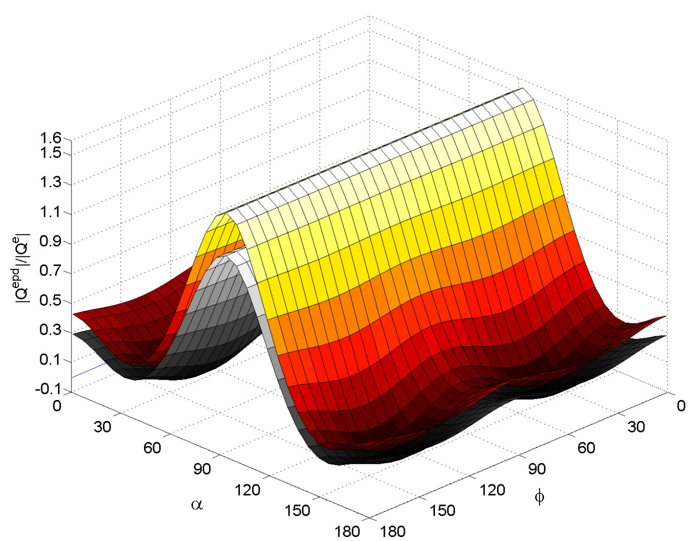

Figure 6.31: Comparison of the localization analysis of the associated and non-associated damage-plasticity models for compression test (grey=associated, hot=non-associated).

Chapter 7. Concluding Remarks

Theoretical background of plasticity and damage-plasticity models were discussed, then the failure diagnostics of the material behavior was explained and studied by the loss of stability, loss of uniqueness and loss of ellipticity and theoretical localization analysis of different yield criteria were presented. The backgrounds of the extended finite element method was described and this method was utilized in conjunction with localization analysis to form the concept of inelastic XFEM. In the numerical implementation chapter, the general framework for modelling the plasticity and damage-plasticity models was introduced and adequate formulations for solving the unknowns of the constitutive driver based on the fully implicit backward Euler and Newthon-Raphson methods were explained. Moreover numerical implementation of the localization analysis of these models for associated and non-associated plasticity were presented.

Experimental observations on the metallic and cementitious materials were performed. Mild steel, aluminum, high strength steel and cast iron flat bars were tested under uniaxial tension and the effect of perforation on the ultimate load capacity and ultimate tensile strength of these materials was studied. Uniaxial and cyclic compression tests were performed on concrete specimens and the corresponding load-deformation and stress-strain curves were achieved. A digital image correlation system was used to monitor the experiments and provide displacement and strain fields on the surface of the specimens at different stages of the experiment. The accuracy of the DIC system in terms of displacement measurements was compared with the results obtained by LVDT and it was observed that corresponding root mean square deviation was very small.

The spatial and displacement data obtained by DIC system were extracted and based on a finite element discretization and the least square approximation the best nodal displacements of the elements were calculated. The error associated with this procedure was calculated and compared for different element types. Finally the infinitesimal and finite strain distribution of the finite element were calculated and compared with the results obtained by Aramis software. It was observed that this method has very small sensitivity to the number of facets while the strain values calculated by the Aramis software were sensitive to facet size.

Furthermore, the numerical models exploited to model metallic specimens were calibrated with the experimental results of the non-perforated specimens and used to predict the behavior of the perforated and non-perforated specimens. The comparison of the failure modes and directions observed by the experimental observations and these models were presented and discussed. The von Mises and Tresca criteria were used in order to initiate crack propagation for ductile metals and the Rankine or St. Venant criteria was used to model cast iron.

Finally, the damage-plasticity model of Drucker-Prager and scalar damage was calibrated with the experimental results obtained by uniaxial and cyclic compression tests performed on concrete cylinders. The numerical localization analysis was implemented inside the constitutive driver of this model and the normalized values of the determinant of the localization tensor were calculated at the onset of damage, plasticity and damage-plasticity and compared for the case of associated and non-associated plasticity.

REMARKS ON THE LEAST SQUARE APPROXIMATION

It was observed that the displacement data obtained by DIC system were congruous with the results obtained by LVDT, this was shown in figure (5.12) and table (5.2). The least square approximation of the finite element discretization covering the facet data was performed for different element types, and it was concluded that the error associated with this method decreases while increasing the element numbers, however this was true while there were enough facet data inside the element. It was also observed that the error associated with Q_9 elements was smaller than Q_8 and

Q_4, but as the number of elements increases the difference in the errors were minimal. This is depicted in figure (5.29).

The results of the finite and infinitesimal strain obtained by least square analysis were compared to the ones calculated by Aramis software, it was observed that although the displacements were in good agreement with each other the strains were not the same. Therefore a study was conducted to see the effect of facet size and facet number on the strain distributions of these methods. It was perceived that the Aramis software provided different values of the strain distribution on the specimen as shown in table (5.4) and figures (5.38) and (7.3) while the least square approximation provided very close results as presented in table (5.5) and figure (7.1). It

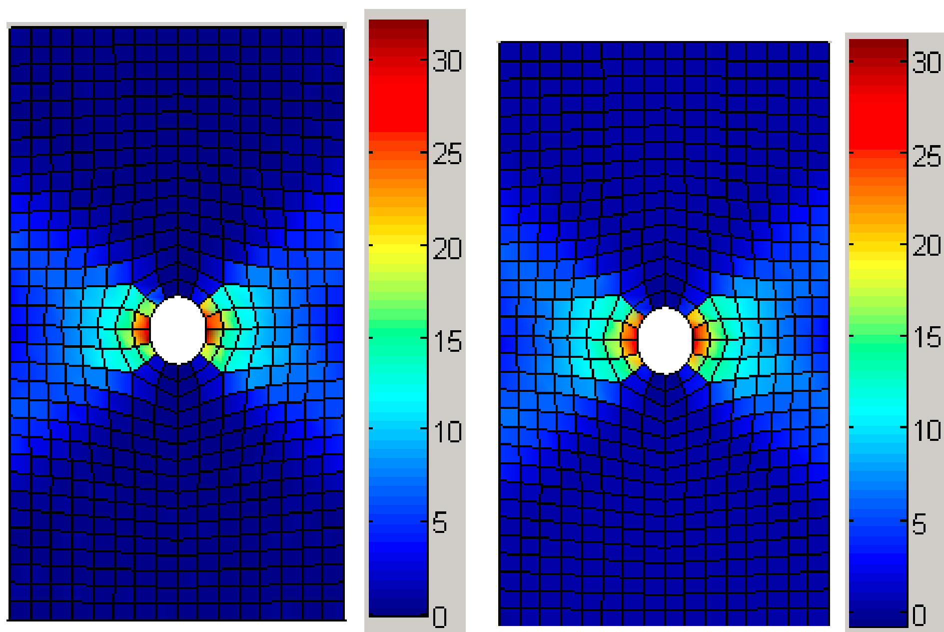

(a) Facet size = 15, step = 9 **(b)** Facet size = 11, step = 7

Figure 7.1: Difference in longitudinal Green strain distribution for the same load stage due to different facet sizes based on least square approximation.

was observed from figure (7.1) that the strain calculation based on the least square approximation was almost identical for different facet sizes.

The future work on this method is focused on comparing different stages of the experiment and calculating the strain distributions based on an updated Lagrange

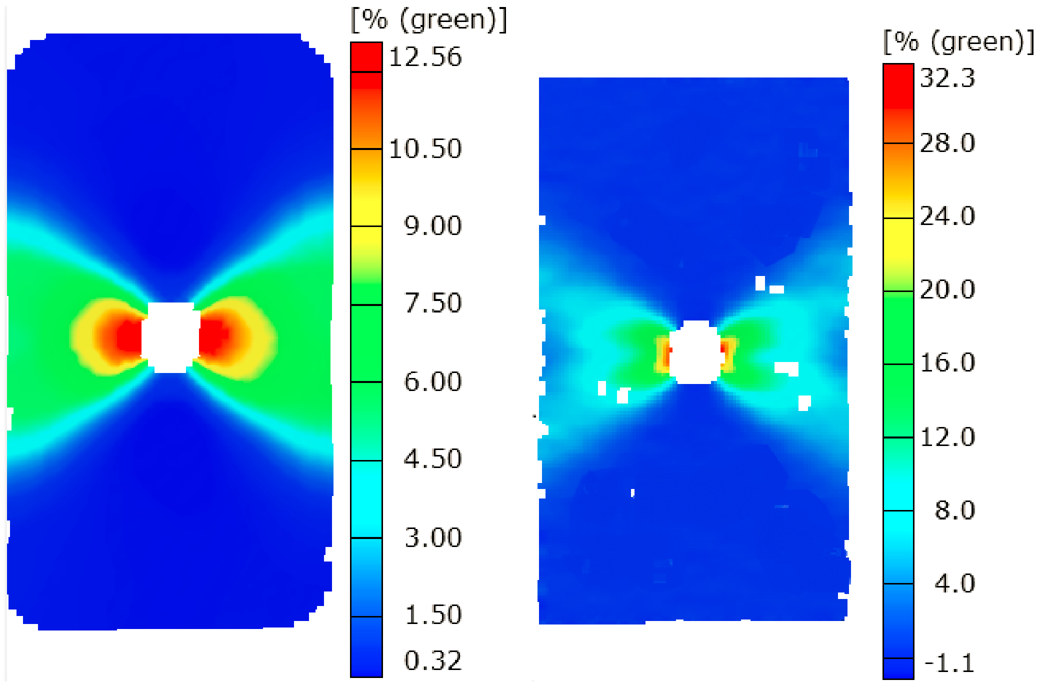

(a) Facet size = 15, step = 9 **(b)** Facet size = 11, step = 7

Figure 7.2: Difference in longitudinal Green strain distribution for the same load stage due to different facet sizes, Aramis software.

approach and to come up with appropriate methodologies to find localized failures on the specimen. This could be achieved in several ways, one would be to calculate the vorticity, shear and divergence distribution on the surface of the specimen as discussed by Peterson and Sulsky (2011) and find the onset of discrete behavior, in another way it is possible to calculate the strain rate from one stage to another stage and find the rank of the strain tensor by an eigenvalue analysis, if there exists a rank deficiency in the strain tensor, this could indicate a jump in the strain rate and therefore a sign of the loss of ellipticity in the material at that point.

REMARKS ON THE INELASTIC XFEM MODELING

The load-deformation curves of the experimental observations on the perforated and non-perforated mild steel, aluminum, high strength steel and cast iron flat bars were obtained and based on that the effect of circular opening on the ultimate load capacity and tensile strength of these materials was investigated. Although it was expected to observe a sixty percent drop in the load capacity of the cast iron specimen because of the stress concentration effects, the load capacity of the perforated cast iron specimen only decreased by fifteen percent, this was also true for ductile materials where local plastification in the vicinity of the perforation was the main reason for this. The results of these comparisons were depicted in figures (5.9) and (5.10).

It was observed that the Rankine or St. Venant criteria were capable of predicting the behavior of the brittle cast iron specimens, the comparison of the calibrated stress-strain curve of the model and the experiment was depicted in figure (6.3). Based on the localization analysis, the normal to the failure surface was parallel to the principal stress/strain direction and therefore, the material failed perpendicular to this direction which was in agreement with the experimental observations and was depicted in figure (6.5).

In the case of Tresca criteria, it was perceived that in the case that the direction of the minimum principal of the normal to the yield surface was pointing through the thickness of the specimen, the failure surface predicted by this model was similar to the failure surface observed in the case of aluminum specimen. It should be noted that the critical angle based on this method was 45 degrees. This method was also a good prediction of the failure surface of the non-perforated mild steel that has an inclined failure surface in the out of plane direction and it was perpendicular to the direction of loading in the in plane direction.

In the case of von Mises plasticity, the critical angle was different based on the associativity and non-associativity of the problem, however in this work the associated plasticity model was used. The prediction of the normal to the failure surface for this model differed for $2D$ and $3D$ cases. It was observed that in case of uniaxial tension for plane stress this angle was 35.26 and for the plane strain it was 45 degrees. However in $3D$ cases, the critical angle was a function of the normal to the yield surface and the Poisson's ratio. For the uniaxial $3D$ case this angle was approximately 41 degrees.

This confirmed the experimental results observed in the perforated mild steel and non-perforated high strength steel specimens as depicted in figures (7.3) and (7.4) respectively.

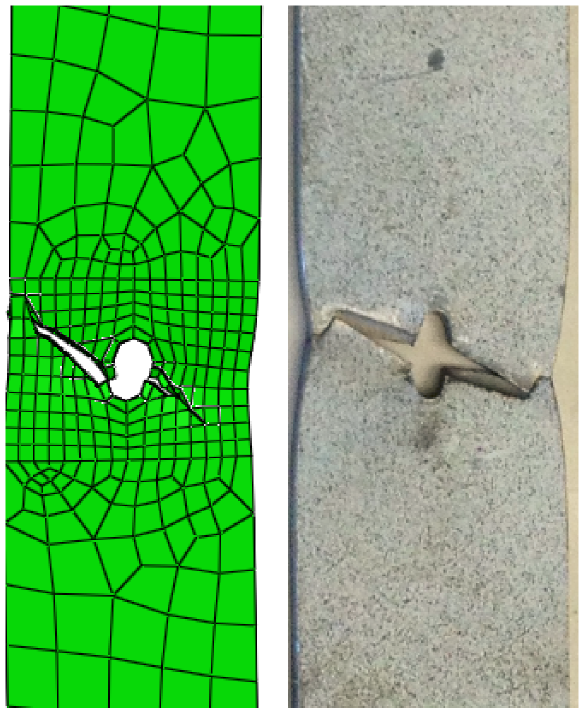

Figure 7.3: Comparison of the failure mode predicted by von Mises criterion and the experimental result on perforate mild steel.

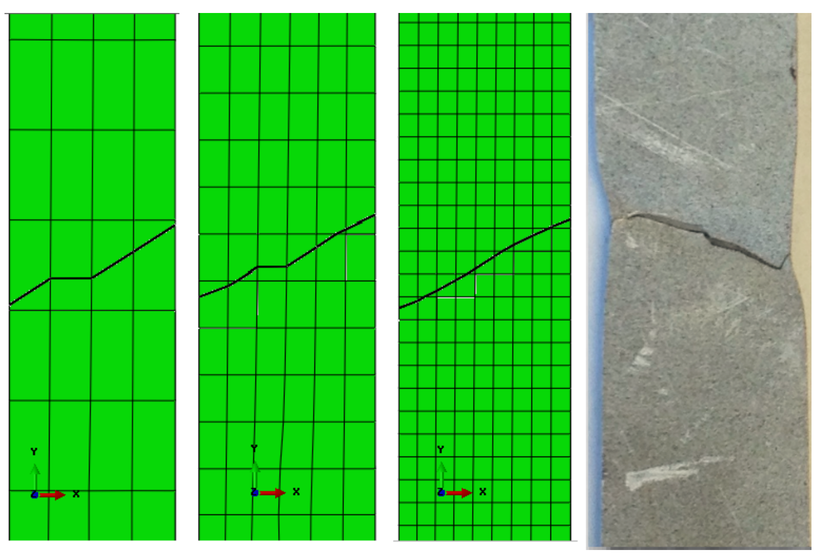

Figure 7.4: Comparison of the failure mode predicted by von Mises criterion and the experimental result on high strength steel.

REMARKS ON THE DAMAGE-PLASTICITY MODEL

Drucker-Prager yield function and scalar damage model were used together to model the behavior of concrete. This model was calibrated with uniaxial and cyclic compression experiments performed at the university of Houston. The calibrated parameters were presented in table (6.3). The numerical localization analysis was implemented inside the constitutive driver written for this model to find the localization properties of the damage, plasticity and damage-plasticity models. In tension test it was observed that the localization properties of the damage model were very critical and for the calibrated parameters the normalized value of the determinant of the localization tensor was mostly negative as depicted in figure (6.24). The critical angle associated with this model was 90 degrees in the $n_1 - n_2$ plane. The plasticity model in tension had stable localization properties and the minimum eigenvalue associated with this was greater than zero as presented in figure (6.25). Therefore plasticity regularized the damage localization properties in the case of damage-plasticity in tension, however as observed from figure (6.26) the normalized determinant of the localization tensor still exhibits negative values.

In the compression test, since the damage model used here was based on the positive values of volumetric strain it was not activated in the absence of plasticity and therefore there was no pure damage case in compression test. The localization analysis of the plasticity model in compression was depicted in figure (6.28), it was observed that all the values were positive and the minimum eigenvalue was associated with α equal to zero and ϕ equal to approximately 47 degrees. When the damage-plasticity model was analyzed, the localization properties were more critical than the pure plastic case, however all the values were still in the positive range and the critical values were associated with α equal to 24.7 degrees and ϕ equal to 43.21 degrees. The summary of the localization properties for this model in tension and compression are presented in table (7.1).

Table 7.1: Localization properties of the damage, plasticity and damage-plasticity models.

	Tension Test		
	Damage	Plasticity	Damage-Plasticity
α_{crit}	90	90	90
ϕ_{crit}	CST	CST	CST

	Compression Test		
	Damage	Plasticity	Damage-Plasticity
α_{crit}	NA	0 - 180	24.7 - 155.3
ϕ_{crit}	NA	47 - 133	43.2 - 136.8

In the case of associated flow plasticity, based on equation (3.6) and Bromwich bounds, it was expected that the minimum eigenvalues of the localization tensor, form a lower bound for the eigenvalues of the non-associated model. This rose from the fact that the minimum eigenvalues of the symmetric part of a tensor were smaller than the eigenvalues of that unsymmetric tensor. The comparison of the localization surfaces of the associated and non-associated models was presented in figure (6.31). It was observed that the associated model has formed a lower bound for the non-associated model and the values of the normalized determinant of the localization tensor are more critical for the associated case. The difference between the normal to the yield function and the normal to the potential function provided an unsymmetrical elasto-plastic damage tangent operator and when this fourth order tensor was contracted into a second order tensor by multiplying the normal to the localization surface, it formed the unsymmetrical second order localization tensor.

References

ABAQUS (2012). *Version 6.12-1.* Dassault Systemes Simulia Corporation, Providence, Rhode Island.

Anderson, T. L. (1995). *Fracture Mechanics: Fundamentals and Applications*, Vol. 2. CRC Press.

Belytschko, T. and Black, T. (1999). "Elastic Crack Growth in Finite Elements with Minimal Remeshing." *International Journal for Numerical Methods*, 45, 601–620.

Carol, I. (1996). "Elastic Degradation and Damage: Plasticity-Like Formulation, Stiffness Recovery and Localization." *Mecánica Computacional*, 17, 243–251.

Carol, I. and Willam, K. J. (1997). "Application of Analytical Solutions in Elasto–Plasticity to Localization Analysis of Damage Models." *Computational Plasticity, Fundamentals and Applications*, 714–719.

Cervenka, J. and Papanikolaou, V. K. (2008). "Three Dimensional Combined FractureâĂŞPlastic Material Model for Concrete." *International Journal of Plasticity*, 24, 2192–2220.

Chaves, E. W. V. (2003). "A Three Dimensional Setting for Strong Discontinuities Modelling in Failure Mechanics." *Ph.D. Dissertation, Universitat Politécnica de Catalunya.*

Cosserat, F. and Cosserat, E. (1909). "Theorie des Corps Deformables.

Coulomb, C. A. (1776). "Essai sur une Application des Regles des Maximis et Minimis a Quelquels Problemesde Statique Relatifs, a la Architecture." *De l'Imprimerie Royale*, 10, 157–165.

de Borst, R. (1993). "A Simulation of Strain Localization: a Reappraisal of the Cosserat Continuum." *Engineering Computations*, 8, 317–332.

Drucker, D. C. and Prager, W. (1952). "Soil Mechanics and Plastic Analysis for Limit Design." *Quarterly of Applied Mathematics*, 10, 157–165.

Etse, G., Nieto, M., and Steinmann, P. (2003). "A Micropolar Microplane Theory." *International Journal of Engineering Science*, 41, 1631–1648.

Giner, E., Sukumar, N., Tarancón, J. E., and Fuenmayor, F. J. (1999). "An Abaqus Implementation of the Extended Finite Element Method." *Engineering Fracture Mechanics*, 76, 347–368.

Grammenoudis, P. and Tsakmakis, C. (2008). "Isotropic Hardening in Micropolar Plasticity." *Archive of Applied Mechanics*, 79, 323–334.

Grassl, P. and Jirásek, M. (2006). "Damage-Plastic Model for Concrete Failure." *International Journal of Solids and Structures*, 43, 7166–7196.

Gurson, A. L. (1975). *Plastic Flow and Fracture Behavior of Ductile Materials Incorporating Void Nucleation, Growth, and Interaction.* Ph.D. Dissertation, Brown University.

Gurson, A. L. (1977). "Continuum Theory of Ductile Rupture by Void Nucleation and Growth: Part I–Yield Criteria and Flow Rules for Porous Ductile Media." *Journal of Engineering Materials and Technology*, 99, 2.

Hansen, N. R. and Schreyer, H. L. (1992). "Thermodynamically Consistent Theories for Elastoplasticity Coupled with Damage." *Damage Mechanics and Localization*, 34, 53–67.

Hansen, N. R. and Schreyer, H. L. (1994). "A Thermodynamically Consistent Framework for Theories of Elastoplasticity Coupled with Damage." *International Journal of Solids and Structures*, 31, 359–389.

Hill, R. (1962). "Acceleration Waves in Solids." *Journal of the Mechanics and Physics of Solids*, 10, 1–16.

Iordache, M. M. (1996). "Failure Analysis of Classical and Micropolar Elastoplastic Materials." *Ph.D. Dissertation, University of Colorado.*

Kang, H. D. and Willam, K. J. (1999). "Localization Characteristics of Triaxial Concrete Model." *Journal of Engineering Mechanics*, 125, 941–950.

Liebe, T. and Willam, K. J. (2001). "Localization Properties of Generalized Drucker-Prager Elastoplasticity." *Journal of Engineering Mechanics*, 127, 616–619.

Lubliner, J., Oliver, J., Oller, S., and Onate, E. ((1989)). "A Plastic–Damage Model for Concrete." *International Journal of Engineering Science*, 25, 299–326.

Maier, C. and Hueckel, T. (1979). "Nonassociated and Coupled Flow Rules of Elastoplasticity for Rock-Like Materials." *International Journal of Rock Mechanics Mining Sciences* & *Geomechanics Abstracts*, 16, 77–92.

Maier, G., Willam, K., and Rizzi, E. (1996). "On Failure Indicators in Multi-dissipative Materials." *International Journal of Solids and Structures*, 33, 3187–3214.

Mase, G. E. (1970). *Shaum's Outline of Theory and Problems of Continuum Mechanics.* McGraw-Hill Professional.

Matlab (2011). *Version 7.13.0.564 (R2011b).* The MathWorks Inc., Natick, Massachusetts.

Mazars, J. (1986). "A Description of Micro- and Macroscale Damage of Concrete Structures." *Engineering Fracture Mechanics*, 25(5-6), 729–737.

Mazars, J. and Pijaudier-Cabot, G. (1989). "Continuum Damage TheoryâĂŤApplication to Concrete." *Journal of Engineering Mechanics*, 115(2), 345.

Menétrey, P. and Willam, K. J. (1995). "Triaxial Failure Criterion for Concrete and Its Generalization." *ACI Structural Journal*, 92, 311–318.

Moës, N., Dolbow, J., and Belytschko, T. (1999). "A Finite Element Method for Crack Growth Without Remeshing." *International Journal for Numerical Methods in Engineering*, 46, 131–150.

Moës, N., Sukumar, N., Moran, B., and Belytschko, T. (2000). "An Extended Finite Element Method (X-FEM) for Two- and Three-Dimensional Crack Modeling." *European Congress on Computional Methods in Applied Sciences and Engineering*.

Ottosen, N. and Runesson, K. (1991). "Properties of Discontinuous Bifurcation Solutions in Elastoplasticity." *International Journal of Solids and Structures*, 27, 401–421.

Ottosen, N. S. and Ristinmaa, M. (2005). *The Mechanics of Constitutive Modeling*. Elsevier Science, 1st edition.

Peterson, K. and Sulsky, D. (2011). "Evaluating Sea Ice Deformation in the Beaufort Sea Using a Kinematic Crack Algorithm with RGPS Data." *Remote Sensing of the Changing Oceans*, 5.

Rice, J. R. and Rudnicki, J. W. (1979). "A Note on Some Features of the Theory of Localization of Deformation." *International Journal of Solids and Structures*, 16, 597–605.

Rudnicki, J. W. and Rice, J. R. (1975). "Conditions for the Localization of Deformation in Pressure–Sensitive Dilatant Materials." *Journal of the Mechanics and Physics of Solids*, 23, 371–394.

Salari, M., Saeb, S., Willam, K., Patchet, S., and Carrasco, R. (2004). "A Coupled Elastoplastic Damage Model for Geomaterials." *Computer Methods in Applied Mechanics and Engineering*, 193(27-29), 2625–2643.

Shao, J. F., Chiarelli, A., and Hoteit, N. (1998). "Modeling of Coupled Elastoplastic Damage in Rock Materials." *International Journal of Rock Mechanics and Mining Sciences*, 35.

Simo, J. C. and Hughes, T. J. R. (1998). *Computational Inelasticity*. Springer Verlag.

Steinmann, P. and Willam, K. (1994). "Finite Element Analysis of Elastoplastic Discontinuities." *Journal of Engineering Mechanics*, 120, 2428–2442.

Tresca, H. (1864). "M**é**moire sur L'**é**coulement des Corps Solides Soumis ***á*** de Fortes Pressions." *Comptes Rendus Hebdomadaires des SÃĺances de l'AcadÃĺmie des Sciences, Paris*, 59, 754.

von Mises, R. (1913). "Mechanik der Festen Korper im plastisch deformablen

Zustand." *Nachrichten von der Gesellschaft der Wissenschaften zu Göttingen, Mathematisch-Physikalische Klasse*, 1, 582–592.

Willam, K. and Iordache, M. M. (1996). "Computational Simulation of Discontinuous Failure Processes." *Mecanica computacional*, 17, 227–242.

Willam, K. J. (2002). "Constitutive Models for Engineering Materials." *Encyclopedia of Physical Science & Technology*, 3, 603–633.

Willam, K. J., Dietsche, A., Iordache, M. M., and Steinmann, P. (1995). "Localization in Micropolar Continua." *Chapter 9, Continuum Models for Materials with Microstructure, H.-B. Mühlhaus (ed.),John Wiley & Sons Ltd.*, 297–340.

Willam, K. J. and Iordache, M. M. (2001). "On the Lack of Symmetry in Materials." *Proceedings of International Conference Trends in Computational Structural Mechanics*, 233–242.

Willam, K. J. and Warnke, E. P. (1975). "Constitutive Models for the Triaxial Behavior of Concrete." *Proceedings of the International Assoc. for Bridge and Structural Engineering*, 19, 1–30.

Zienkiewicz, O. C., Taylor, R. L., and Zhu, J. Z. (2005). *The Finite Element Method: Its Basis and Fundamentals*. Elsevier Butterworth-Heinemann, 6th edition.